THE UNIVERSITY of ADELAIDE

Design and Fabrication of Non-Noble-Metal Electrocatalysts for Oxygen Reduction Reactions

Ji Liang

School of Chemical Engineering

A thesis submitted for the degree of Doctor of Philosophy

The University of Adelaide

Jul 2014

Chapter 4 Non-Noble-Metal decorated Carbon Hybrid for ORR

4.1 Introduction, Significance and Commentary

Pt-free catalysts for oxygen reduction reaction (ORR) with high performance and low cost are extremely desirable for the commercialization of many state-of-the-art devices, such as fuel cells, metal-air batteries and sensors. However, the design and fabrication of such materials are still highly challenging so far. In this work, we report a Fe-N decorated hybrid carbon material composed of ordered porous carbon (OPC) and in-situ grown carbon nanotubes (CNTs). This material has successfully combined the desired merits for ORR, such as highly active Fe-N species, good conductivity, large pore size and sufficient surface area to catalyse the electrochemical reduction of oxygen. The excellent characters of the material have resulted in outstanding ORR performances closely comparable with commercial Pt/C catalyst of the same amount.

The highlights and novelty in this work include:

1. High Performance

a). This carbon based material show outstanding ORR catalytic performances, including very positive ORR onset potential, high reaction current and efficient 4-electron ORR selectivity, which are closely comparable with Pt/C catalyst and have rarely been observed on Pt-free catalyst.

b). This Pt-free material has also shown a complete methanol tolerance and excellent long-term stability, which is much superior to the commercial Pt/C and makes this material especially suitable for applications such as fuel cells and batteries.

2. Novel Structure

a). We have for the first time prepared this Fe-N decorated hybrid carbon material of in-situ grown CNTs from porous carbon microblocks with 3-dimensionallty interconnected macroporous and abundant mesopores.

b). By this delicate design, this material has obtained: highly active and finely dispersed Fe-N catalytic sites, good conductivity from the highly graphitic CNTs, facile mass transportation from the ordered macropores and sufficient active site exposure from the robust mesopores. So, this material has combined the desired merits for an electrochemical catalyst for ORR.

3. New Method, Low Cost and Enlightenment for Future Study

a). This material is designed and synthesized with the idea of green chemistry: toxic chemicals have been avoided and the resultant wastes have been minimized. The chemicals involved in this research are very cheap and the final material was prepared by one-pot heating of all-solid precursors; thus the synthesis is inexpensive, low-hazardous and promisingly scalable.

b). Last but not the least, this study has shed light on a new route of material design by in-situ integration of different materials to combine together their advantages, which is especially

important not only for oxygen reduction but also for other materials for energy storage and conversion.

4.2 Fe-N Decorated Hybrid of CNTs Grown on Hierarchically Porous Carbon for High Performance Oxygen Reduction

This section is included in the thesis as it appears as a research paper submitted by **J. Liang**, R. F. Zhou, X. M. Chen and S. Z. Qiao, Fe-N Decorated Hybrid of CNTs Grown on Hierarchically Porous Carbon for High Performance Oxygen Reduction accepted for publication on *Advanced Materials.*

Statement of Authorship (Page 1)

Statement of Authorship

Title of Paper	Fe-N Decorated Hybrid of CNTs Grown on Hierarchically Porous Carbon for High Performance Oxygen Reduction
Publication Status	○ Published, ◉ Accepted for Publication, ○ Submitted for Publication, ○ Publication style
Publication Details	Accepted by Advanced Materials for publication 10.1002/adma.201401848

Author Contributions

By signing the Statement of Authorship, each author certifies that their stated contribution to the publication is accurate and that permission is granted for the publication to be included in the candidate's thesis.

Name of Principal Author (Candidate)	Ji Liang (First Author)		
Contribution to the Paper	Research plan, material synthesis, most of the characterizations, material performance assessment, manuscript drafting.		
Signature		Date	23/5/2014

Name of Co-Author	Ruifeng Zhou		
Contribution to the Paper	Assistance with material synthesis, result discussion and part of characterization		
Signature		Date	23/5/2014

Name of Co-Author	Xuemin Chen		
Contribution to the Paper	Assistance with part of characterization		
Signature		Date	23/5/2014

Name of Co-Author	Dr. Youhong Tang		
Contribution to the Paper	Assistance with part of characterization		
Signature		Date	23-05-2014

Statement of Authorship

Title of Paper	Fe-N Decorated Hybrid of CNTs Grown on Hierarchically Porous Carbon for High Performance Oxygen Reduction
Publication Status	○ Published, ◉ Accepted for Publication, ○ Submitted for Publication, ○ Publication style
Publication Details	Accepted by Advanced Materials for publication 10.1002/adma.201401848

Author Contributions

By signing the Statement of Authorship, each author certifies that their stated contribution to the publication is accurate and that permission is granted for the publication to be included in the candidate's thesis.

Name of Principal Author (Candidate)	Ji Liang (First Author)		
Contribution to the Paper	Research plan, material synthesis, most of the characterizations, material performance assessment, manuscript drafting.		
Signature		Date	23/5/2014

Name of Co-Author	Prof. Shizhang Qiao		
Contribution to the Paper	Design of the project, organisation of the research and supervision		
Signature		Date	23/5/2014

Name of Co-Author			
Contribution to the Paper			
Signature		Date	

Name of Co-Author			
Contribution to the Paper			
Signature		Date	

DOI: 10.1002/((please add manuscript number))
Article type: Communication

Fe-N Decorated Hybrid of CNTs Grown on Hierarchically Porous Carbon for High Performance Oxygen Reduction

v

*Ji Liang, Rui Feng Zhou, Xue Min Chen, You Hong Tang and Shi Zhang Qiao**

[*] Prof. Shi Zhang Qiao, Ji Liang, Rui Feng Zhou
School of Chemical Engineering, the University of Adelaide,
Adelaide, SA 5005, Australia
E-mail: s.qiao@adelaide.edu.au

Dr. You Hong Tang
Centre for Nano Scale Science and Technology,
School of Computer Science, Engineering, and Mathematics, Flinders University,
Adelaide, SA 5042, Australia

Xue Min Chen
School of Materials Science and Engineering, Tianjin University,
Tianjin, 300072, China

Keywords: hybrid carbon, carbon nanotube, *in-situ* growth, oxygen reduction, non-noble-metal

Electrochemical reduction of oxygen is the key step controlling the performance of various next-generation devices concerning the conversion and storage of energy, such as a fuel cell, metal-air battery or oxygen sensor.[1, 2] Due to the sluggish nature of oxygen reduction reactions (ORRs), catalyst materials are inevitably employed in these devices; and Pt nanoparticles supported on carbon black (Pt/C) have been the most active catalyst for ORR at the current stage.[3] However, the high cost, low reserve, poor durability and significant hazard to environment of Pt/C catalyst have consequently uplifted the cost and severely hindered the industrialization of these state-of-the-art devices. Thus, it is practically necessary and economically desirable to develop an alternative ORR catalyst with similar activity but much lower cost compared with Pt/C.

For this purpose, extensive efforts have been exerted on non-Pt materials for ORR catalysis, including both completely metal-free (*e.g.* carbon materials doped by one or multiple heteroelements) [3-10] and non-noble-metal (compounds) materials.[11-16] For the metal-free materials, the catalytic activity is generally believed to come from the charge relocation due to the heteroelement doping on the carbon framework.[8, 17, 18] Unfortunately, their relatively low ORR activity, especially the frequently negative ORR onset potential, makes them less competitive than

Pt when they are adopted alone in a fuel cell, although they generally have a good stability due to the strong covalent bonding between the carbon and dopant atoms.[8, 19] To deal with this, different metal species, as active additives, have been intentionally introduced [11, 12, 14, 20, 21] or preserved [15, 22] in doped carbons with the perspective of further enhancing their ORR catalytic activity. Among them, Fe-N decorated carbons (Fe-N-C) are particularly interesting and potentially promising due to the interactions between the Fe and N species on the carbon substrates, which could boost ORR activity by theoretical predictions.[18] Such materials with different structures have been recently reported, including nanorods,[23] tetrapods,[24] tubes [14] and sheets.[12] However, the ORR performance of these carbon-based composites still can hardly match that of Pt/C from the aspect of ORR onset potential and reaction current at the same catalyst loading amount; let alone the hazardous chemicals, harsh treatments, substantial amount of resulted pollutants, expensive precursors and/or tedious post-processing employed in the fabrications, which makes these materials further uneconomical for fabrication at large scale.

Based on our recent researches on the materials involved in electrochemical processes, apart from their chemical composition, the microarchitecture (*e.g.* graphitic crystalline, hierarchical meso- and/or macro-porosity *etc.*) can play an equally or even more important role in controlling the overall mechanism and kinetic of the catalysis process by affecting the conductivity, reactant accessibility and reactive sites exposure of the material;[10, 22, 25] and the aforementioned unsatisfactory performances of current Fe-N-C materials could possibly be due to the failure in meeting one or more of these aspects because of the difficulties in structure control during the synthesis by far. Generally, architecting robust porosity in carbon, expecting to facilitate reactant diffusion in macropores and/or maximizing the active sites exposure in meso/micropores, always results in both excessive defects in carbon framework bringing bulk resistance and inevitable contact resistance from microscopically isolated carbon particles, which then significantly limits the conductivity and impedes the ORR process.[25, 26] On the other hand, for the highly conductive graphitic carbons fabricated through top-down (*e.g.* chemically exfoliated graphene),[22] bottom-up (*e.g.* precursor grown carbon nanotubes (CNTs)) [14] or other methods (*e.g.* catalytically formed

graphitic shells on metal particles),[27] it is hard to obtain the desired porosity.[8, 28] Thus, the fabrication of Fe-N-C materials with both desirable porosity and high conductivity through simple and low-priced process is extremely attractive to enhance the material's catalytic performance, but this has rarely been achieved so far.

Herein, we have developed a porous Fe-N-C hybrid material (denoted as Fe-N-CNT-OPC), which is composed of hierarchically ordered porous carbon (OPC) microblocks interlinked via *in-situ* grown CNTs, for catalyzing ORR. This composite material has successfully combined together the merits such as highly active Fe-N species for ORR, hierarchical porosity for facile reactant transportation and sufficient active site exposure as well as abundant graphitic CNTs to maximize the conductivity. This new material has thus resulted in an outstanding catalytic activity similar to Pt/C for ORR at very low cost.

The hybrid material was synthesized via a bottom-up procedure using dual-templates (Scheme 1). Ordered packed polystyrene (PS) microspheres (Figure S1) were selected as the hard template for 3-dimensionally ordered macropores and F127 was used as a soft template to form mesopores (details included in supplementary information). Resol was employed as the carbon precursor and was dissolved in ethanol together with F127 and iron chlorides. Acetylacetone (acac) was also added into the solution to chelate with Fe ion for better dispersion of Fe species. The solution was impregnated into the voids of PS template and the mesostructure was formed during the evaporation induced self-assembly (EISA) of F127 and resol at ambient temperature. Then the mixture was pre-heated to polymerize resol into rigid resin. Afterward, the residual templates were washed off by a blend of cyclohexane and acetone, leaving a Fe-contained ordered porous resin (Fe-OPR) (Figure S2). Then, it was finely mixed with melamine and graphitic carbon nitride (g-C_3N_4); and the mixture was heated in N_2 at 900 ºC to form Fe-N-CNT-OPC. The hybrid was also synthesized at 750 ºC and 1050 ºC (denoted as Fe-N-CNT-OPC-750 or -1050, respectively); comparative Fe decorated porous carbon with only non-graphitized hollow carbon nanofiber (denoted as Fe-N-CNF-OPC, where CNF represents carbon nanofiber) was also prepared by heating Fe-OPR and melamine/g-C_3N_4 in separate boats in the furnace tube in nitrogen atmosphere at 900 ºC.

The morphology and microstructure of Fe-N-CNT-OPC were firstly investigated by scanning electron microscopy (SEM). Large amount of entangled CNT clusters were observed on OPC microblocks, interlinking them into a network (Figure 1a and S3). Magnified OPC section in the hybrid shows the ordered macropores are *ca.* 200 nm in diameter (Figure S4), which is smaller than PS microspheres (*ca.* 300 nm, Figure S1), possibly due to the shrinkage of the carbon skeleton during the high temperature heating. By looking at the root section of these *in-situ* formed CNTs, it is found that the CNTs grow not only on the surface of OPC, but also from inside its pores (Figure 1b, c and S4). The structure of CNTs was then studied by transmission electron microscopy (TEM), which shows that the CNTs are *ca.* 30 to 100 nm in diameter and form a bamboo-like structure (Figure 1d, e, S5 and S6). High resolution TEM images reveal the wall thickness of the CNTs is between 5 to 10 nm, corresponding to *ca.* 15 to 30 parallel-stacked graphitic layers (Figure 1f and S5). Interestingly, iron nanoparticles are found to be encapsulated either inside each compartment of the bamboo-structure or on the tip of CNTs (Figure 1d, e and S6), which might indicate complex CNT growth mechanisms. The porous carbon section was also observed by TEM as shown in Figure S7. Apart from small-sized mesopores, randomly formed bubble-like pores (*ca.* 10 to 15 nm) also exist. These irregular pores might be the vacancies formed from relocated iron nanoparticles at high temperature. On the other hand, comparative Fe-N-CNF-OPC was also studied under SEM and TEM as shown in Figure S8; but only tubular carbon nanofibers were observed in this material (the amorphous nature of carbon can also confirmed by X-ray diffraction and Raman results below) and they almost exclusively have a very large diameter up to several hundred nanometers.

To further analyze the porosity of the materials, nitrogen adsorption-desorption was performed (Figure S9). The isotherm of Fe-N-CNT-OPC shows a significant hysteresis loop extending from medium to high pressure, which is responsible to dominant mesopores and macropores. The raised adsorption amount at low pressure ($P/P_0<0.05$) also suggests the existence of micropores. The pore distribution was then obtained from the desorption branch of the isotherm. Compared with Fe-N-CNF-OPC, which possesses typical mesopore size distribution centered at *ca.* 5.8 nm and large surface area (1190 m^2 g^{-1}) like other mesoporous carbons prepared by the soft template

method,[25] the Fe-N-CNT-OPC shows a lower surface area (616 m^2 g^{-1}) and wider pore size distribution below 15 nm, which is in agreement with the TEM observations (Figure S7).

To reveal the materials' crystal structure, X-ray diffraction (XRD) was performed (Figure 1g). The XRD patterns show the existence of metallic Fe and magnetite Fe_3O_4 in all samples. Remarkably, the samples with *in-situ* formed CNTs, regardless of the pyrolysis temperature, all give a distinct characteristic peak of graphitic carbon at *ca.* 26 º; while the Fe-N-CNF-OPC only shows a broad curve without any peaks at this position, suggesting the amorphous nature of carbons in this material. Raman spectra of the samples were also collected to further assess their graphitic structure as shown in Figure 1h. Typical G (1587 cm^{-1}) and D (1348 cm^{-1}) bands, which represent the hexagonally bonded carbon atoms inside the graphitic networks and the distorted carbon frames on the defect sites respectively, were obtained. For the samples with CNTs, these two bands become significantly slimmer and the I_G/I_D ratio also increases when the sample is heated at higher temperature, indicating high-graphitic structure was formed as the temperature increased. On the contrary, the Fe-N-CNF-OPC, although heated up to 900 ºC, only gives broad bands at these positions, suggesting its amorphous nature with low graphitization and large amount of distortions in agreement with the XRD results (Table S1). Based on these observations, it has been found that CNTs can only be formed when Fe-OPR is in close physical contact with melamine/g-C_3N_4 during the heating; whilst on the other hand, the isolation of Fe-OPR from melamine/g-C_3N_4 by putting them in the separated boats during the heating would just result in non-graphitic hollow carbon structures with very large diameter on the hierarchical porous carbon.

The chemical composition of materials was analyzed by X-ray photoelectron spectroscopy (XPS). As expected, survey scan of Fe-N-CNT-OPC and Fe-N-CNF-OPC shows the existence of Fe, C, N and O at a comparable level indicating their similar chemical compositions, which is further confirmed by their identical high resolution N1s and Fe2p spectra suggesting the similar chemical status of these elements in the two materials (Figure 2a, S10 and Table S2). Moreover, energy dispersive X-ray spectroscopy (EDS) was also employed to probe the elements' location in Fe-N-CNT-OPC. Firstly, EDS spectra were collected from both the CNT and OPC sections and

identical elemental signals were obtained on both areas (Figure 2b), in agreement with the XPS results. Then, EDS elemental mapping was acquired to further identify the distribution of different species in this hybrid (Figure 2c-g and S11). The mapping shows the homogeneous distribution of C, N and O elements on both OPC and CNTs in Fe-N-CNT-OPC. Unexpectedly, apart from the intensive Fe signals from the iron particles, Fe species were also detected on other sections where no Fe particles were observed. Such finely dispersive Fe species could possibly bond with the neighboring C or N atoms and have been believed to be highly active for ORR.[18]

The materials' activity to electrochemically catalyze ORR was firstly evaluated by cyclic voltammetry (CV) (Figure 3a and S12). Distinct ORR peak centered at *ca.* -0.23 V for Fe-N-CNT-OPC was observed, which is over 100 mV more positive than that of Fe-N-CNF-OPC and clearly indicates a better ORR performance. To gain insight into the ORR process on the materials, rotating disk electrode (RDE) test was then performed in comparison with commercial 20 % Pt/C catalyst (Figure 3b and S13). Remarkably, the Fe-N-CNT-OPC shows a very positive ORR onset potential within 18 mV close to that of Pt/C (Figure 3b inset) in low over-potential. Such positive ORR onset potential has rarely been achieved on Pt-free catalysts and is more positive compared with other non-noble-metal or non-metal catalysts.[5, 11, 19, 29] Apart from this at slightly higher over-potential between -0.1 to -0.2 V, the Fe-N-CNT-OPC gives a very sharp current increase and thus makes its ORR current exceed that of Pt/C, and the ORR current remains stable when the potential goes more negative till -0.8 V. On the other hand, for the sample without *in-situ* formed CNTs (*i.e.* Fe-N-CNF-OPC), the ORR does not appear until *ca.* -0.1 V. This is over 50 mV more negative than the Fe-N-CNT-OPC, and the corresponding reaction current is also lower (Figure 3b and inset). Moreover, the Fe-N-CNT-OPC also possesses similar Tafel slope as Pt/C, which is smaller than that of Fe-N-CNF-OPC, indicating the more facile ORR kinetics on this material. The substantially superior ORR activity on Fe-N-CNT-OPC in comparison with the analogue, considering both the positive onset potential and the large reaction current from the RDE and CV results, has clearly confirmed that the *in-situ* formed CNTs can significantly facilitate the ORR process on the catalyst, especially when the similarity of other aspects (*i.e.* the similar

elemental composition and pore structures of the OPCs) in both materials are taken into consideration.

The materials' ORR efficiency was then quantified on rotating ring-disk electrode (RRDE) (Figure 3c). Remarkably, although Fe-N-CNT-OPC possesses higher ORR catalytic activity compared with the Fe-N-CNF-OPC by giving larger reaction current at low over-potential on the disk, however, its ring current is even lower (Figure 3c inset). This clearly suggests that larger portion of oxygen is directly reduced into OH^- without intermediate peroxides on Fe-N-CNT-OPC. Accordingly, the amount of peroxide and the electron transfer numbers of the catalysts during ORR has been calculated (Figure 3d). As shown on Fe-N-CNT-OPC, only less than 1 % of peroxide yield, corresponding to an electron transfer number up to 3.99, has been obtained at the over-potential as low as -0.1 V. This negligible peroxide yield clearly confirms its extremely high ORR efficiency, which directly and completely reduces O_2 into OH^- through the high efficient $4e^-$ pathway. In contrast, the Fe-N-CNF-OPC has significantly higher peroxide yield and obviously smaller electron transfer number, which suggests substantial portion of O_2 undergoes a low efficient $2e^-$ ORR pathway on this material. Apart from the high activity and efficiency for ORR, the Fe-N-CNT-OPC hybrid also shows full resistance against the methanol crossover and excellent long term stability (Figure S14), which are much superior to Pt/C and make this material promising for fuel cell applications.

Pyrolysis temperature is another factor affecting the ORR performance of the catalysts, thus the samples prepared at different temperatures were also assessed by RDE, RRDE and Tafel analysis (Figure 3e, S15 and S16). The Fe-N-CNT-OPC heated at 900 °C showed a slightly better ORR onset potential than the ones heated at 750 °C or 1050 °C. The inconsiderably inferior performance on the Fe-N-CNT-OPC-750 may result from the relatively lower conductivity from uncompleted graphitization proved by XRD and Raman; whereas for Fe-N-CNT-OPC-1050, despite of its highest graphitic degree, it could suffer from active N and Fe species leaching at high heating temperature as shown by XPS (Figure S10 and Table S2), which compromised its ORR activity.[30] Thus, the best performance of Fe-N-CNT-OPC prepared at 900 °C, considering its positive onset

potential and low Tafel slope value, would possibly be the result of balanced graphitic degree and active species retained at moderate heating temperature. Lastly, this Pt-free material's cost economy was evaluated versus the commercial Pt/C as shown in Figure 3f. Although they give comparative ORR currents the tested potentials (columns with pattern); however, our material developed here is far more economical than the commercial Pt/C (columns with color) by giving out a significantly higher ORR activity per cost unit, due to its much lower price for fabrication.

To sum up, a Fe-N decorated hybrid of carbon nanotubes *in-situ* grown from hierarchically porous carbon has been developed, which has successfully combined the desired merits such as highly active Fe-N species and good conductivity to catalyze ORR, large pore size for facile transportation and sufficient surface area for catalytically active sites exposure. These excellent characters have endowed this material with outstanding ORR catalytic activity closely comparable to or even better than Pt/C, considering its very positive ORR onset potential, quite high ORR current, excellent durability and complete resistance to methanol crossover, which makes this catalyst promising as a potential substitute for Pt/C. Besides, this research has also provided a new route of *in-situ* hybridizing of different forms of carbon to integrate their advantages into one material, which is crucially important for not only ORR but also other electrochemical applications cherishing these characters. Moreover, the material is made via very simple, low-cost and eco-friendly route, which makes it convenient for large-scale fabrication.

Supporting Information

Supporting Information is available from the Wiley Online Library or from the author.

Acknowledgements

This research is financially supported by Australian Research Council (DP1095861, DP130104459).

Received: ((will be filled in by the editorial staff))
Revised: ((will be filled in by the editorial staff))
Published online: ((will be filled in by the editorial staff))

[1] B. C. H. Steele, A. Heinzel, *Nature* **2001**, *414*, 345.
[2] A. Débart, A. J. Paterson, J. Bao, P. G. Bruce, *Angew. Chem. Int. Edit.* **2008**, *47*, 4521.
[3] K. Gong, F. Du, Z. Xia, M. Durstock, L. M. Dai, *Science* **2009**, *323*, 760.

[4] K. Ai, Y. Liu, C. Ruan, L. Lu, G. Lu, *Adv. Mater.* **2013**, *25*, 998.
[5] C. Zhang, N. Mahmood, H. Yin, F. Liu, Y. Hou, *Adv. Mater.* **2013**, *25*, 4932.
[6] S. Wang, L. Zhang, Z. Xia, A. Roy, D. W. Chang, J. B. Baek, L. M. Dai, *Angew. Chem. Int. Edit.* **2012**, *51*, 4209.
[7] P. Chen, T. Y. Xiao, Y. H. Qian, S. S. Li, S. H. Yu, *Adv. Mater.* **2013**, *25*, 3192.
[8] J. Liang, Y. Jiao, M. Jaroniec, S. Z. Qiao, *Angew. Chem. Int. Edit.* **2012**, *51*, 11496.
[9] I. Y. Jeon, S. Zhang, L. Zhang, H. J. Choi, J. M. Seo, Z. Xia, L. M. Dai, J. B. Baek, *Adv. Mater.* **2013**, *25*, 6138.
[10] J. Liang, Y. Zheng, J. Chen, J. Liu, D. Hulicova-Jurcakova, M. Jaroniec, S. Z. Qiao, *Angew. Chem. Int. Edit.* **2012**, *51*, 3892.
[11] Z. S. Wu, S. Yang, Y. Sun, K. Parvez, X. L. Feng, K. Mullen, *J. Am. Chem. Soc.* **2012**, *134*, 9082.
[12] Z. Xiang, Y. Xue, D. Cao, L. Huang, J. Chen, L. M. Dai, *Angew. Chem. Int. Edit.* **2014**, *53*, 2433.
[13] H. W. Liang, W. Wei, Z. S. Wu, X. L. Feng, K. Mullen, *J. Am. Chem. Soc.* **2013**, *135*, 16002.
[14] H. T. Chung, J. H. Won, P. Zelenay, *Nat. Commun.* **2013**, *4*, 1922.
[15] J. Y. Cheon, T. Kim, Y. Choi, H. Y. Jeong, M. G. Kim, Y. J. Sa, J. Kim, Z. Lee, T. H. Yang, K. Kwon, O. Terasaki, G. G. Park, R. R. Adzic, S. H. Joo, *Sci. Rep.* **2013**, *3*.
[16] G. Zhang, B. Y. Xia, X. Wang, X. W. Lou, *Adv. Mater.* **2013**, *26*, 2408.
[17] L. Zhang, Z. Xia, *J. Phys. Chem. C* **2011**, *115*, 11170.
[18] W. Qi, W. Liu, B. Zhang, X. Gu, X. Guo, D. Su, *Angew. Chem. Int. Edit.* **2013**, *52*, 14224.
[19] Y. Zheng, Y. Jiao, L. Ge, M. Jaroniec, S. Z. Qiao, *Angew. Chem. Int. Edit.* **2013**, *52*, 3110.
[20] A. Serov, K. Artyushkova, P. Atanassov, *Adv. Energy Mater.* **2014**, doi: 10.1002/aenm.201301735.
[21] Y. Chang, F. Hong, C. He, Q. Zhang, J. Liu, *Adv. Mater.* **2013**, *25*, 4794.
[22] Y. Li, W. Zhou, H. Wang, L. Xie, Y. Liang, F. Wei, J. C. Idrobo, S. J. Pennycook, H. Dai, *Nat. Nanotechnol.* **2012**, *7*, 394.
[23] Z. Wen, S. Ci, F. Zhang, X. Feng, S. Cui, S. Mao, S. Luo, Z. He, J. Chen, *Adv. Mater.* **2014**, *24*, 1399.
[24] J. S. Lee, G. S. Park, S. T. Kim, M. Liu, J. Cho, *Angew. Chem. Int. Edit.* **2012**, *52*, 1026.
[25] J. Liang, X. Du, C. Gibson, X. W. Du, S. Z. Qiao, *Adv. Mater.* **2013**, *25*, 6226.
[26] W. Yang, T. P. Fellinger, M. Antonietti, *J. Am. Chem. Soc.* **2010**, *133*, 206.
[27] Y. Hu, J. O. Jensen, W. Zhang, L. N. Cleemann, W. Xing, N. J. Bjerrum, Q. Li, *Angew. Chem. Int. Edit.* **2014**, *53*, 3675.
[28] Z. S. Wu, Y. Sun, Y. Z. Tan, S. Yang, X. L. Feng, K. Mullen, *J. Am. Chem. Soc.* **2012**, *134*, 19532.
[29] D. Deng, L. Yu, X. Chen, G. Wang, L. Jin, X. Pan, J. Deng, G. Sun, X. Bao, *Angew. Chem. Int. Edit.* **2013**, *52*, 371.
[30] S. B. Yang, X. L. Feng, X. C. Wang, K. Mullen, *Angew. Chem. Int. Edit.* **2011**, *50*, 5339.

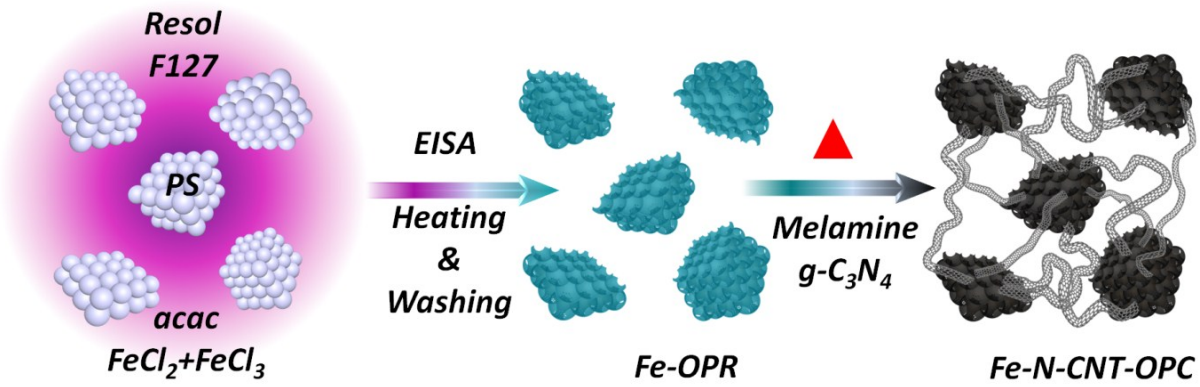

Scheme 1. Synthetic procedure of the Fe-N-CNT-OPC material.

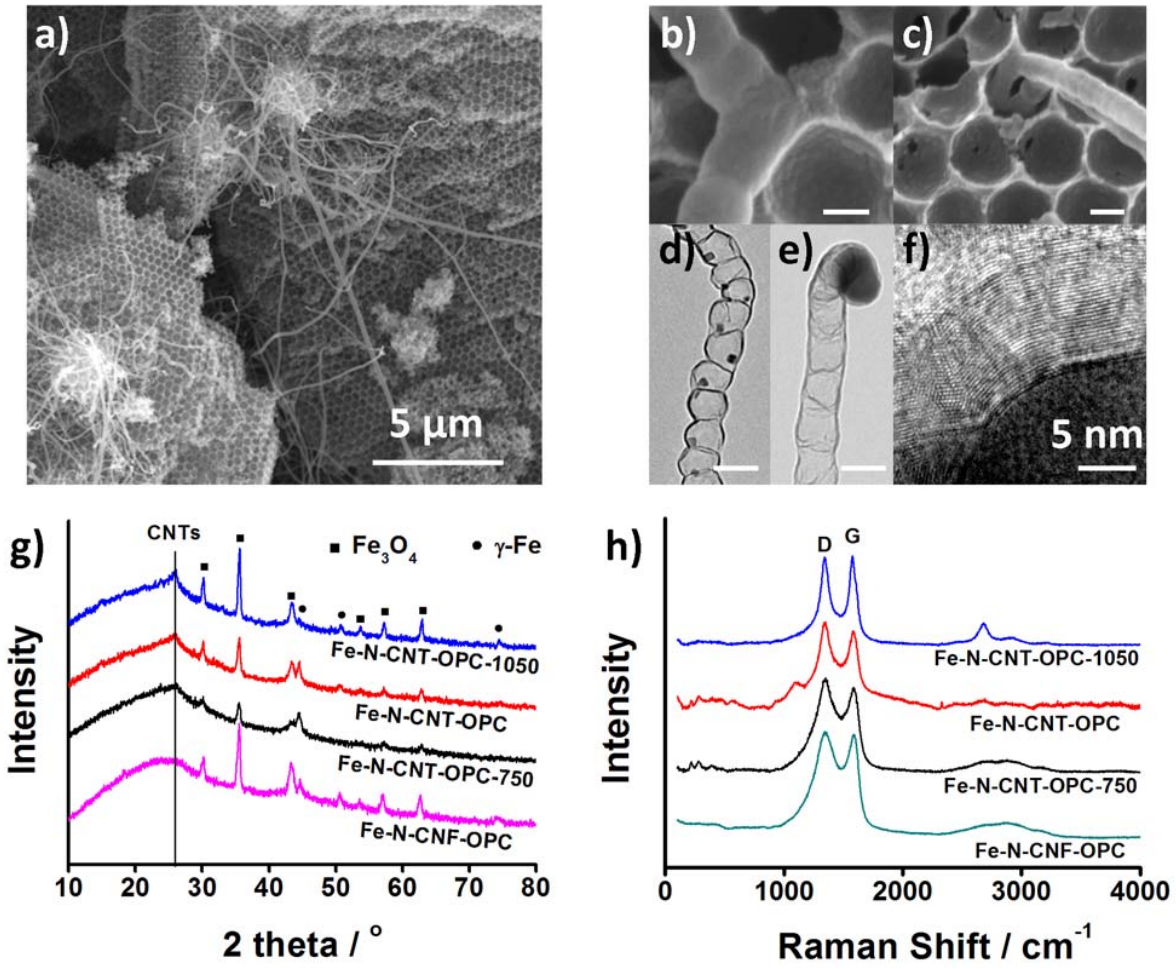

Figure 1. Typical structural characterizations of Fe-N-CNT-OPC and analogues. (a-c) SEM and (d-f) TEM images of Fe-N-CNT-OPC; (g) XRD patterns; (h) Raman spectra of the samples. The scale-bars in b-e correspond to 100 nm.

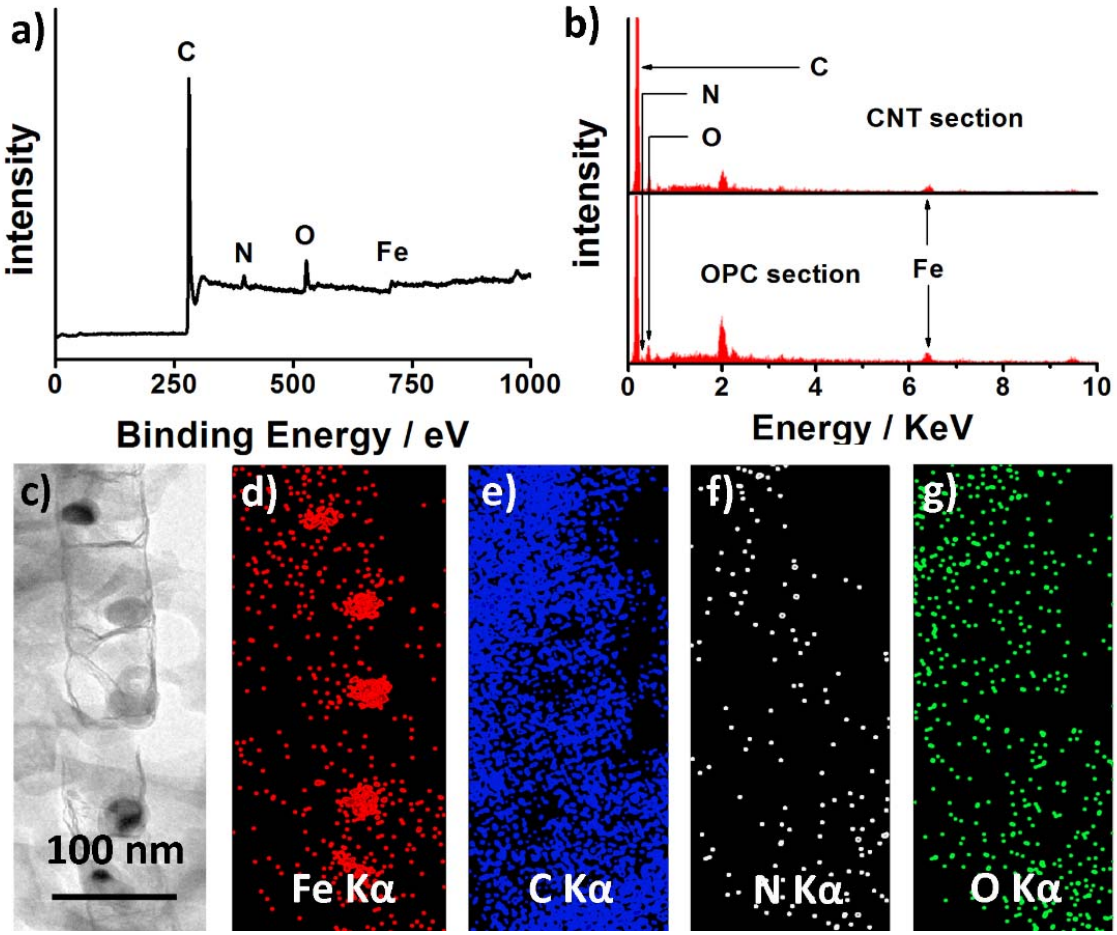

Figure 2. Chemical composition analysis of Fe-N-CNT-OPC. (a) XPS survey scan; (b) EDS spectra of CNT section (above) and OPC section (below). Peaks at *ca.* 2 keV corresponds to Pt coating for SEM; (c-g) TEM image and corresponding elemental mappings of the same area.

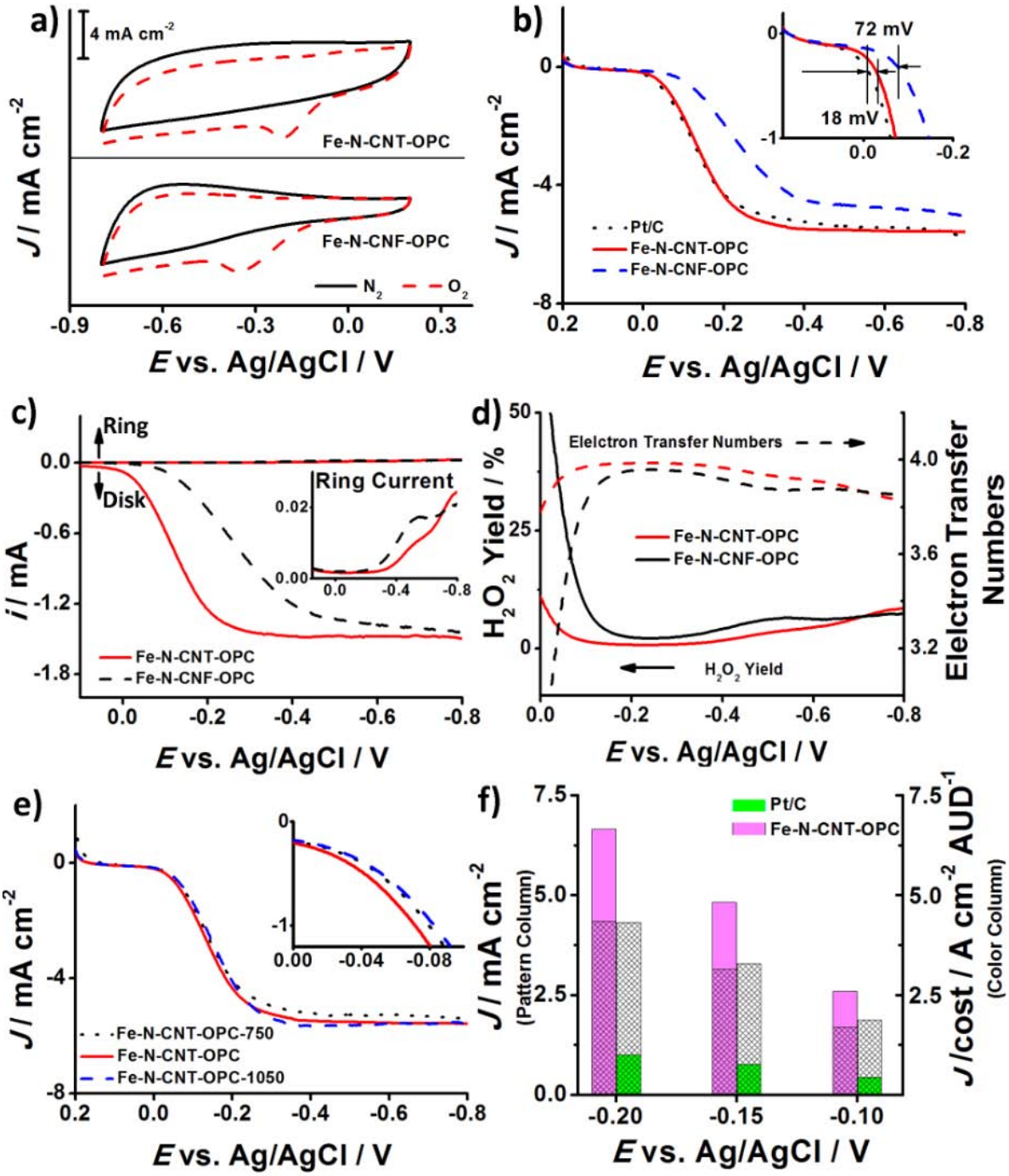

Figure 3. ORR evaluations of Fe-N-CNT-OPC and analogues. (a) CV curves in O_2 and N_2 saturated 0.1 M KOH solution; (b) RDE and (c) RRDE voltammograms at 1600 rpm in O_2 saturated 0.1 M KOH solution; (d) Peroxide yield (solid) and electron transfer numbers (dash); (e) RDE voltammograms of the analogues pyrolyzed at different temperatures; (f) ORR current (pattern column) and the corresponding cost-efficiency (color column) of the samples at different potentials. The insets in b, c and e have the same title and unit as the corresponding figures. The catalyst loading on the electrode for all tests is 80 μg.

The table of contents entry

A Fe-N decorated hybrid material of carbon nanotubes *in-situ* grown from porous carbon microblocks has been designed and constructed. This material has successfully combined the desirable merits for oxygen reduction reaction (ORR), such as highly active Fe-N species, good conductivity, large pore size and sufficient surface area. These structural advantages have brought this low-priced material an outstanding catalytic performance for ORR closely comparable with Pt/C of the same quantity.

Keyword: hybrid carbon, carbon nanotube, in-situ growth, oxygen reduction, non-noble-metal

Ji Liang, Rui Feng Zhou, Xue Min Chen, You Hong Tang and Shi Zhang Qiao*

Title: Fe-N Decorated Hybrid of CNTs Grown on Hierarchically Porous Carbon for High Performance Oxygen Reduction

ToC figure

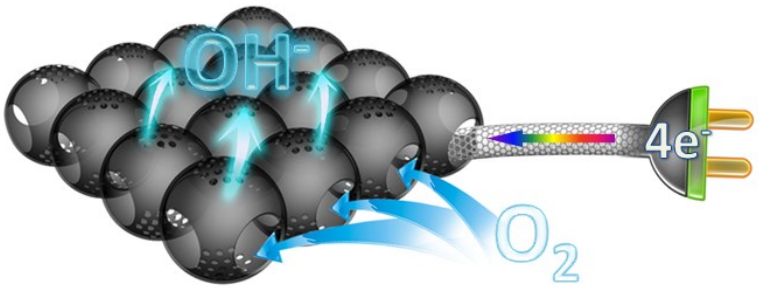

((Supporting Information can be included here using this template))

Supporting Information

Fe-N Decorated Hybrid of CNTs Grown on Hierarchically Porous Carbon for High Performance Oxygen Reduction

*Ji Liang, Rui Feng Zhou, Xue Min Chen, You Hong Tang and Shi Zhang Qiao**

[*] Prof. Shi Zhang Qiao, Ji Liang, Rui Feng Zhou
School of Chemical Engineering, the University of Adelaide,
Adelaide, SA 5005, Australia
E-mail: s.qiao@adelaide.edu.au

Dr. You Hong Tang
Centre for Nano Scale Science and Technology,
School of Computer Science, Engineering, and Mathematics, Flinders University,
Adelaide, SA 5042, Australia

Xue Min Chen
School of Materials Science and Engineering, Tianjin University,
Tianjin, 300072, China

I. Experimental Section

1. Chemicals

Potassium persulfate ($K_2S_2O_8$, 99 wt. %), melamine (99 wt. %), styrene (ST, 99 %), polyvinyl pyrrolidone (PVP, MW 44000, 99 %), sodium hydroxide pellets (NaOH, 99 %), ethanol (EtOH, absolute), phenol (99 %), formaldehyde solution (37 %), ferrous chloride tetrahydrate ($FeCl_2 \cdot 4H_2O$, 98 %), ferric chloride hexahydrate ($FeCl_3 \cdot 6H_2O$, 97 %), cyclohexane (99.5 %), acetone (> 99 %), acetylacetone (acac, 99 %) were purchased from Sigma-Aldrich and directly used without treatment or purification.

2. Preparation of polystyrene (PS) spheres

Typically, 13 ml ST was firstly washed with 4 ml 10 wt. % NaOH solution to remove the stabilizer. Then, the washed ST was added to 100 ml water with 0.5 g PVP in a triple-neck flask. The mixture was fluxed 70 °C with stir (600 rpm) for 30 min with nitrogen purged in. Afterward, 20 ml of aqueous solution containing 0.3 g $K_2S_2O_8$ was injected into the flask to initiate the polymerization reaction of ST. The mixture was stirred at 600 rpm at 70 °C for 24 h. The milk-like product was then centrifuged and washed with water for three times. Finally, the PS microspheres were dispersed in EtOH or water by ultrasonication and the suspension was dried in

an evaporation dish at room temperature, forming 3-dimensionally ordered packed PS template of about 10 g.

3. Preparation of resol

Typically, 10 g of phenol was heated until melt at 42 °C in a capped bottle. Then 2.1 g of 20 % NaOH aqueous solution was added dropwise with stir at 100 rpm. Afterward, 17.7 g of 37 wt. % formaldehyde solution was added by dropwise and the temperature was raised to 70 °C. The mixture was heated and stirred for another hour and then cooled to room temperature. After that, the pH of the solution was adjusted with 2 M HCl solution to neutral. Afterward, water was rotary-vaporated at 45 °C and the product was diluted into 20 wt. % EtOH solution. During this process, the NaCl sediment was filtered. The prepared resol solution can be stored in fridge for several months.

4. Preparations of Fe-N-CNT-OPC and Fe-N-CNF-OPC

1.7 g F127 was dissolved in 17 ml EtOH at 50 °C with continuous stir for 30 min. Then 8.5 g of above prepared 20 wt. % resol solution was added and kept stirred for another 20 min. Then, 0.48 g $FeCl_3 \cdot 6H_2O$ and 0.36 g $FeCl_2 \cdot 4H_2O$, which were dissolved in 16 ml EtOH, were added into the solution of Resol and F127. A dark blue color immediately appeared when the two solutions were mixed together. Then 352 μl acetylacetone was added into the solution with stir, and the color changed from dark blue into reddish brown after stirring for several seconds. The above solution was added by drop into the evaporation dish containing 10 g of dry PS template. After all the solution was added, the dish was kept under vacuum until no bubble came out from the PS template. This takes about 10 min. Then, the mixture was dried in air at room temperature overnight to form Fe/PS/Resl/F127 precursor. After that, the material was heated at 100 °C for 24 h in air and then at 350 °C in N_2 for 3.5 h with a ramp rate of 1 °C min^{-1}, and after this, the color changed from reddish-brown into dark blue. The obtained solid was slightly crashed and washed by excessive amount of acetone and cyclohexane mixture (1:1 in volume) at 60 °C twice under continuous stir to remove the residual template. The washing solvent could be recycled and reused by distillation to remove the dissolved components. The powder was filtered and dried at 100 °C overnight, resulting a porous Fe-contained resin (denoted as the Fe-OPR in the text); and a beautiful color of green-indigo from reversed opal structure containing Fe can be observed. The powder was finely ground with 5 times weight of melamine and 5 times weight of g-C_3N_4 (prepared by heating melamine in air at 550 °C for 4 h) in an agate mortar and the mixture was heated in the following program in N_2 to prepare Fe-N-CNT-OPC:

Room temperature → 60 °C (ramp rate: 1 °C min^{-1}, kept for 3 h) → 600 °C (ramp rate: 2.3 °C min^{-1}, kept for 4 h) → 900 °C (ramp rate: 5 °C min^{-1}, kept for 3 h) → room temperature

To prepare Fe-N-CNF-OPC with non-graphitized hollow carbon fibers, same amount of melamine and g-C_3N_4 was put in a separate boat with cover. Then the materials underwent the same heating process as above.

The above amount of precursor, which was started from 10 g of PS templates, would result in *ca.* 1 g of the final catalyst material. To prepare 1 g of Fe-N-CNT-OPC catalyst, the price of all chemicals, solvents and electricity was calculated according to the retail price in Australia to be less than 8.15 Australian Dollars, while price of commercial Pt/C catalyst containing 20 wt. % Pt is about 50 Australian Dollars per gram if it is purchased in bulk quantity. Considering the much lower price of the chemicals for bulk purchase, the cost of our catalyst would be significantly lowered if fabricated in large scale.

5. Characterizations

Nitrogen adsorption-desorption isotherm was collected on Tristar II (Micrometrics) at 77 K. Pore size distribution of the materials was obtained by Barrett-Joyner-Halenda (BJH) model using the adsorption branch on the isotherm. The specific surface area of the materials was calculated using adsorption data at the pressure range of $P/P_0 = 0.05\text{-}0.3$ by Brunauer-Emmett-Teller (BET) model.

Microstructures of the samples were examined on TEM (Tecnai G2 Spirit TEM) and SEM (Quanta FEG 450, FEI). High resolution (HR) TEM images were acquired on JEM-2100 microscopy. Elemental mapping of the materials was obtained through the EDAX detector attached on JEM-2100. XPS analysis was conducted on AXIS Ultra spectrometer (Kratos Analytical Ltd.) with monochromated Al Kα radiation at *ca.* 5×10^{-9} Pa.

All Raman spectra were collected on LabRAM (Horiba Ltd) with 532 nm laser.

X-Ray diffraction was performed on Miniflx-600 (Rigaku Ltd.) at ambient conditions using a Cu Kα X-ray.

6. Electrochemical test

For the electrochemical test, 2 mg of the catalyst was dispersed in 1 ml of DI water (18.2 MΩ). The mixture was slightly ultrasonicated to obtain a homogenous catalyst ink.

To prepare the working electrode for electrochemical measurements, 40 µl of the ink was dipped on a mirror polished glass carbon electrode. Then, 10 µl of 0.5 wt. % Nafion aqueous solution was dipped on the electrode and dried at room temperature as binder (for the long term durability tests and methanol crossover tests of the materials, the Nafion loading amount was 10 µl of 1 wt. % to prevent form any catalyst detachment from the electrode surface). After that, the working electrode was inserted into the cell setup, which is composed of a platinum counter electrode, an Ag/AgCl/KCl (4 M) reference electrode and a glass cell containing 100 ml of 0.1 M KOH aqueous

electrolyte.

Cyclic voltammetry (CV) experiments were performed on an electrochemical analysis station (CHI 760 C, CH Instruments, USA) at 100 mV s^{-1}. Before the test, an O_2/N_2 flow was used to purge through the electrolyte in the cell for 20 min to saturate it with O_2/N_2.

For the rotating disk electrode (RDE) and rotating ring-disk electrode (RRDE) test, the same working electrode was prepared as for CV and the test was conducted on CHI 760 C. A Pt wire and an Ag/AgCl/KCl (4 M) were used as the counter and reference electrodes, respectively. The linear sweep voltammograms of the catalysts were recorded in O_2 saturated 0.1 M KOH with a scan rate of 5 mV s^{-1} at various rotating speeds from 0 to 2000 rpm for ORR. After each scan, the electrolyte was saturated with O_2 again for 5 minutes. The sample was tested 3 times to avoid any incidental error.

For the RRDE test, the working electrode was prepared as illustrated above and the test was conducted on CHI 760 C. A Pt wire and an Ag/AgCl/KCl (4 M) were used as the counter and reference electrodes, respectively. The linear sweep voltammograms were recorded in O_2 saturated 0.1 M KOH at 1600 rpm. The disk was set to scan at 5 mV s^{-1} from 0.2 V to -0.8 V and the ring was set at 0.5 V. The collecting efficiency of the RRDE (N) was 0.37.

The peroxide yield (HO_2^-%) and the electron transfer number (n) was calculated as follows:

$$HO_2^-\% = 200 \times I_r / N / (I_d + I_r / N)$$

$$n = 4 \times I_d / (I_d + I_r / N)$$

where I_d is the disk current and I_r is the ring current.

The materials' resistance to methanol crossover effect and stability were test in the same setup as for the RDE test in the N_2/O_2 saturated 0.1 M KOH aqueous electrolyte. The stability test was performed at a static potential of -0.3 V for the chronoamperometry at room temperature with the working electrode rotating at 1600 rpm. The long-term CV durability test was also performed for 1500 cycles with scan rate of 200 mV/s in 0.1 M KOH solution with 50 sccm oxygen bubbled into the cell.

II. Supplementary Results

Table S1. Raman spectra analysis of the samples

I_G/I_D Sample	Area Ratio	Height Ratio
Fe-N-CNT-OPC-1050	0.68	1.07
Fe-N-CNT-OPC	0.52	0.89
Fe-N-CNT-OPC-750	0.42	0.83
Fe-N-CNF-OPC	0.33	0.85

Table S2. Elemental composition of the samples obtained from the XPS results in Figure 2a and S10.

at. % Sample	C	N	Fe	O
Fe-N-CNT-OPC-750	84.53	7.98	0.38	7.12
Fe-N-CNT-OPC	91.49	3.53	0.28	4.70
Fe-N-CNT-OPC-1050	94.20	1.52	0.15	4.13
Fe-N-CNF-OPC	93.30	3.47	0.20	3.03

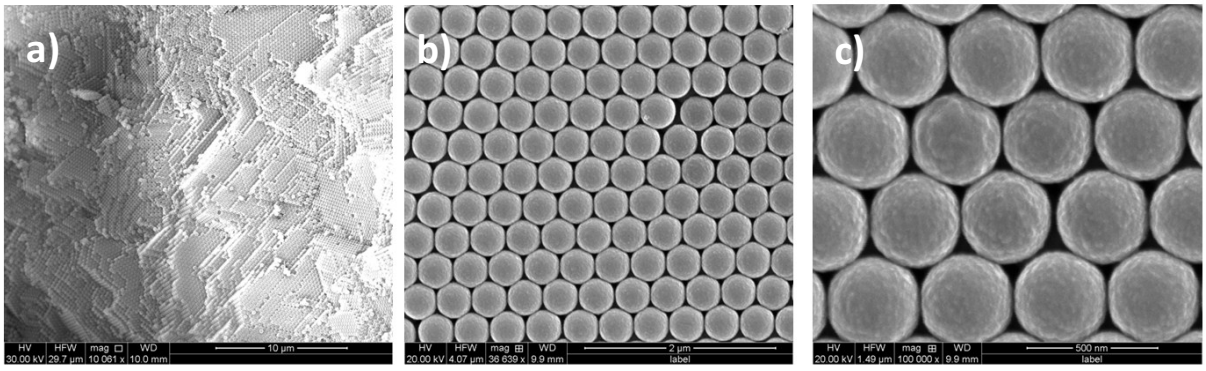

Figure S1. SEM images at different magnifications of polystyrene (PS) microspheres ordered packed as the template for the 3-dimensional macropores in the material.

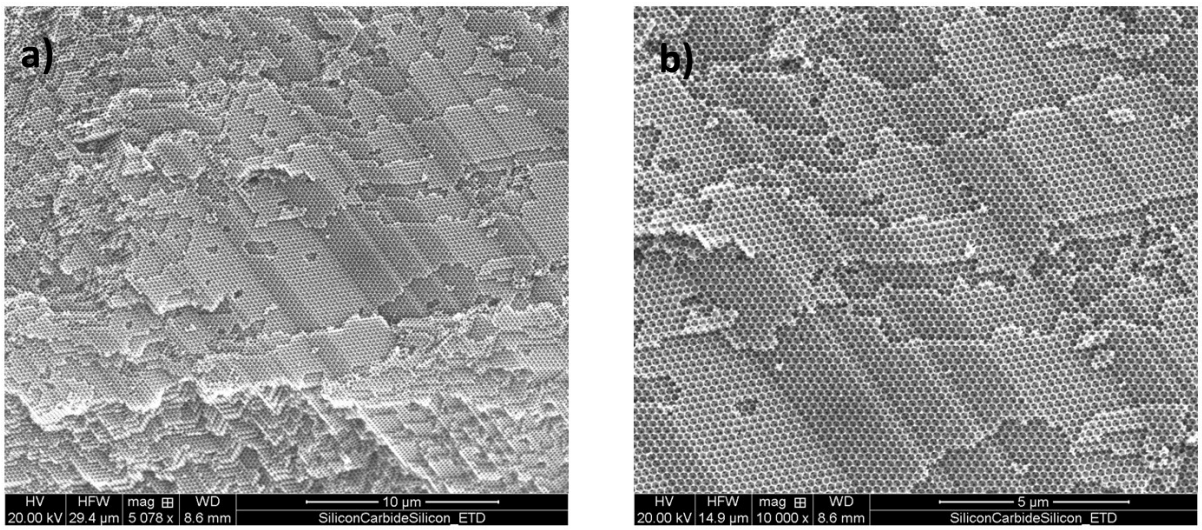

Figure S2. SEM images at different magnifications of Fe contained resin with 3-dimensionally ordered macropores after washed with the acetone/cyclohexane solvent.

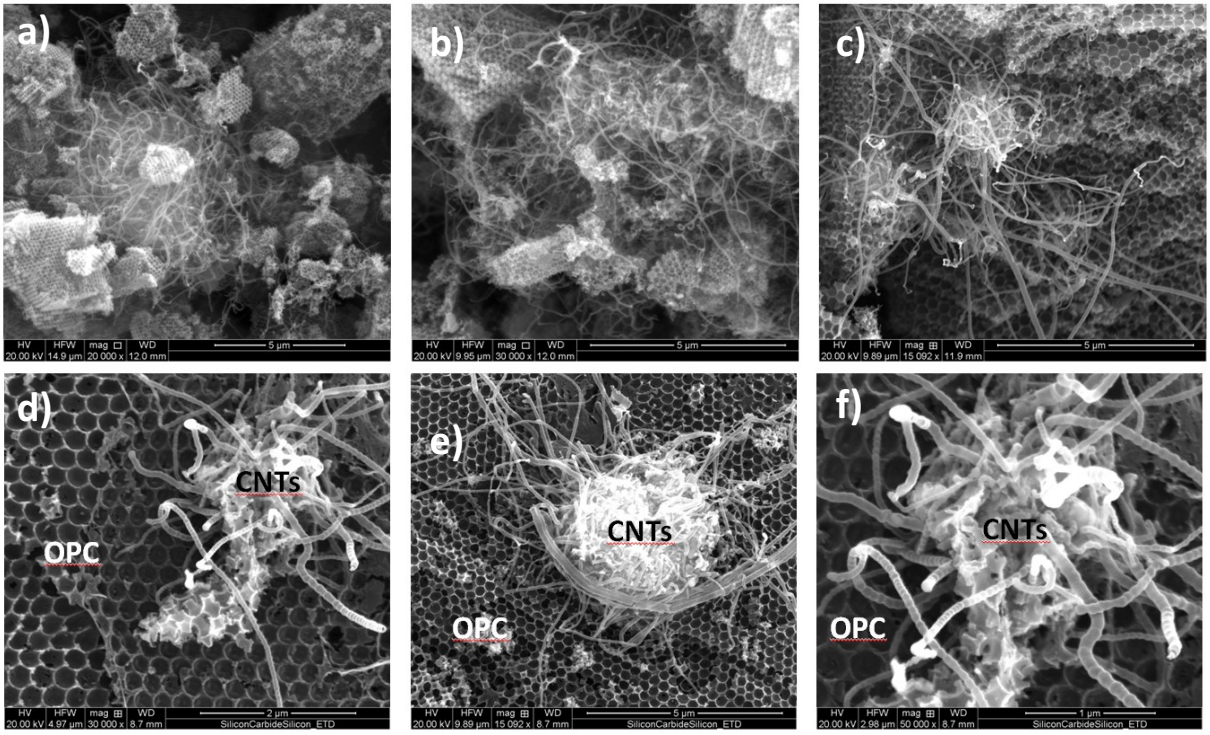

Figure S3. SEM images of Fe-N-CNT-OPC; (a-c) low magnification and (d-f) high magnification.

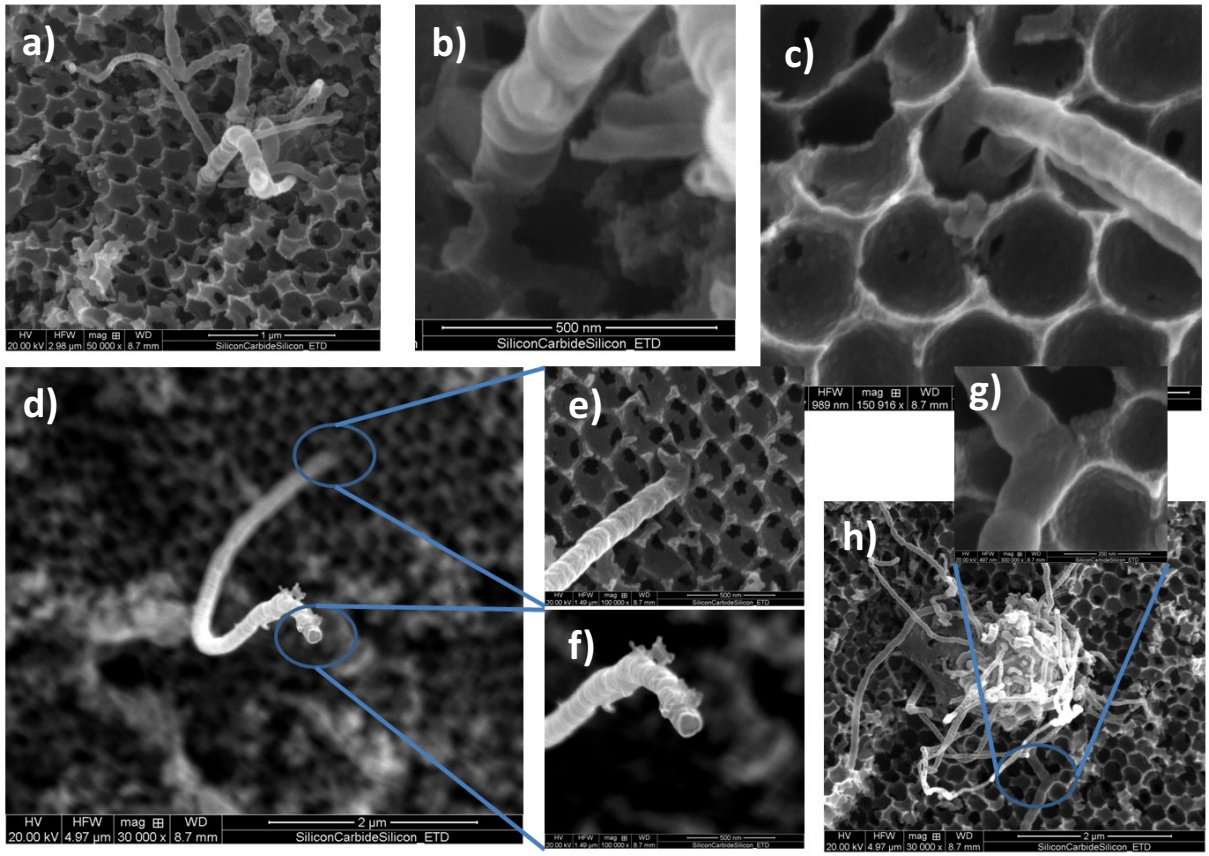

Figure S4. SEM images showing the rooting and the tip sections of CNTs on the porous carbon blocks (OPC) in Fe-N-CNT-OPC sample.

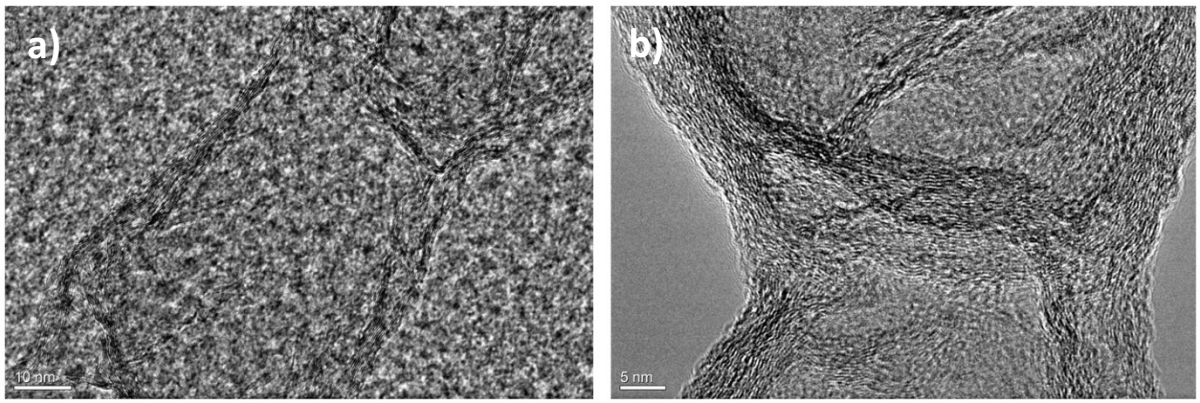

Figure S5. High resolution TEM images showing the bamboo structured *in-situ* grown CNTs in the Fe-N-CNT-OPC sample.

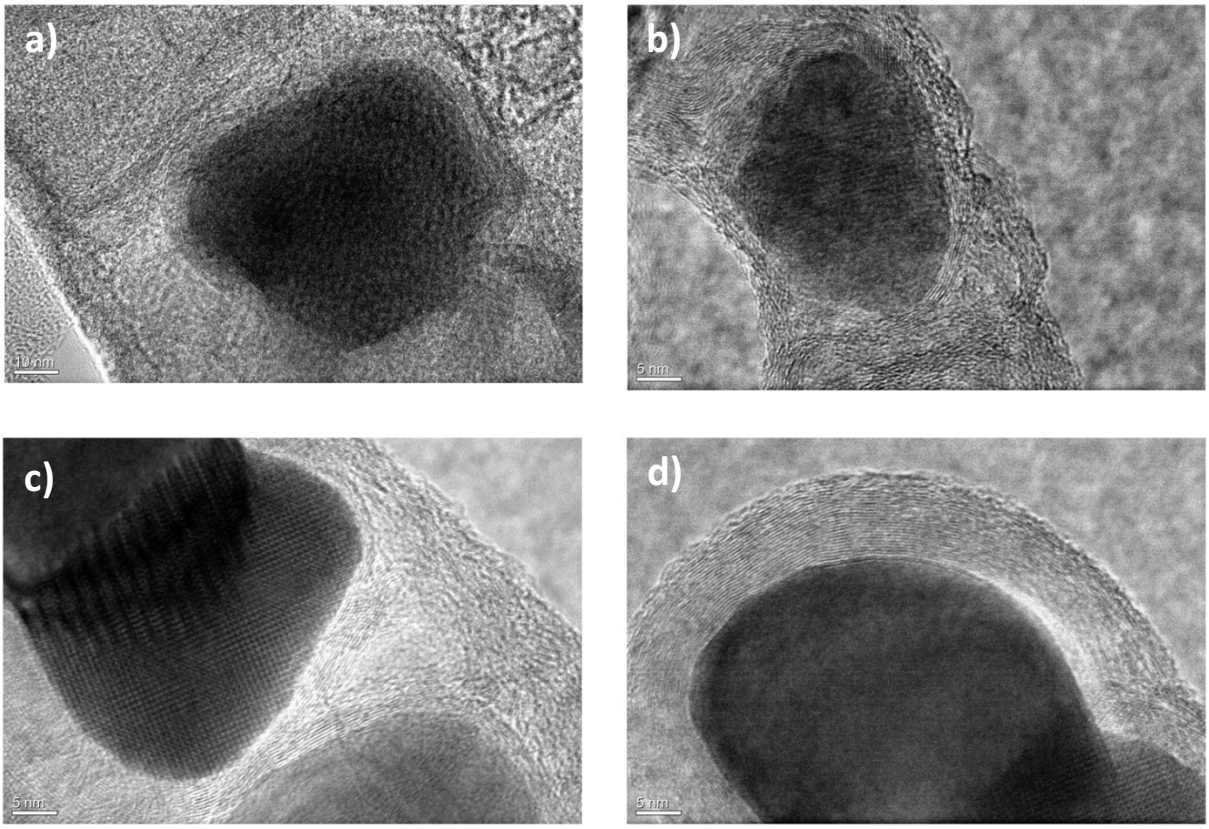

Figure S6. High resolution TEM images showing the iron particles encapsulated either in the chambers of the bamboo structures (a-c) or on the tip (d) of the CNTs in Fe-N-CNT-OPC sample.

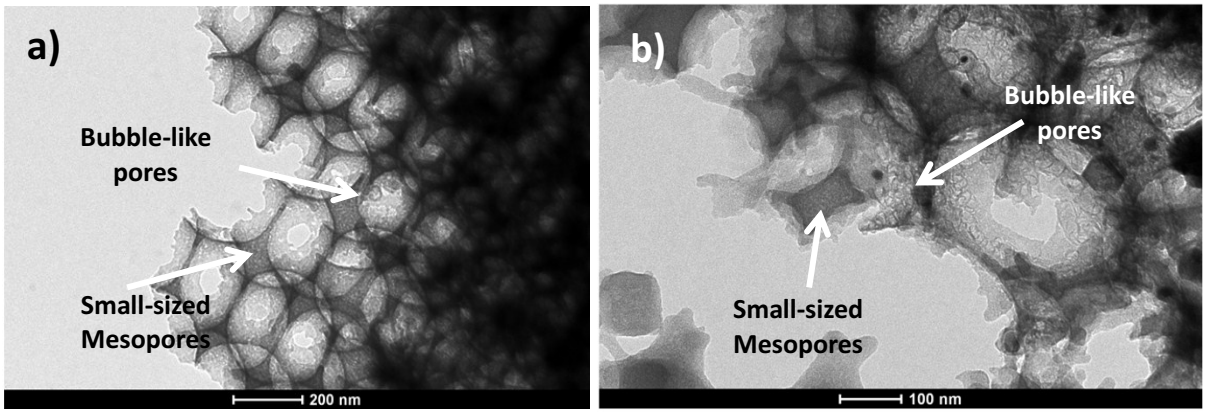

Figure S7. TEM images of the OPC sections in Fe-N-CNT-OPC showing both small-sized mesopores from F127 soft template and the disordered pores which might result from the relocated iron nanoparticles during the high temperature pyrolysis.

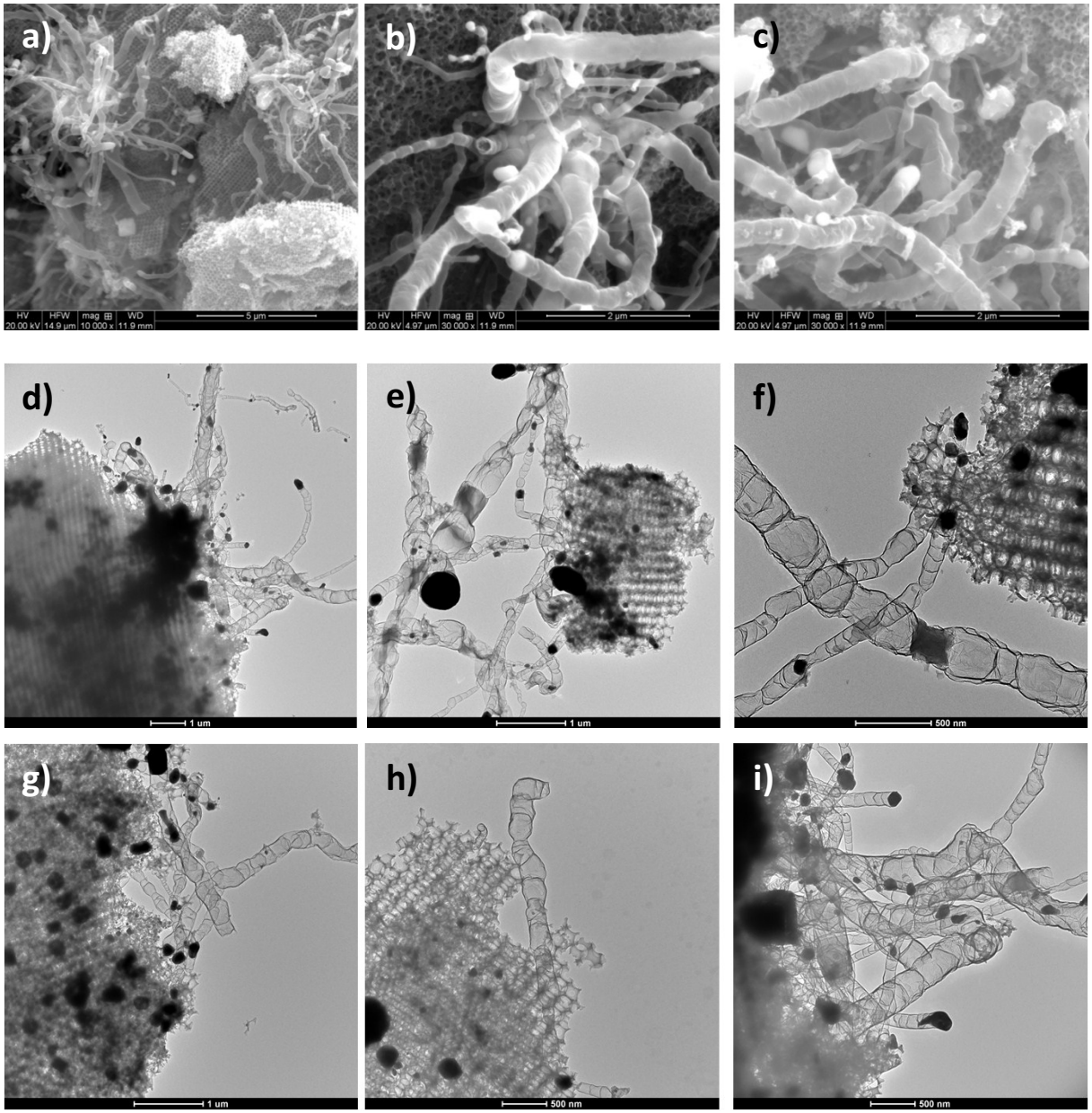

Figure S8. SEM (a-c) and TEM (d-i) images of the comparative Fe-N-CNF-OPC hybrid samples with hollow carbon nanofibers with diameter of several hundred nanometers.

The TEM images also show large amount of tubular hollow carbon nanofibers (CNF) with very big diameter up to several hundred nanometers, which is in agreement with the SEM results. Porous carbon with ordered 3-dimentioanlly macropores has also been observed, which is the same as the OPCs in the Fe-N-CNT-OPC sample and suggests that the growth of CNTs or CNFs does not significantly affect the structures of the substrate porous carbon material.

On the other hand, although both Fe-N-CNT-OPC and Fe-N-CNF-OPC materials can "grow" certain forms of tubular carbon (and in some aspect they look very similar, *e.g.* tubes with large length); however, their microstructures are not the same. The fundamental difference between these two materials can be revealed through XRD and Raman results, which clearly show that the "CNF"

in the Fe-N-CNF-OPC material is not crystalized/graphitized and thus would be poor in electrical/mechanical properties compared with the highly graphitized CNTs in Fe-N-CNT-OPC material.

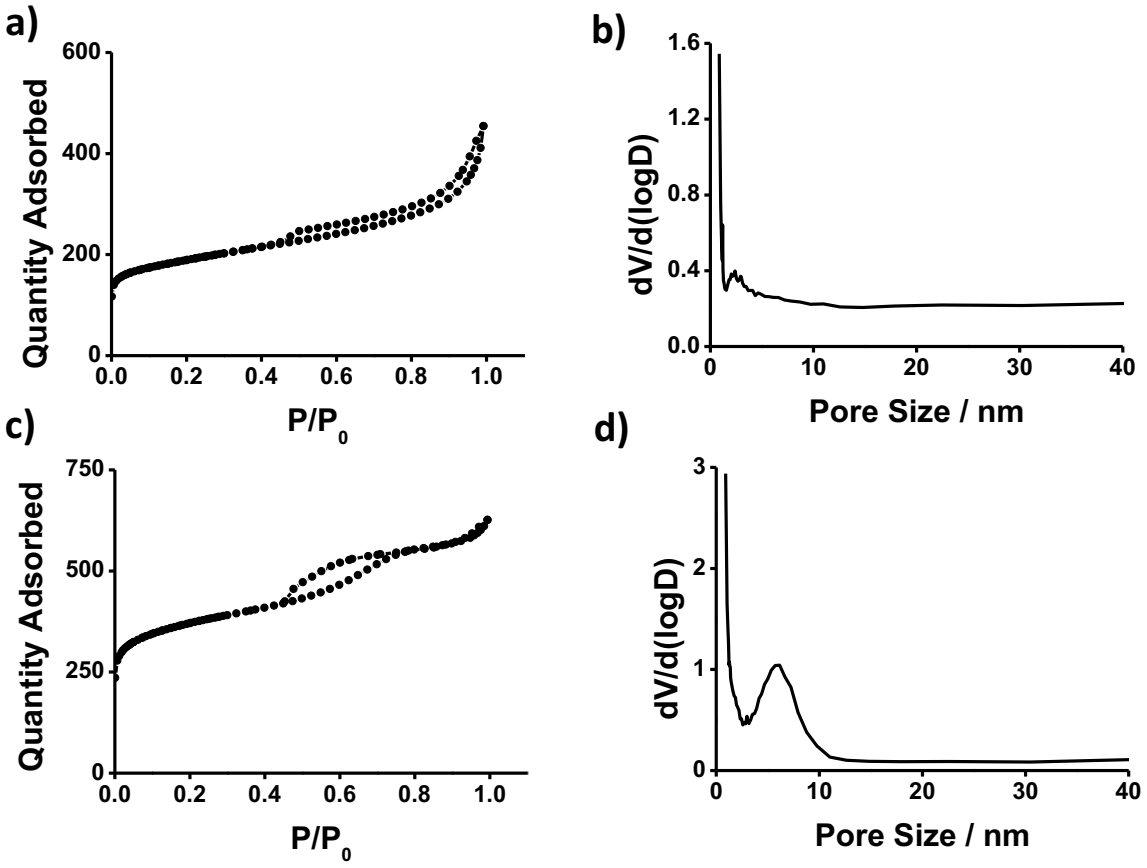

Figure S9. Nitrogen adsorption-desorption isotherms and the corresponding pore size distributions of Fe-N-CNT-OPC (a, b) and Fe-N-CNF-OPC (c, d).

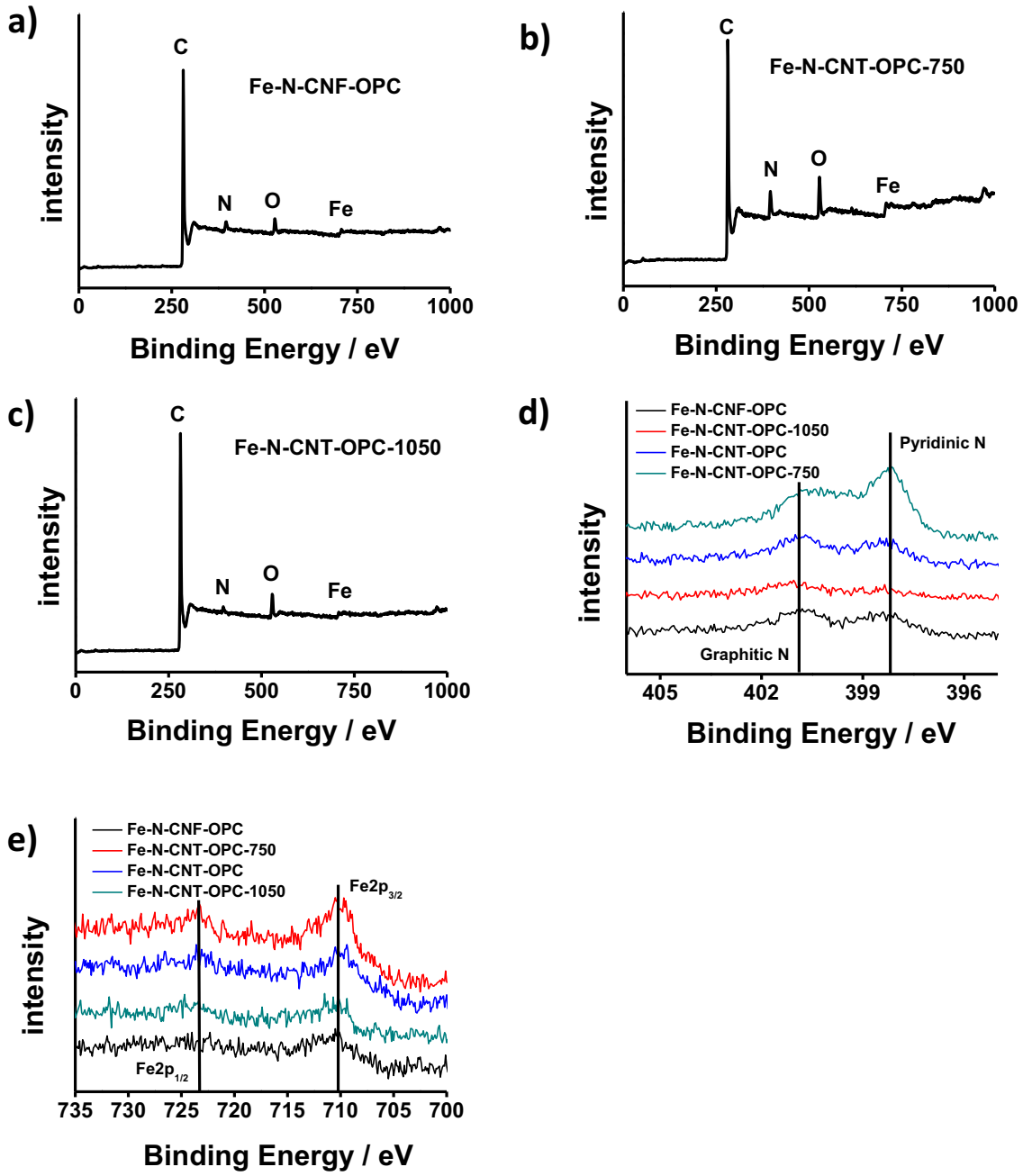

Figure S10. XPS survey scan of (a) Fe-N-CNF-OPC. (b) Fe-N-CNT-OPC-750 and (c) Fe-N-CNT-OPC-1050; and the corresponding high resolution N1s (d) and Fe2p (e) spectra of the samples.

It can be found that the Fe-N-CNT-OPC and Fe-N-CNF-OPC (synthesized at the same temperature of 900 °C) show very similar N and Fe high resolution spectra, which indicates the similar chemical status of these two species in both materials. On the other hand, for the Fe-N-CNT-OPC samples synthesized at different temperatures, the content of pyridinic N species significantly decreased as the heating temperature increased, indicating the loss of active sites on the materials when heated at high temperature.

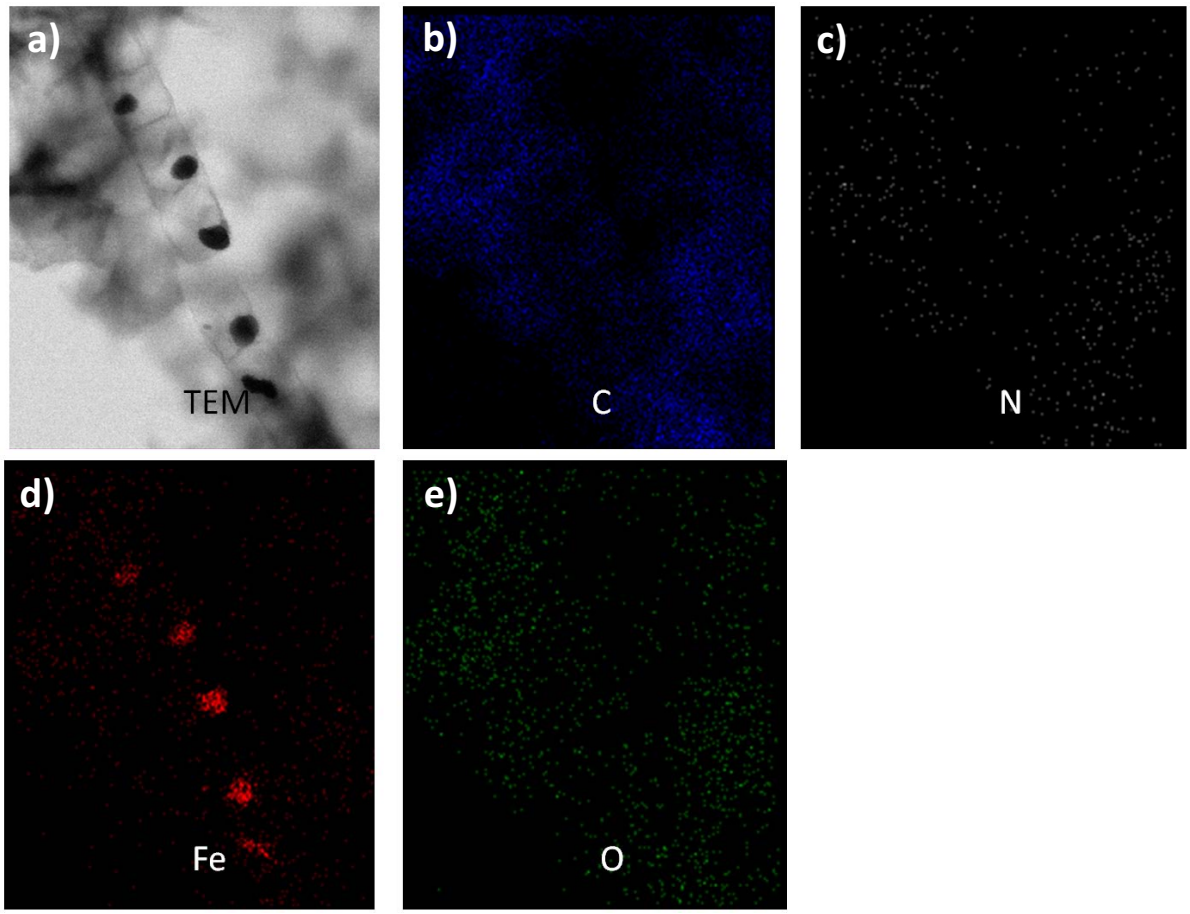

Figure S11. TEM image of Fe-N-CNT-OPC showing the CNT and OPC sections (a) and the corresponding elemental distributions in this area (b-e).

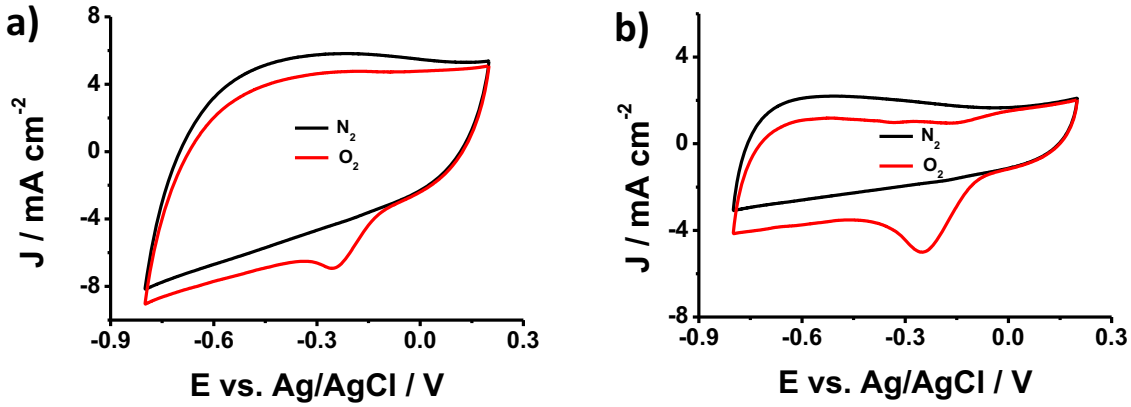

Figure S12. CV loops of Fe-N-CNT-OPC-750 (a) and Fe-N-CNT-OPC-1050 (b) in 0.1 M KOH aqueous electrolyte saturated with N_2 or O_2.

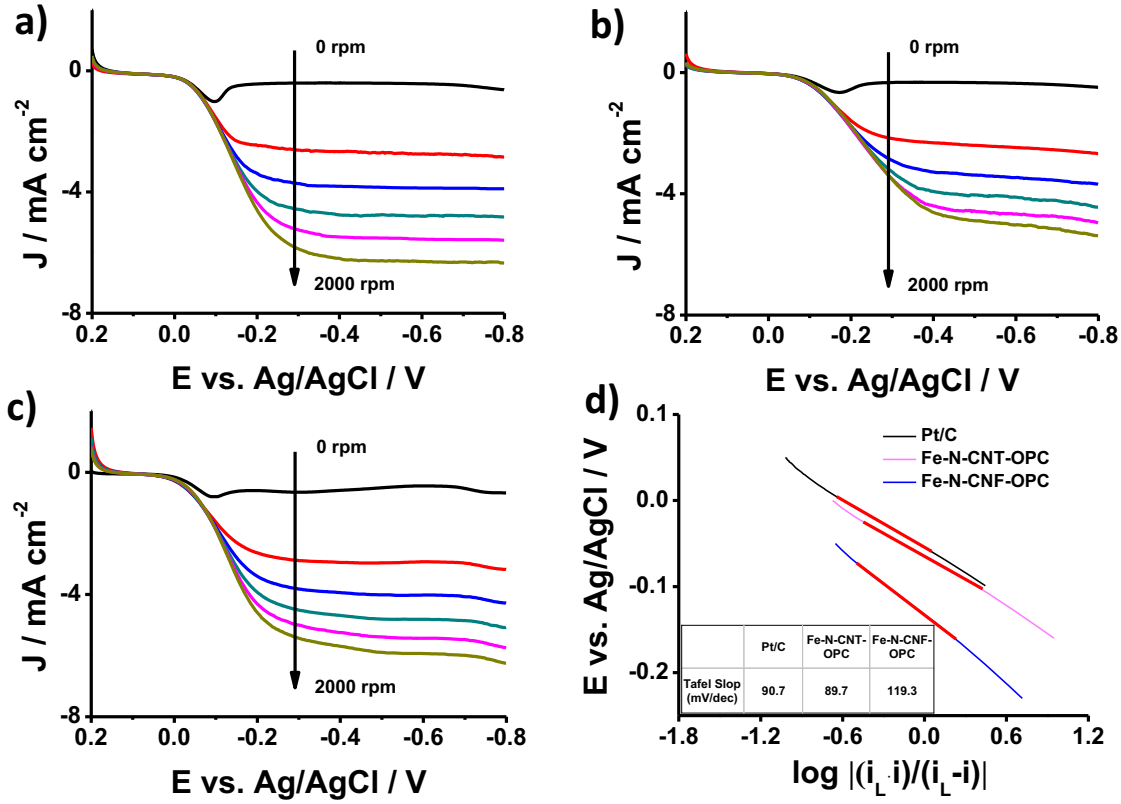

Figure S13. RDE voltammograms of (a) Fe-N-CNT-OPC, (b) Fe-N-CNF-OPC and (c) Pt/C at different rotating speeds from 0 to 2000 rpm with an increment of 400 rpm between each voltammogram; and the corresponding Tafel plots (d) obtained from the voltammogram at 1600 rpm.

The Fe-N-CNT-OPC and Pt/C show a similar slope value, which indicates their comparable ORR activity, in agreement with their close electrochemical performances; while the Fe-N-CNF-OPC sample gives a higher Tafel slope value, which reveals its higher resistance in the ORR process resulting in poor catalytic performance.

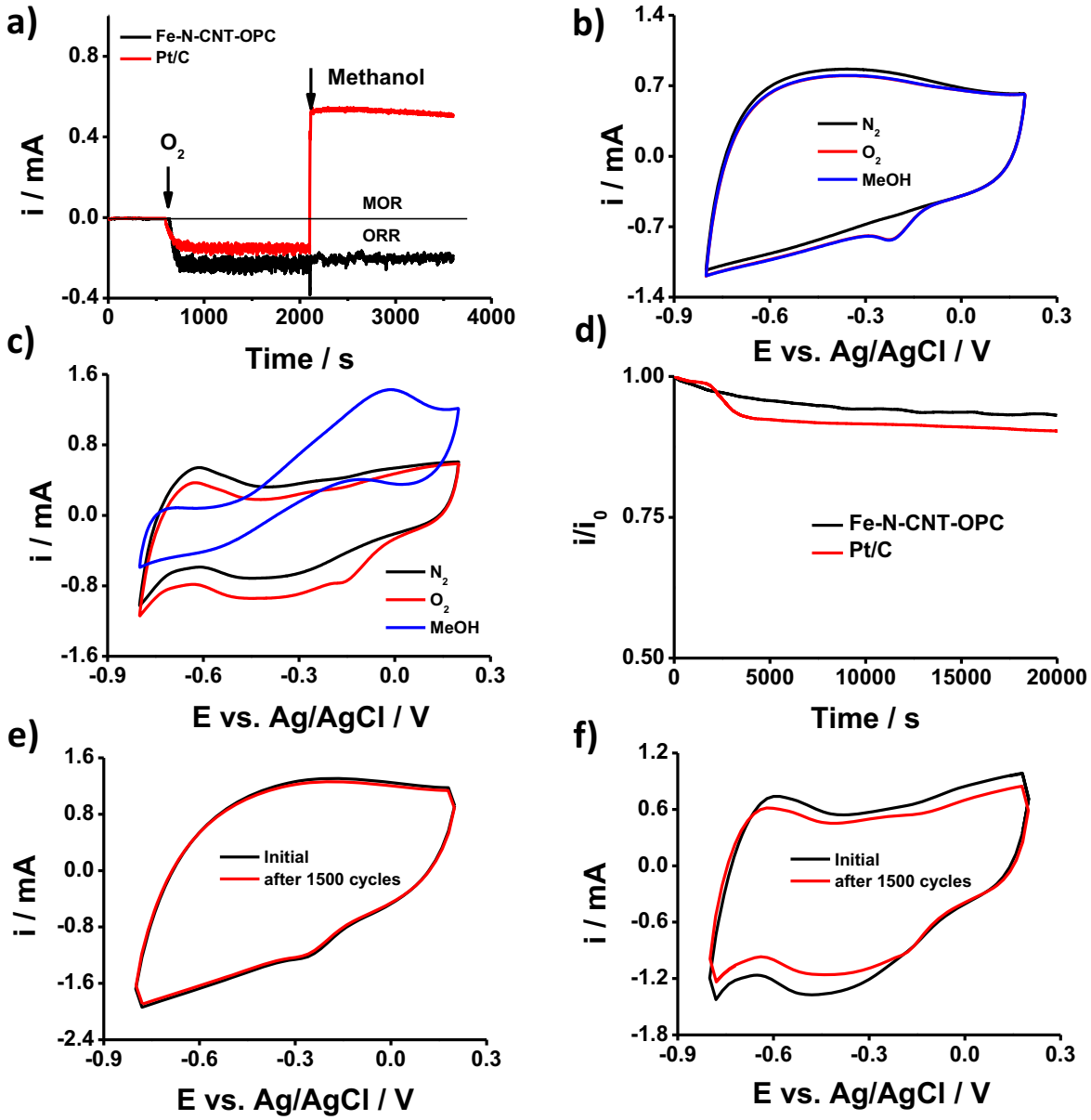

Figure S14. (a) Methanol crossover resistance test by chronoamperometry. When methanol was introduced into the testing cell, the catalytic behaviour of Pt/C changed immediately from oxygen reduction reaction (ORR) to methanol oxidation reaction (MOR) while the Fe-N-CNT-OPC was not affected; The methanol crossover resistance tests were also conducted by CV on Fe-N-CNT-OPC (b) and Pt/C (c), showing the similar behaviour of methanol crossover effect of as in chronoamperometry. (d) Long-term stability test by chronoamperometry of Fe-N-CNT-OPC in comparison with commercial Pt/C. The long term test was conducted on RDE at 1600 rpm with continuous oxygen purged into the electrolyte. The materials were also tested by CV, showing the better stability of Fe-N-CNT-OPC (e) than Pt/C (f). The Pt/C suffered from obvious activity shrinkage but the performance change on Fe-N-CNT-OPC was negligible.

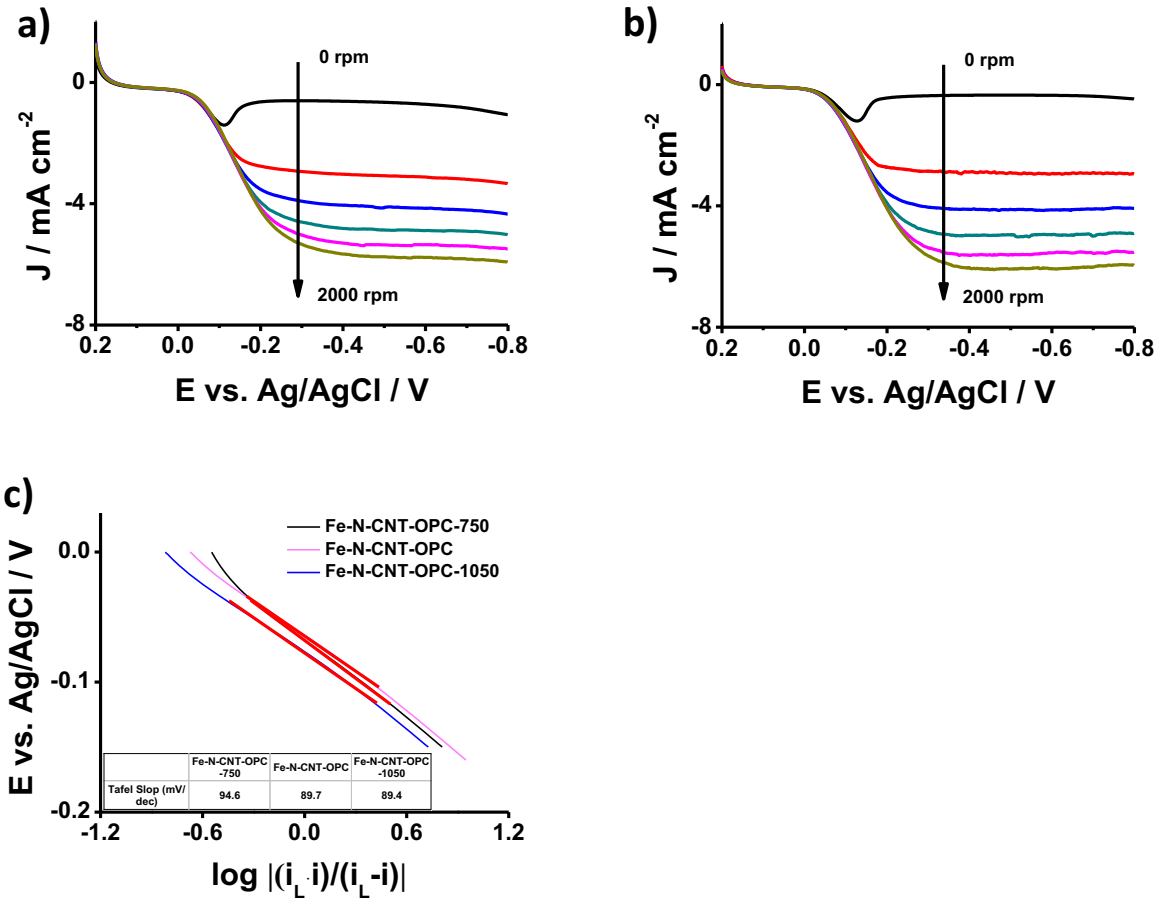

Figure S15. RDE voltammograms of (a) Fe-N-CNT-OPC-750 and (b) Fe-N-CNT-OPC-1050 at different rotating speeds from 0 to 2000 rpm with an increment of 400 rpm between each voltammogram; and the corresponding Tafel plots (c) obtained from the voltammogram at 1600 rpm.

The samples heated at different temperatures show close Tafel slope values indicating their similar kinetics during the ORR catalysis process. This is also in agreement with the trend of their performance in relation with the synthesis temperature.

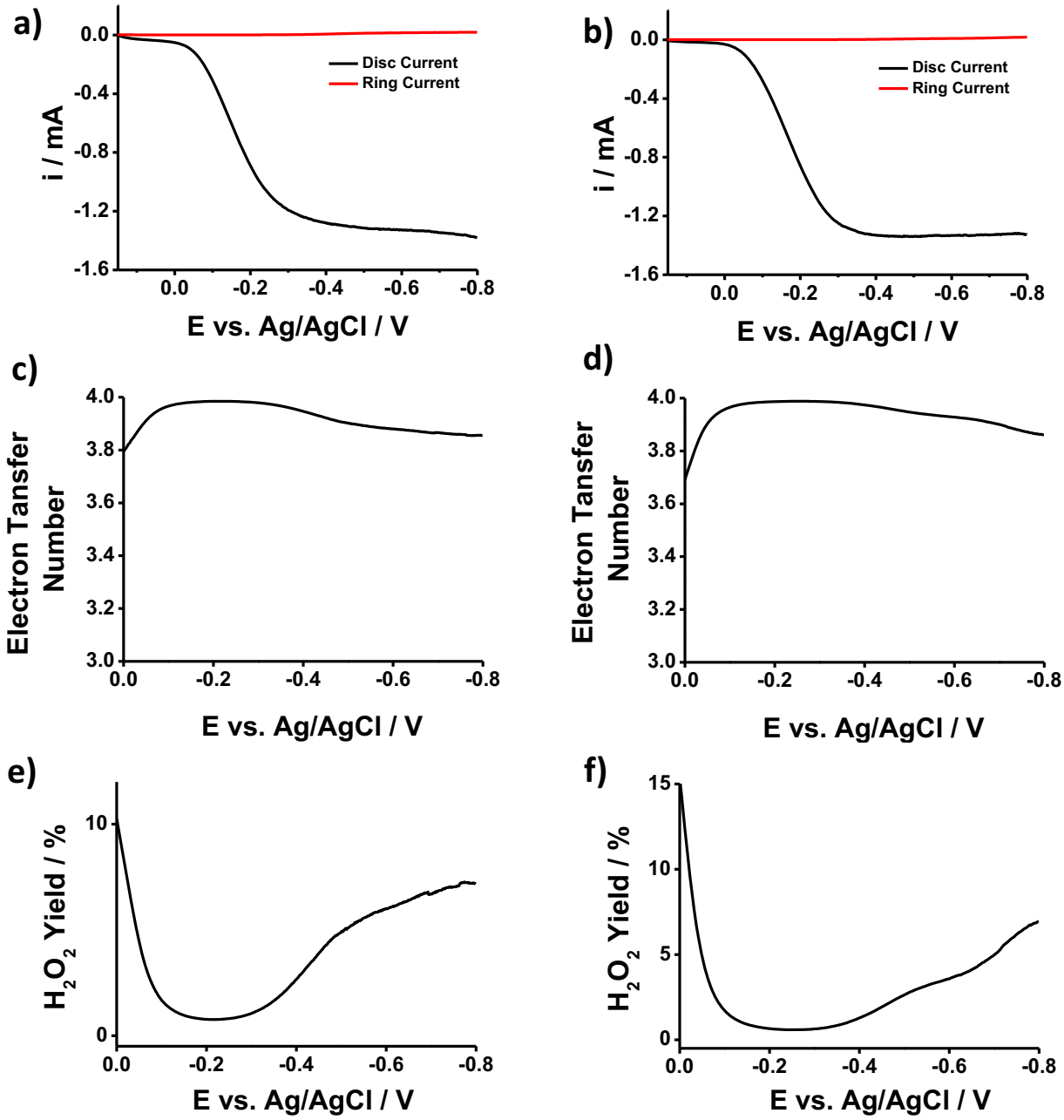

Figure S16. RRDE voltammograms, accordingly calculated electron transfer number and the peroxide yield of Fe-N-CNT-OPC-750 (a, c and e) and Fe-N-CNT-OPC-1050 (b, d and f).

Chapter 5 Design, Optimization and Insights of Non-Noble-Metal decorated Carbon Hybrid for ORR

5.1 Introduction, Significance and Commentary

In the previous chapter, we have presented a carbon based hybrid material, which is composed of porous carbon and graphene and decorated with Fe and N species, for high performance ORR catalysis. We found that Fe-N species can be very helpful in boosting the ORR performance and the in-situ formed highly conductive carbon nanotubes is the key for further enhancing the ORR catalytic performance be increasing the electron conductivity of the material. To further identify the roles of different components in the Fe-N decorated materials, in this section, we have demonstrated a design of Fe-N decorated carbon hybrid of hierarchical porous carbon and in-situ formed graphene. In this design, we are able to control the structure and composition of finial material by simply adjusting the combination of starting materials prior to the final heating step. By constructing an analogue of comparative materials, we have got a clearly view and understanding of the effects of different compositions in the material on it respective ORR activity and as a result we have successfully designed an optimized catalyst with even better performance than the commercial Pt/C of the same quantity.

5.2 Fe-N decorated hybrid porous carbon catalyst for high performance oxygen reduction

This section is included in the thesis as it appears as a research paper composed by **J. Liang**, X. M. Chen, R. F. Zhou, T. Y. Yang and S. Z. Qiao, Designable Fe-N-C Complex: an Avenue towards Best Oxygen Reduction Catalytic Activity, which has been composed for submission and peer review in a paper style.

Statement of Authorship (Page 1)

Statement of Authorship

Title of Paper	Designable Fe-N-C Complex: an Avenue towards Best Oxygen Reduction Catalytic Activity
Publication Status	○ Published, ○ Accepted for Publication, ○ Submitted for Publication, ◉ Publication style
Publication Details	Has been prepared for submission.

Author Contributions

By signing the Statement of Authorship, each author certifies that their stated contribution to the publication is accurate and that permission is granted for the publication to be included in the candidate's thesis.

Name of Principal Author (Candidate)	Ji Liang (First Author)		
Contribution to the Paper	Research plan, material synthesis, most of the characterizations, material performance assessment, manuscript drafting.		
Signature		Date	23/5/2014

Name of Co-Author	Xuemin Chen		
Contribution to the Paper	Assistance with part of key characterization		
Signature		Date	23/5/2014

Name of Co-Author	Ruifeng Zhou		
Contribution to the Paper	Assistance with part of characterization		
Signature		Date	23/5/2014

Name of Co-Author	Tianyu Yang		
Contribution to the Paper	Assistance with part of characterization		
Signature		Date	23/May/2014

Statement of Authorship

Title of Paper	Designable Fe-N-C Complex: an Avenue towards Best Oxygen Reduction Catalytic Activity
Publication Status	○ Published, ○ Accepted for Publication, ○ Submitted for Publication, ◉ Publication style
Publication Details	Has been prepared for submission.

Author Contributions

By signing the Statement of Authorship, each author certifies that their stated contribution to the publication is accurate and that permission is granted for the publication to be included in the candidate's thesis.

Name of Principal Author (Candidate)	Ji Liang (First Author)		
Contribution to the Paper	Research plan, material synthesis, most of the characterizations, material performance assessment, manuscript drafting.		
Signature		Date	23/5/2014

Name of Co-Author	Prof. Shizhang Qiao		
Contribution to the Paper	Design of the project, organisation of the research and supervision Assistance with result discussion and manuscript revising. Corresponding Author		
Signature		Date	23/5/2014

Name of Co-Author			
Contribution to the Paper			
Signature		Date	

Name of Co-Author			
Contribution to the Paper			
Signature		Date	

Designable Fe-N-C Complex: an Avenue towards Best Oxygen Reduction Catalytic Activity

*Ji Liang, Rui Feng Zhou, Xue Min Chen, Tian Yu Yang and Shi Zhang Qiao**

Oxygen reduction reactions (ORR) via electrochemical processes is the key step controlling the overall performance of a number of devices concerning the conversion and storage of clean energy, such as low-temperature fuel cells, metal-air batteries or oxygen sensors.[1, 2] Due to the sluggish nature of ORR, catalysts are inevitably employed to accelerate ORR in these devices and Pt nanoparticles loaded on carbon black (Pt/C) have been the most widely used and successfully commercialized by far. However, multiple disadvantages, especially its high price, have made the Pt/C catalyst economically unfavorable for large scale application, and have thus severely hindered the commercialization of these devices.[3] To deal with this issue, extensive efforts have been made to develop a non-noble metal electrocatalyst with low price but comparable performance as Pt/C, including both metal-free catalysts (e.g. heteroatom doped carbon materials) [3-8] as well as non-noble-metal catalysts (e.g. transitional metal or their compounds decorated carbon materials). [9-13]

Among these Pt-free catalysts, iron-nitrogen-carbon (Fe-N-C) complex is exceptionally attractive because of the potentially high ORR activity from the Fe-N complex, which has been theoretically predicted by the computational calculations. As a result, a variety of such materials with different structures, such as nanotubes,[12] microspheres,[14] tetra-pods [15] or nanosheets,[10] have been fabricated and studied. Although, these materials could show very good ORR performances in some cases; however the roles of the different components in boosting the ORR, which is the key to understand the ORR mechanism and kinetics of these materials, are still unknown. The difficult in fully revealing this can be attributed to multiple aspects. Firstly, in many cases, the microstructure of Fe-N-C materials is strongly controlled by their chemical compositions and the change of their compound always results in the formation of different microstructures. Comparing the ORR catalytic activity based on the different microstructures, which frequently lead to different ORR

kinetics, is not only unfair but also misleading. Besides, for the materials reported by far, the precursors always contain multiple elements (e.g. Fe-N [10], Fe-C [16] or N-C [15]), thus the synthesis of analogues with designed component as comparatives to reveal the function of individual elements and to confirm the synergistic effect of multiple elements is extremely hard. Moreover, in many synthesis, excessive amount of Fe has been remained in the material to form the Fe-N complex as well as to enhance the graphitic structures in the material, which not only forms large amount of inactive large Fe particles but also require tedious acid leaching treatments to remove. As a consequent, these disadvantages and complexity in Fe-N-C materials' design and fabrication, both in their composition and structure, have veiled the ORR process on the catalyst, made it hard to achieve the predicted high ORR performance and severely uplifted the cost of the materials.[12, 15-17]

Recently, we have demonstrated a highly controllable synthesis of hybrid carbon materials based on hierarchical porous carbon and graphene, which potentially provides an ideal platform of fabricating an analogue of Fe-N-C material with optimized microstructure for ORR and designable chemical components. Via a simple precursor adjustment during the synthesis, an analogue of materials of hierarchical porous carbon (HPC), N or/and Fe decorated HPC (N-HPC, Fe-HPC or Fe-N-HPC) were facilely fabricated. By looking into the ORR behavior on them, a comprehensive step-by-step understanding of the ORR mechanism and kinetics of the Fe-N-C materials can thus be obtained and the role of each component can also be revealed. Afterward, by *in-situ* grown graphene on the Fe-N-OPC, to further enhance its ORR performance by increasing the electron conductivity, an optimal-designed material of Fe-N decorated graphene *in-situ* formed on hierarchical ordered porous carbon (denoted as Fe-N-G-HPC) has been successfully obtained with a even better ORR catalytic performance than Pt/C of the same amount.

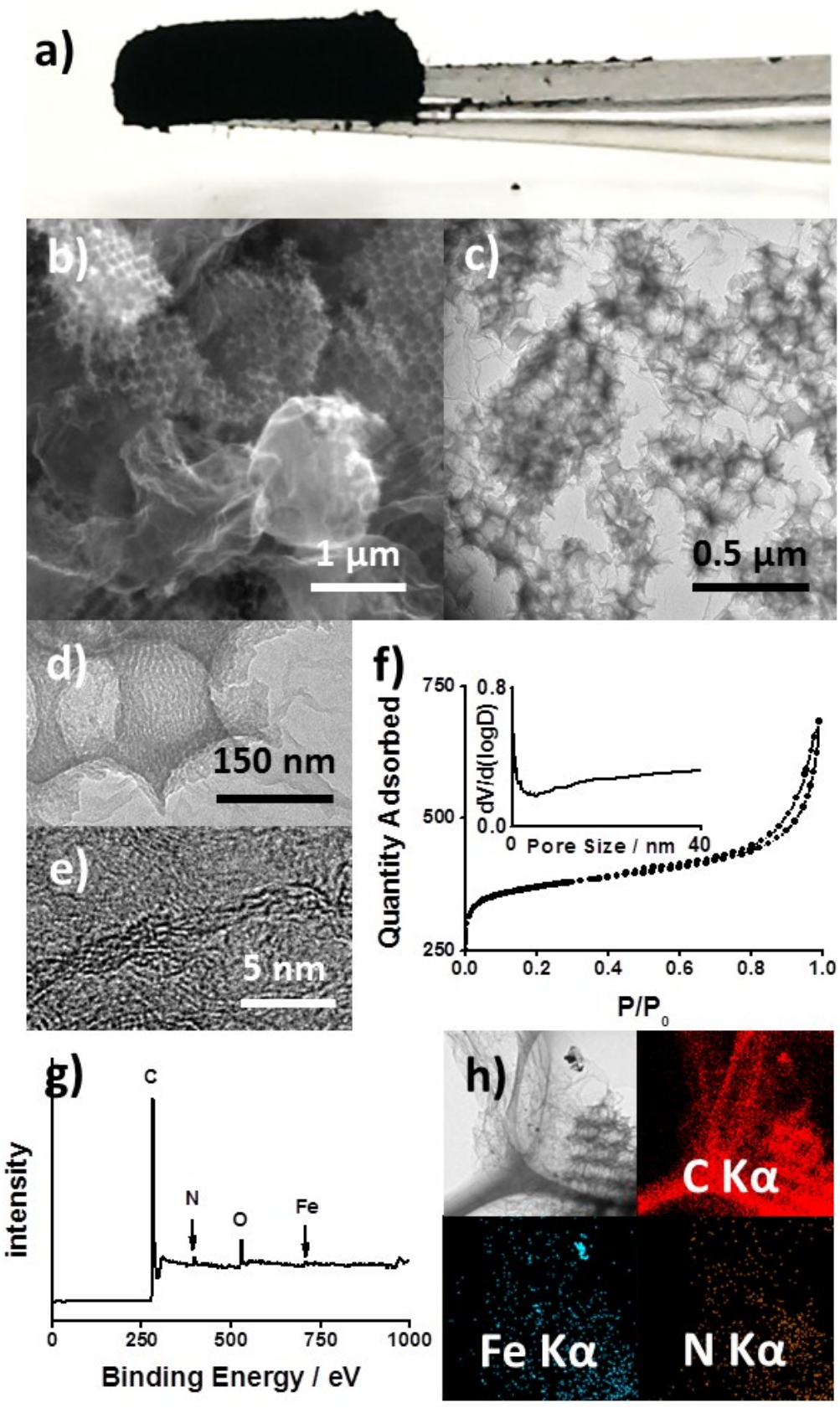

Figure 1. Typical Characterizations of Fe-N-G-HPC material heated at 900 °C. (a), Optical image of the sample after the pyrolysis held on a tweezer. (b), SEM and (c-e) TEM images of different sections of the sample. (f), Nitrogen adsorption and desorption isotherms and the corresponding pore distribution (inset). (g), XPS survey scan and h) elemental mapping by EDS.

Typically, the Fe-N-G-HPC material shows a monolithic appearance (Figure 1a), rather than the porous carbon in loose powder form without the *in-situ* formed graphene, which indicats a 3-dimensional connection among the HPC microblocks. This connection has been further confirmed by the scanning electron microscopy (SEM) and transmission electron microscopy (TEM) images (Figure 1b, c and S1), to come from the foam-like wrinkled graphene where the HPC microblocks are embedded. High resolution (HR) TEM images (Figure 1d) indicated the existence of tubular mesopores on the walls of the macropores, which is the typical pore structure derived from the F127 soft template. The graphene section was also observed under HR-TEM as shown in Figure 1e and S2, which reveals the graphene is composed of abundant small-sized graphitic domains. Besides, the wrinkled section on the graphene also suggests the thickness of *ca.* 2.5 nm to 4 nm, which corresponds to 3-6 single graphitic layers in the graphene. Besides, metal particles with diameter of tens of nanometers were also occasionally observed, on both the HPC and graphene sections (Figure S3), which might result from the relocation and aggregation of small metal species at high temperature and can be proved by featureless XRD pattern of the sample heated at lower temperature of 750 °C (Figure S4). The XRD patterns of the materials also reveal the existence of different metallic Fe phases as well as Fe_3O_4 in this material.

The porosity of the samples was then examined by nitrogen adsorption-desorption (Figure 1f). Both the Fe-N-G-HPC and Fe-N-HPC materials possess an isotherm with a hysteresis loop at extending from medium to high pressure regions, which is typical of hierarchical porous carbons due to the capillary condensation in the tubular mesopores and the neck section of the cage-like macropores.

The chemistry of Fe-N-G-HPC and Fe-N-HPC was then analyzed by X-ray photoelectron spectroscopy (XPS), which confirms the existence of similar amount of N and Fe species on the carbon matrix in both materials (Figure 1g, S6 and Table S1). Besides, small amount of oxygen has also been probed, which could possibly result from the oxygen species in the resin precursor. The distribution of these elements in Fe-N-G-HPC has also been examined via energy dispersive

spectroscopy (EDS) mapping (Figure 1h and S7). Besides the uniformly distributed C elements as expected, Fe and N species are also found to be finely dispersed all over the material on both the porous carbon and graphene sections. The highly dispersive Fe and N elements in the carbon framework may indicate an interaction between them during the high temperature treatment and have also been believed to be active towards ORR. [12, 15-17]

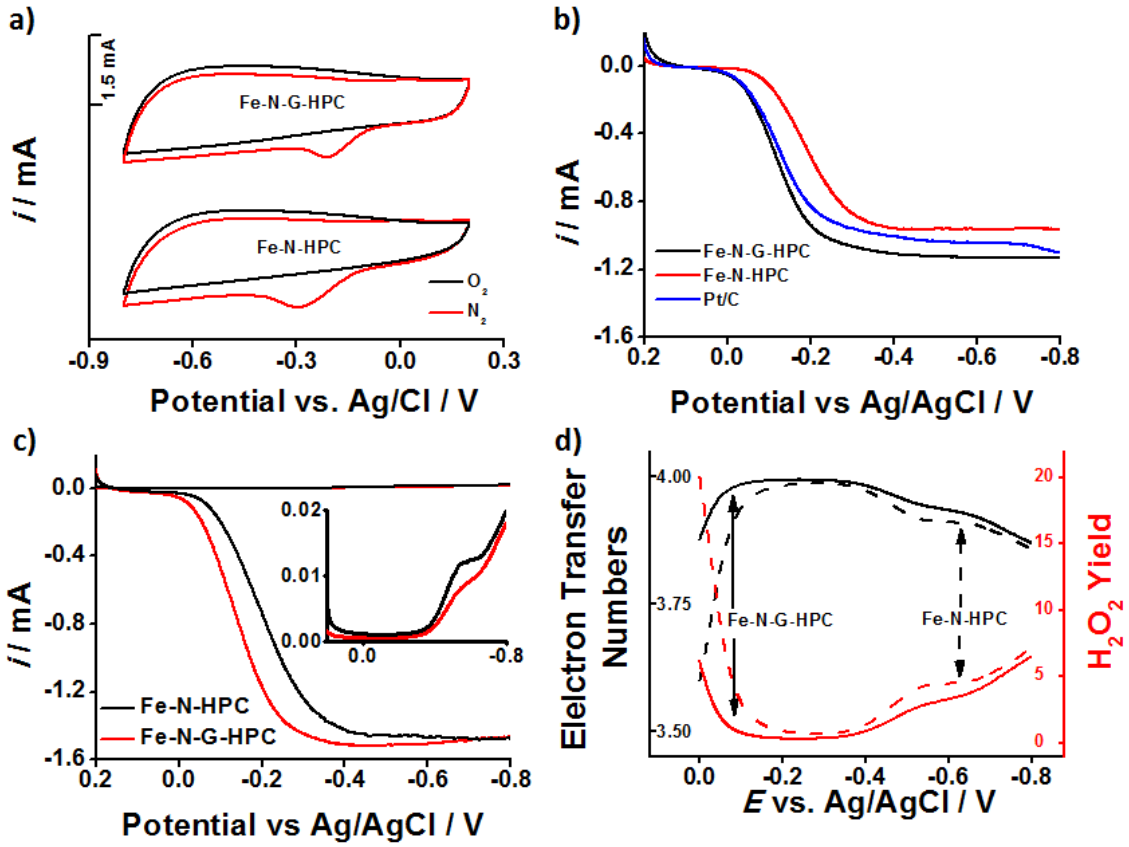

Figure 2. Elelctrochemical catalytic performance for ORR of the Fe-N-G-HPC and Fe-N-HPC samples in comparison with the commercial Pt/C sample. (a) CV loops, (b) voltammograms of the samples on RDE, (c) voltammograms of the samples obtained on RRDE and the ring current (inset), (d) the electron transfer numbers and peroxide product of the samples.

To evaluate the ORR catalytic performance of the materials, the Fe-N-G-HPC and Fe-N-HPC were firstly tested via cyclic voltammetry (CV) as shown in Figure 2a. Both the samples give a distinct ORR response when oxygen is introduced into the electrolyte, suggesting their ability to electrochemically reduce oxygen upon certain potentials. However, compared with the Fe-N-HPC sample, the ORR peak of Fe-N-G-HPC with the *in-situ* grown graphene is more positive in both the onset and peak positions, which indicates oxygen can be more facilely reduced on Fe-N-G-HPC at a

smaller over-potential on this material. To gain deeper insight into the ORR process over the materials, they were then assessed on rotating disk electrode (RDE) in comparison with the commercial 20 wt. % Pt/C catalyst of the same amount as shown in Figure 2b and S9. All the samples reached the diffusion limiting region before -0.3 V with a similar ORR current, which suggests smooth ORR kinetic over the materials. Remarkably, the Fe-N-G-HPC gives a very positive ORR onset potential and half-wave potential, which are even more positive than that of the Pt/C and have rarely been observed on the non-noble-metal catalysts.[12, 15-17] Moreover, the ORR efficiency of the materials has also been quantified using the rotating ring-disk electrode (RRDE) method (Figure 2c). Similar voltammograms have been collected on the disk electrode as in the RDE test. However, although the Fe-N-G-HPC presented a significantly higher ORR activity by giving a much more positive ORR onset potential and a larger ORR current at the low over-potential between 0 to -0.4 V compared with the Fe-N-HPC, the Fe-N-G-HPC still possessed an even lower current on the ring electrode. As a result, the accordingly calculated ORR efficiency of the Fe-N-G-HPC sample is much high higher than the Fe-N-HPC especially at the low over-potential region, which is proved by its larger electron transfer numbers and lower peroxide production (up to 3.99 at -0.1 V and less than 1 % respectively at -0.1 V) (Figure 2d). Thus, the Fe-N-G-HPC material not only possesses an outstanding ORR activity better than the commercial Pt/C, but also undergoes a high efficiency completely 4 electron ORR pathway during the catalysis.

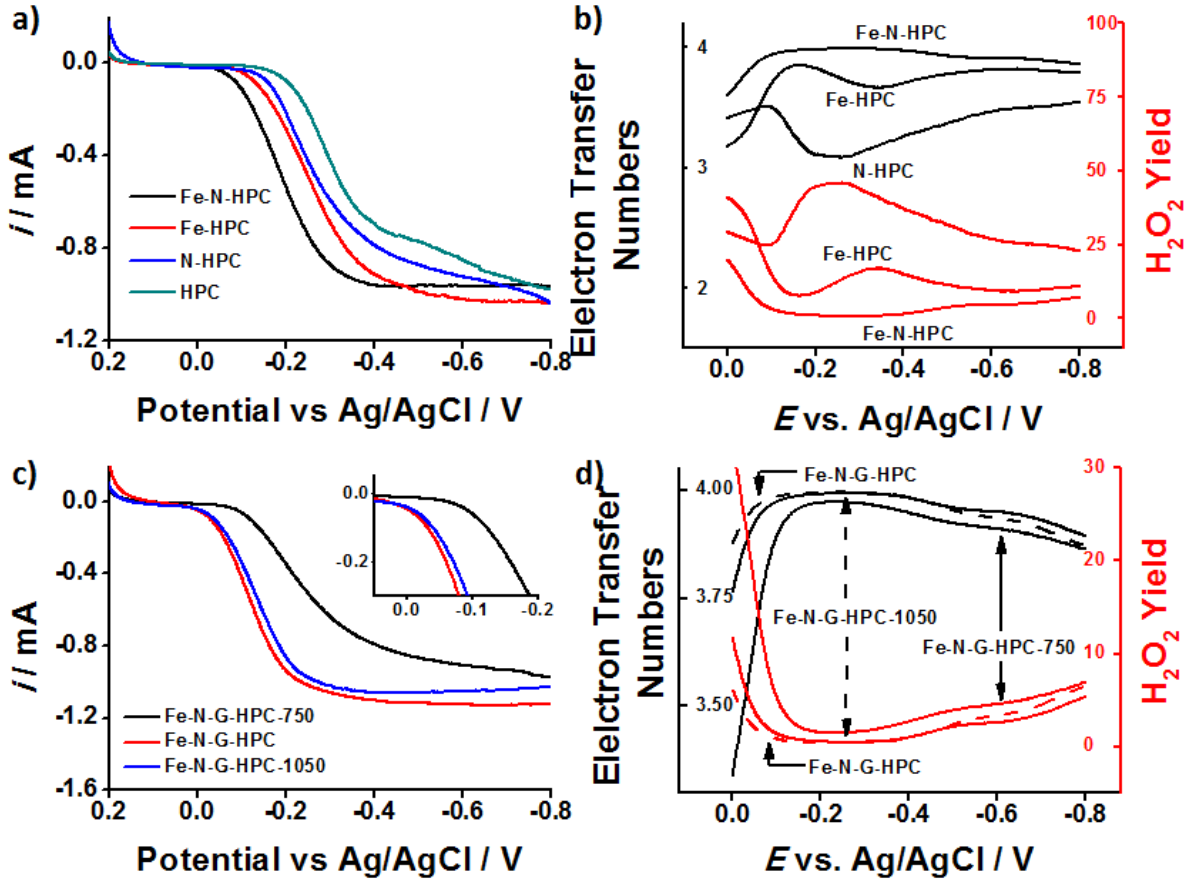

Figure 3. Elelctrochemical catalytic performance for ORR of the analogue samples (a) voltammograms of the samples containing different elements obtained on RDE, (b) the corresponding electron transfer numbers and peroxide product of the samples, (c) voltammograms of the samples prepared at different temperatures obtained on RDE and the enlarged low-potential section (inset), (d) the corresponding electron transfer numbers and peroxide product of the samples.

To obtain an insight into the roles that the decorated Fe and/or N elements plays in the catalyst as well as to explorer the synergistic effect between these two species on the catalyst, we have also constructed materials of either Fe or N decorated HPC as well as the pristine HPC (denoted as Fe-HPC, N-HPC and HPC respectively). Their ORR performances were firstly evaluated by CV and RDE techniques in comparison with the Fe-N-HPC sample (Figure 3a, S9 and S10). From the RDE voltammograms, all the samples give comparable ORR currents at high over- potential at -0.8 V, reaching their diffusion limiting current which is mainly determined by the geometry and rotating speed of the electrode. However, the sample dually decorated by both Fe and N gives a remarkably

better ORR catalytic performance considering its obviously more positive ORR onset potential and sharper current increase as the potential goes more negative compared with the other samples decorated by sole or non heterospecies. Moreover, the voltammogram of Fe-N-HPC material quickly reached its diffusion limited current plateau (*ca.* -0.4 to -0.8 V) after the ORR kinetic limited region (*ca*. 0 to -0.4 V), which indicates that this material possesses more stable electron transfer numbers during the ORR process. In contrast, the comparative materials underwent a constantly increasing ORR current without obvious flat current plateaus at the same potential region, which reveals a constantly increasing ORR electron transfer number similar as other solely doped/decorated ORR catalysts reported previously.[4-7] And this is further confirmed by the corresponding electron transfer numbers and the peroxide production of the materials during ORR were then collected on the RRDE as shown in Figure 3b and S11. From these observations, it is reasonable to deduce that Fe and N species dually decorated in the carbon material can significantly boost higher catalytic activity as well as enhance the ORR efficiency from 2 electron pathway to 4 electron pathway, especially at low over-potential regions.

The origin of the synergistic effect between the Fe and N elements in the carbon, which has been proved to be crucial in enhancing the ORR catalytic activity, can also be evidenced by the high resolution N1s spectra in the XPS results of Fe-N-HPC and N-HPC. In the Fe-N-HPC sample containing both Fe and N, the corresponding N1s spectra contains larger amount of graphitic nitrogen species in the carbon frame work, which is similar as the Fe-N-G-HPC, compared with the N-HPC with large amount of pyridinic nitrogen. The larger amount of saturated graphitic nitrogen atoms with triple bonds with the neighboring atoms are not only considered more active towards ORR, but moreover, can be an evidence of the binding with the surrounding Fe atoms in the carbon, which is in agreement with the EDS elemental mappings of the finely dispersed Fe and N species on carbon.

Pyrolysis temperature during the materials synthesis is another parameter that can affect the materials' catalytic behavior by determining its chemical composition as well as the microstructure. Thus, Fe and N decorated hybrid carbon materials fabricated at different 750 °C and 1050 °C

(denoted as Fe-N-G-HPC-750 and Fe-N-G-HPC-1050) were also tested on RDE and RRDE (Figure 3c, d and S12) in comparison with the Fe-N-G-HPC which is heated at 900 °C. It is interesting to note that the sample prepared at 900 °C shows the best ORR catalytic performance, which is slightly better than the one heated at 1050 °C, by giving the most positive ORR onset potential and the current (Figure 3c). In sharp contrast, the sample synthesized at 750 °C only gives a poor ORR activity with an onset potential over 100 mV more negative. On the other hand, although all the samples can eventually reach high ORR efficiency by showing a high electron transfer number and low peroxide production when the potential is negative enough (e.g. over -0.2 V for the Fe-N-G-HPC sample); however, at low over-potential between 0 to -0.05 V, the samples prepared at higher temperature shows an substantially higher ORR efficiency (Figure 3d). Thus, treating the material with high temperature can remarkably uplift the materials' performance at low over-potential region, which is the key factor when evaluating the activity of an ORR catalyst.

The material's best performance, when synthesized at 900 °C, can be a combined result of both the compositional and structural aspects. Compared with the Fe-N-G-HPC-750, the samples heated at 900 °C and 1050 °C possessed a larger surface area mainly attributed by the mesopores (Figure S13). The larger surface area would help expose more active sites on the Fe-N-G-HPC and Fe-N-G-HPC-1050 samples, whilst the much smaller surface area on the Fe-N-G-HPC-750 sample may come from the pore blockage by the residual carbon nitride in the material. The materials' chemical composition was then analyzed by XPS (Figure S14). The Fe-N-G-HPC-750 possesses the highest content of Fe and N (0.38 and 11.92 at.% respectively), which is much larger than that of Fe-N-G-HPC (0.15 and 2.40 at.% respectively) and Fe-N-G-HPC-1050 (0.09 and 1.68 at.% respectively); and the proportion of pyrodinic nitrogen decreases while the heating temperature rises from 750 °C to 1050 °C (Figure S15 and Table S2). As a result, the poor performance on the Fe-N-G-HPC-750 could be due to low surface area, although it has the largest amount of N species in the material. On the other hand, the samples heated at 900 °C and 1050 °C have similarly large surface area and high content of active N species.[18] The slightly better performance on the Fe-N-G-HPC sample, heated at 900 °C, would then be attributed to the inconsiderably larger

amount of the Fe and N species in the material.

To sum up, in this research, we have developed a strategy to fabricate an analogue of materials with controllable chemical composition and microstructure. By studying their ORR performances in relation with their composition, the roles of different species in this material have been understood. As a result, a carbon based catalyst, which contains both Fe and N as well as in-situ grown graphene, has been designed and constructed with an ultrahigh ORR activity even better than that of commercial Pt/C catalyst of the same quantity, making this material a very suitable substitute for the expensive Pt catalysts for ORR. Moreover, his material is made from very cheap chemicals through one-step heating procedure, which makes it practically ready for large-scale production.

References:

[1] B. C. H. Steele, A. Heinzel, *Nature* **2001**, *414*, 345.

[2] A. Débart, A. J. Paterson, J. Bao, P. G. Bruce, *Angew. Chem. Int. Ed.* **2008**, *47*, 4521.

[3] K. Gong, F. Du, Z. Xia, M. Durstock, L. Dai, *Science* **2009**, *323*, 760.

[4] S. Wang, L. Zhang, Z. Xia, A. Roy, D. W. Chang, J. B. Baek, L. Dai, *Angew. Chem. Int. Ed.* **2012**, *51*, 4209.

[5] P. Chen, T. Y. Xiao, Y. H. Qian, S. S. Li, S. H. Yu, *Adv. Mater.* **2013**, *25*, 3192.

[6] J. Liang, Y. Jiao, M. Jaroniec, S. Z. Qiao, *Angew. Chem. Int. Ed.* **2012**, *51*, 11496.

[7] I. Y. Jeon, S. Zhang, L. Zhang, H. J. Choi, J. M. Seo, Z. Xia, L. Dai, J. B. Baek, *Adv. Mater.* **2013**, *25*, 6138.

[8] J. Liang, Y. Zheng, J. Chen, J. Liu, D. Hulicova-Jurcakova, M. Jaroniec, S. Z. Qiao, *Angew. Chem. Int. Ed.* **2012**, *51*, 3892.

[9] Z. S. Wu, S. Yang, Y. Sun, K. Parvez, X. Feng, K. Mullen, *J. Am. Chem. Soc.* **2012**, *134*, 9082.

[10] Z. Xiang, Y. Xue, D. Cao, L. Huang, J. Chen, L. Dai, *Angew. Chem. Int. Ed.***2014**, *53*, 2433.

[11] H. W. Liang, W. Wei, Z. S. Wu, X. Feng, K. Mullen, *J. Am. Chem. Soc.* **2013**, *135*, 16002.

[12] H. T. Chung, J. H. Won, P. Zelenay, *Nat. Commun.* **2013**, *4*, 1922.

[13] G. Zhang, B. Y. Xia, X. Wang, X. W. Lou, *Adv. Mater.* **2013**, *26*, 2408.

[14] Z. Wen, S. Ci, F. Zhang, X. Feng, S. Cui, S. Mao, S. Luo, Z. He, J. Chen, *Adv. Mater.* **2014**, *24*, 1399.

[15] J. S. Lee, G. S. Park, S. T. Kim, M. Liu, J. Cho, *Angew. Chem. Int. Edit.* **2012**, *52*, 1026.

[16] Y. Hu, J. O. Jensen, W. Zhang, L. N. Cleemann, W. Xing, N. J. Bjerrum, Q. Li, *Angew. Chem. Int. Ed.* **2014**, *53*, 3675.

[17] D. Deng, L. Yu, X. Chen, G. Wang, L. Jin, X. Pan, J. Deng, G. Sun, X. Bao, *Angew. Chem. Int. Ed.* **2013**, *52*, 371.

[18] S. B. Yang, X. L. Feng, X. C. Wang, K. Mullen, *Angew. Chem. Int. Ed.* **2011**, *50*, 5339.

5.3 Supplimentary Ingormation

This section is included in the thesis as as a supplimentary information to setion 5.2. It includes additional information which is not put in the main text of the papr, but as an sullimentrary information submitted together with the paper for peer review.

I. Experimental Section

1. Chemicals

Potassium persulfate ($K_2S_2O_8$, 99 wt. %), melamine (99 wt. %), styrene (ST, 99 %), polyvinyl pyrrolidone (PVP, MW 44000, 99 %), hydroxide pellets (NaOH, 99 %), ethanol (EtOH, absolute), phenol (99 %), formaldehyde solution (37 %), iron(II) chloride tetrahydrate ($FeCl_2 \cdot 4H_2O$, 98 %), iron(III) chloride hexahydrate ($FeCl_3 \cdot 6H_2O$, 97 %), cyclohexane (99.5 %), acetone (> 99 %), acetylacetone (acac, 99 %) were purchased from Sigma-Aldrich and directly used without further treatment or purification.

2. Preparation of polystyrene (PS) spheres

13 ml ST was firstly washed with 4 ml 10 wt. % NaOH aqueous solution for three times and then deionized (DI) water for two times to remove the stabilizer. During this process, the ST changed from color-less into light yellow, indicating the complete removal of the stabilizer. Then, ST was added to 100 ml DI water containing 0.5 g PVP in a triple-neck flask. The mixture was fluxed and stirred at 70 °C/600 rpm for 30 min with continuous N_2 purged in. Then, 20 ml aqueous solution containing 0.3 g $K_2S_2O_8$ was injected into the flask to initiate the polymerization of ST forming PS spheres. The mixture was kept flux-stirred at 70 °C/600 rpm for 24 h. The milky product was then centrifuged and washed with EtOH for three times. Finally, the PS microspheres were dispersed in EtOH by ultrasonication and the suspension was dried in an evaporation dish at room temperature, resulting in a colorful 3D packed PS template of about 10 g.

3. Preparation of resol

Typically, 10 g of phenol was heated until melt at 42 °C in a capped bottle. Then 2.1 g of 20 % NaOH aqueous solution was added by drop with continuous stir at 100 rpm. Afterward, 17.7 g of 37

wt. % formaldehyde solution was added by drop and the heating temperature was raised to 70 °C. The solution was heated and stirred for another 1 h, and then cooled to room temperature. After that, the pH of the solution was adjusted with 2 M HCl aqueous solution until 7. Then, water was removed by rotary evaporation at 45 °C and the product was diluted into a 20 wt. % EtOH solution. During the dilution, the separated NaCl was filtered, resulting in a pale yellow solution. The prepared resol solution can be stored in fridge for several months.

4. Preparations of Fe contained porous resin (Fe-resin)

1.7 g F127 was dissolved in 17 ml EtOH at 50 °C with continuous stir for 30 min. Then 8.5 g of above prepared 20 wt. % resol solution was added and kept stirred for another 20 min. Then, 0.12 g $FeCl_3 \cdot 6H_2O$ and 0.09 g $FeCl_2 \cdot 4H_2O$, which were dissolved in 16 ml EtOH, were added into the solution of Resol and F127. A dark blue color immediately appeared when the two solutions were mixed together. Then 352 μl acetylacetone was added into the solution with stir, and the color changed from dark blue into reddish brown after stirring for several seconds. The above solution was added by drop into the evaporation dish with 10 g of dry PS template. After all the solution was added, the dish was kept under vacuum until no bubble came out from the PS template. This takes about 10 min. Then, the mixture was dried in air at room temperature overnight to form Fe/PS/Resl/F127 precursor. After that, the material was heated at 100 °C for 24 h in air and then at 350 °C in N_2 for 3.5 h with a ramp rate of 1 °C min^{-1}, and after this, the color changed from reddish-brown into dark blue. The obtained solid was slightly crashed and washed in excessive amount of acetone and cyclohexane mixture at 60 °C twice under continuous stir to remove the residual template. The washing solvent could be recycled and reused by distillation to remove the dissolved components from the porous resin. The powder was filtered and dried at 100 °C overnight, resulting a porous Fe-contained resin (denoted as the Fe-OPR in the text); and a beautiful color of green-indigo from reversed opal structure containing Fe can be observed.

5. Preparations of Fe-N-G-HPC and Fe-N-HPC

To prepare the Fe-N-G-HPC, the Fe-resin powder was finely ground with 5 times weight of melamine and 5 times weight of g-C_3N_4 (prepared by heating melamine in air at 550 °C for 4 h) in an agate mortar and the mixture was heated in the following program in N_2 to prepare Fe-N-G-HPC: Room temperature → 60 °C (ramp rate: 1 °C min^{-1}, kept for 3 h) → 600 °C (ramp rate: 2.3 °C min^{-1}, kept for 4 h) → 900 °C (ramp rate: 5 °C min^{-1}, kept for 3 h) → room temperature.

Fe-N-G-HPC-750 and Fe-N-G-HPC-1050 were also synthesized similarly as above but by changing the heating temperature from 900 °C to 750 °C and 1050 °C, respectively.

To prepare Fe-N-HPC without in-situ formed graphene, same amount of melamine and g-C_3N_4 was put in a separate boat with cover. Then the materials underwent the same heating process as above.

6**. Preparations of Fe-HPC, N-HPC and HPC**

To prepare the Fe-HPC, Fe-resin was heated without any melamine or g-C_3N_4 through the heating pregram as used for the Fe-N-G-HPC.

To prepare the N-HPC and HPC, pristine resin was prepared same as Fe-resin, but without putting any iron salts into the resol/F127 solution.

To prepare N-HPC without in-situ formed graphene, resin was put in a boat and then 5 times weight of melamine and 5 times weight of g-C_3N_4 was put in a separate boat with cover. Then the materials underwent the same heating process as used for Fe-N-G-HPC.

To prepare HPC, pristine resin was heated without any melamine or g-C_3N_4 through the heating pregram as used for the Fe-N-G-HPC

7. Characterizations

Nitrogen adsorption-desorption isotherm was recorded on Tristar II (Micrometrics) at -196 °C. Pore size distribution was calculated by Barrett-Joyner-Halenda (BJH) model using adsorption branch data of the nitrogen isotherms. The specific surface area was calculated using adsorption data at the relative pressure range of P/P_0 = 0.05-0.3 by Brunauer-Emmett-Teller (BET) model.

Microstructures of the samples were observed on TEM (Tecnai G2 Spirit TEM) and SEM

(Quanta FEG 450, FEI). High resolution TEM images were obtained on JEM-2100 microscopy. Elemental mapping was conducted using EDAX detector attached on JEM-2100. XPS analysis was carried out on AXIS Ultra spectrometer (Kratos Analytical Ltd.) with monochromated Al Kα radiation at a pressure of *ca.* 5×10^{-9} Pa. Binding energies were calibrated using the adventitious carbon (C1s) = 284.5 eV

All Raman spectra were collected on LabRAM (Horiba Ltd) with 514.3 nm Ar laser.

X-Ray diffraction was performed on Miniflx-600 (Rigaku Ltd.) at ambient conditions using a Cu Kα X-ray.

8. Electrochemical test

For the electrochemical test, 2 mg of the catalyst was dispersed in 1 ml of deionized water (18.2 MΩ). The mixture was slightly ultrasonicated to obtain a homogenous catalyst ink.

To prepare the working electrode for electrochemical measurements, 40 µl of the ink was dipped on a mirror polished glass carbon electrode. Then, 10 µl of 0.5 wt. % Nafion aqueous solution was dipped on the electrode and dried at room temperature as binder. After that, the working electrode was inserted into the cell setup, which is composed of a platinum counter electrode, an Ag/AgCl/KCl (3 M) reference electrode and a glass cell containing 100 ml of 0.1 M KOH aqueous electrolyte.

Cyclic voltammetry (CV) experiments were performed on an electrochemical analysis station (CHI 760 C, CH Instruments, USA) at 100 mV s^{-1}. Before test, an O_2/N_2 flow was used to purge through the electrolyte in the cell for 20 min to saturate it with O_2/N_2.

For the rotating disk electrode (RDE) and rotating ring-disc electrode (RRDE) test, the same working electrode was prepared as for CV and the test was conducted on CHI 760 C. A Pt wire and an Ag/AgCl/KCl (3 M) were used as the counter and reference electrodes, respectively. The linear sweep voltammograms of the modified glass carbon electrode were recorded in O_2 saturated 0.1 M KOH with a scan rate of 5 mV s^{-1} at various rotating speeds from 0 to 2000 rpm for ORR. After

each scan, the electrolyte was saturated with O_2 again for 5 minutes. The sample was tested 3 times to avoid any incidental error.

For the rotating diska-ring electrode (RRDE) test, the working electrode was prepared as illustrated above and the test was conducted on CHI 760 C. A Pt wire and an Ag/AgCl/KCl (3 M) were used as the counter and reference electrodes, respectively. The linear sweep voltammograms were recorded in O_2 saturated 0.1 M KOH at 1600 rpm. The disc was set to scan at 5 mV s^{-1} on the disc electrode from 0.2 V to -0.8 V *vs.* Ag/AgCl and the ring was set at 0.5 V *vs.* Ag/AgCl. The collecting efficiency of the RRDE (N) was 0.37.

The perocide yield (HO_2^-%) and the electron transfer number (n) was calculated as follows:

$$HO_2^-\% = 200 \times I_r / N / (I_d + I_r / N)$$

$$n = 4 \times I_d / (I_d + I_r / N)$$

where I_d is the disc current and I_r is the ring current.

II Supplementary Results

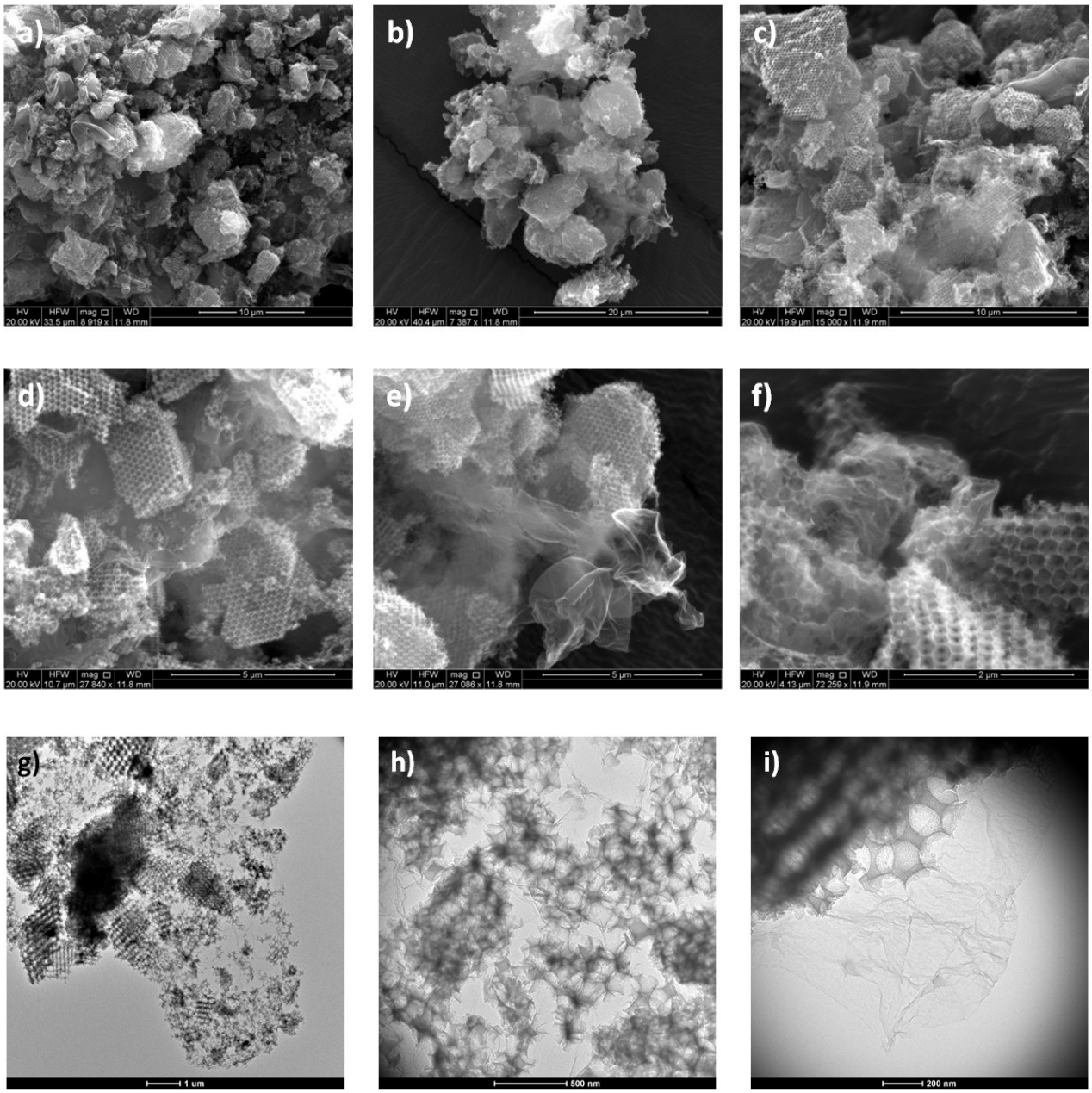

Figure S1. (a-f) SEM and (g-i) TEM images of Fe-N-G-HPC at different magnifications.

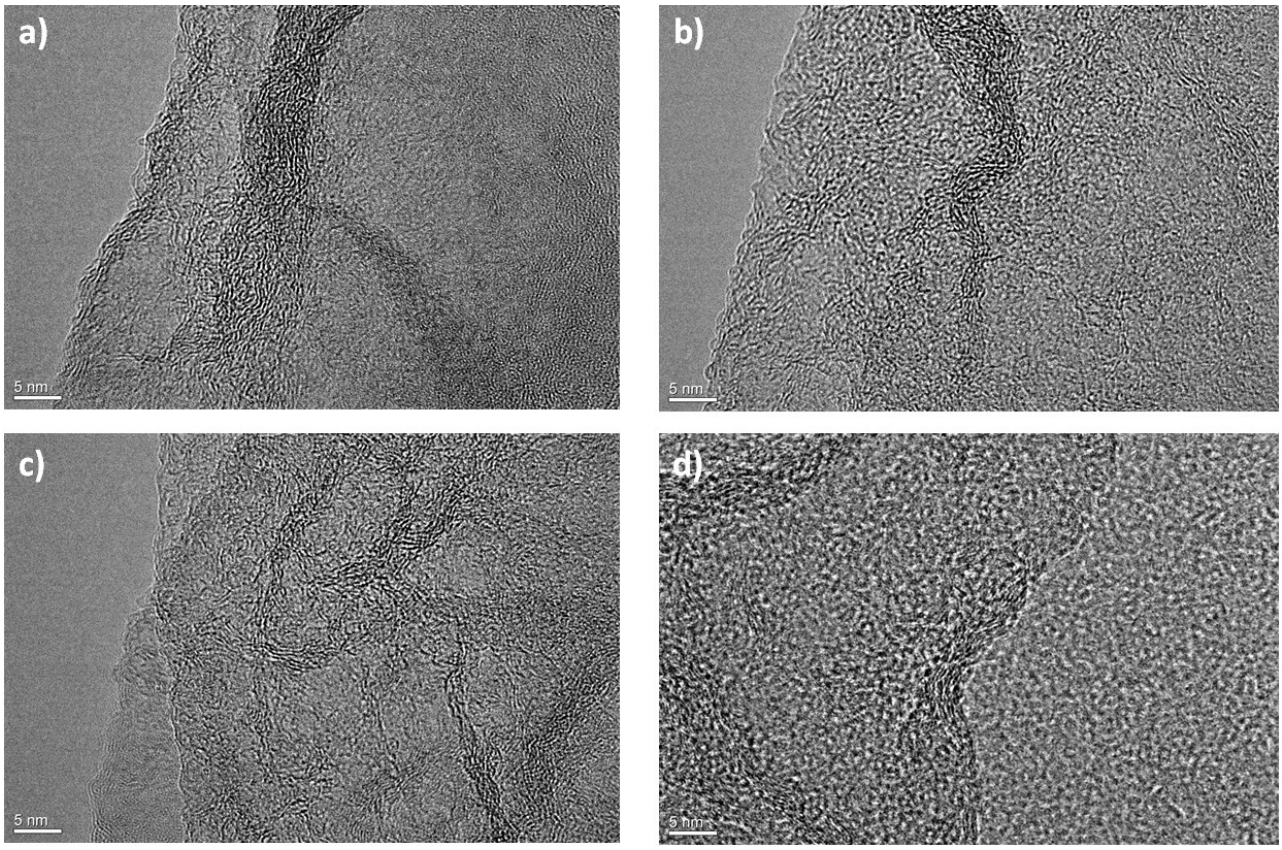

Figure S2. High resolution TEM images of the graphene section in the Fe-N-G-HPC material.

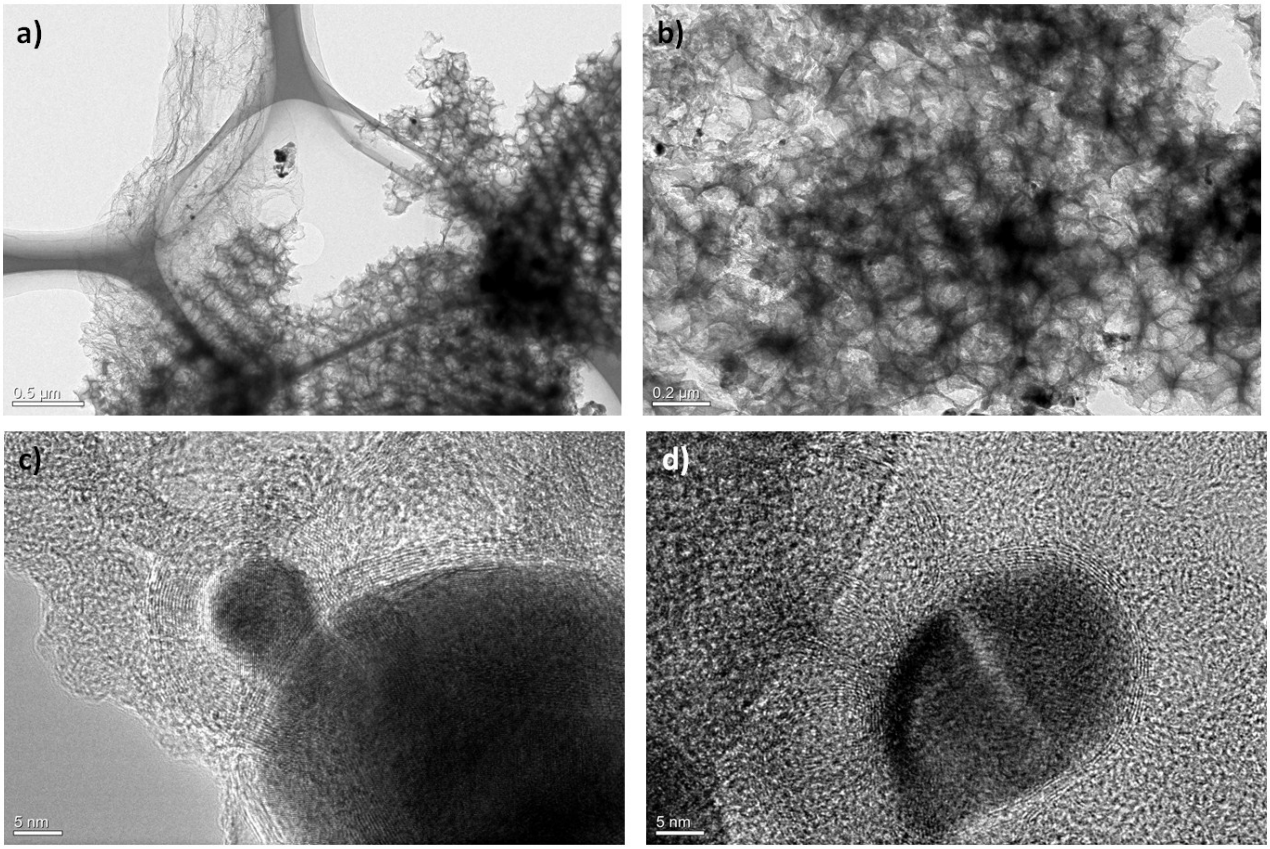

Figure S3. TEM images showing the iron (oxide) nano particles on theFe-N-G-HPC sample.

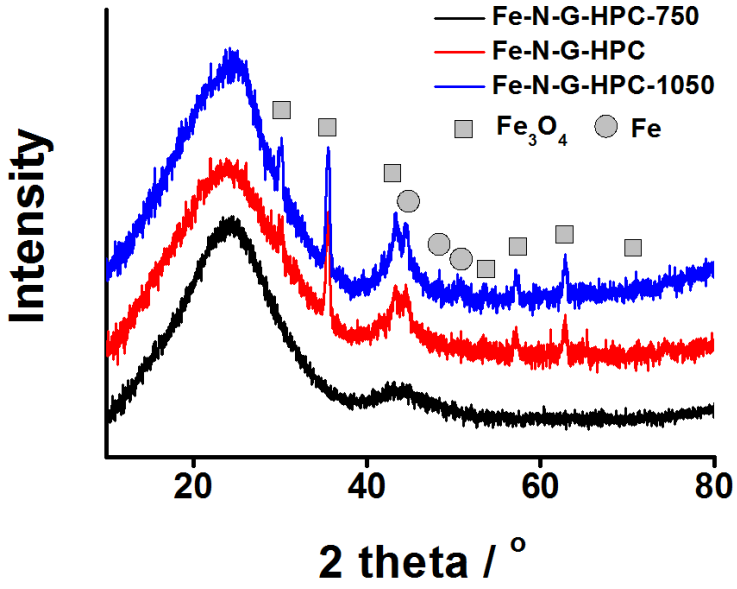

Figure S4. XRD patterns of the Fe-N-G-HPC sample as well as the analogue heated at 750 °C and 1050 °C.

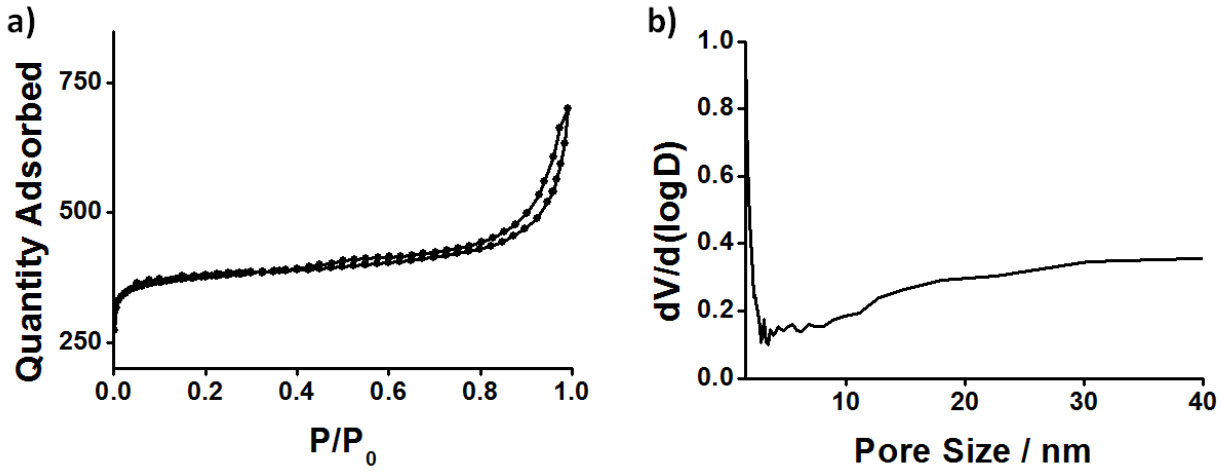

Figure S5. (a) Nitrogen adsorption-desorption isotherms of Fe-N-HPC and (b) the corresponding pore size distribution.

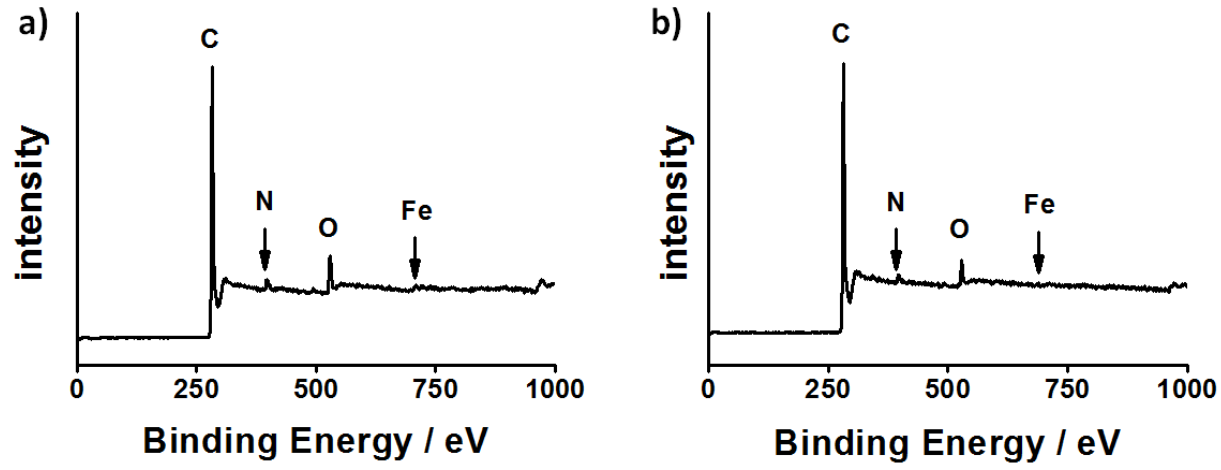

Figure S6. XPS survey scans of (a) Fe-N-G-HPC and (b) Fe-N-HPC.

Table S1

Content (at.%)	Fe	N	O	C
Fe-N-HPC	0.14	2.11	3.29	94.46
Fe-N-G-HPC	0.15	2.40	5.43	92.01

Table S1. The content of different elements in the Fe-N-G-HPC and Fe-N-HPC samples obtained from the XPS results in Figure S6.

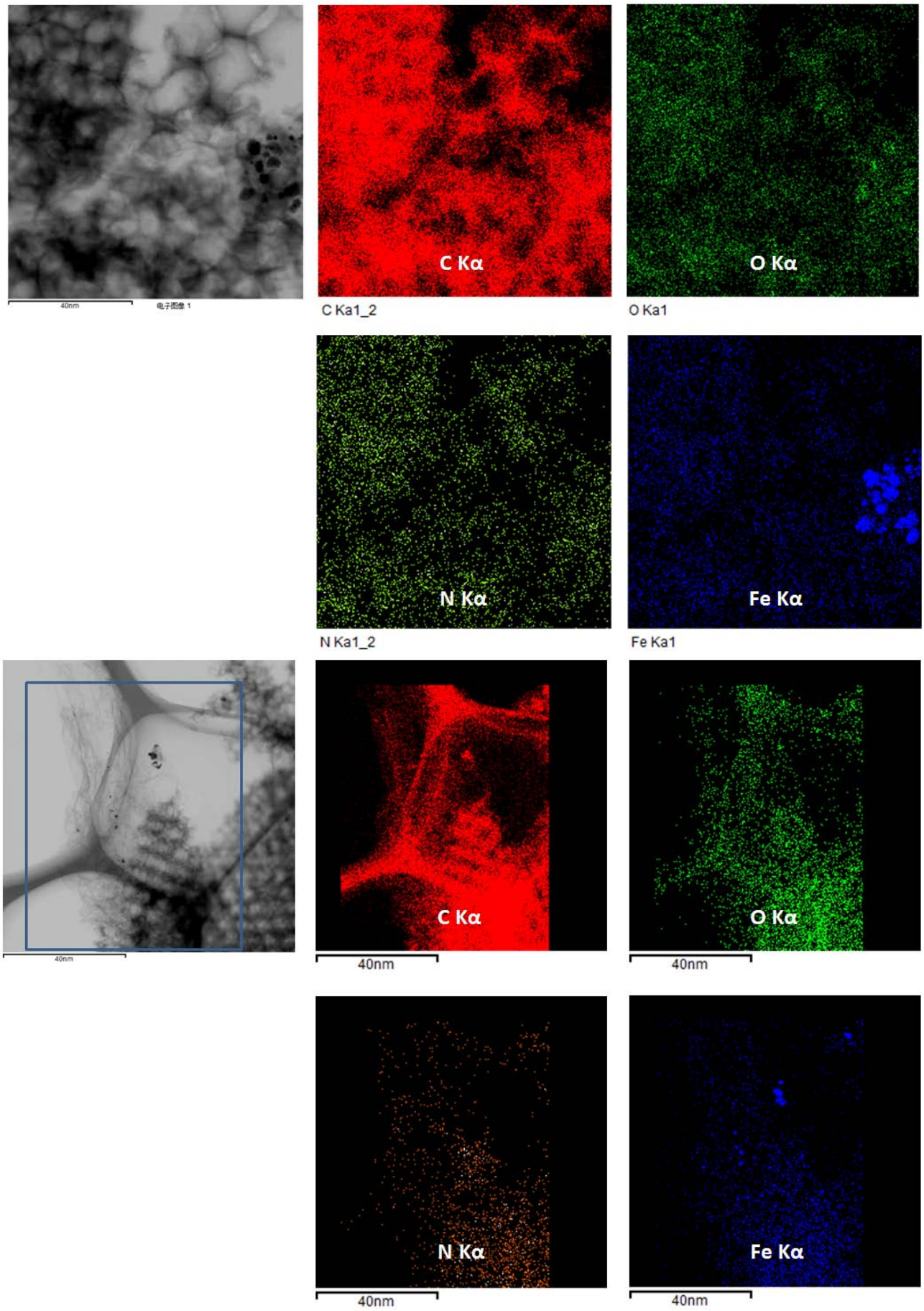

Figure S7. Elemental mappings of two regions on Fe-N-G-HPC sample.

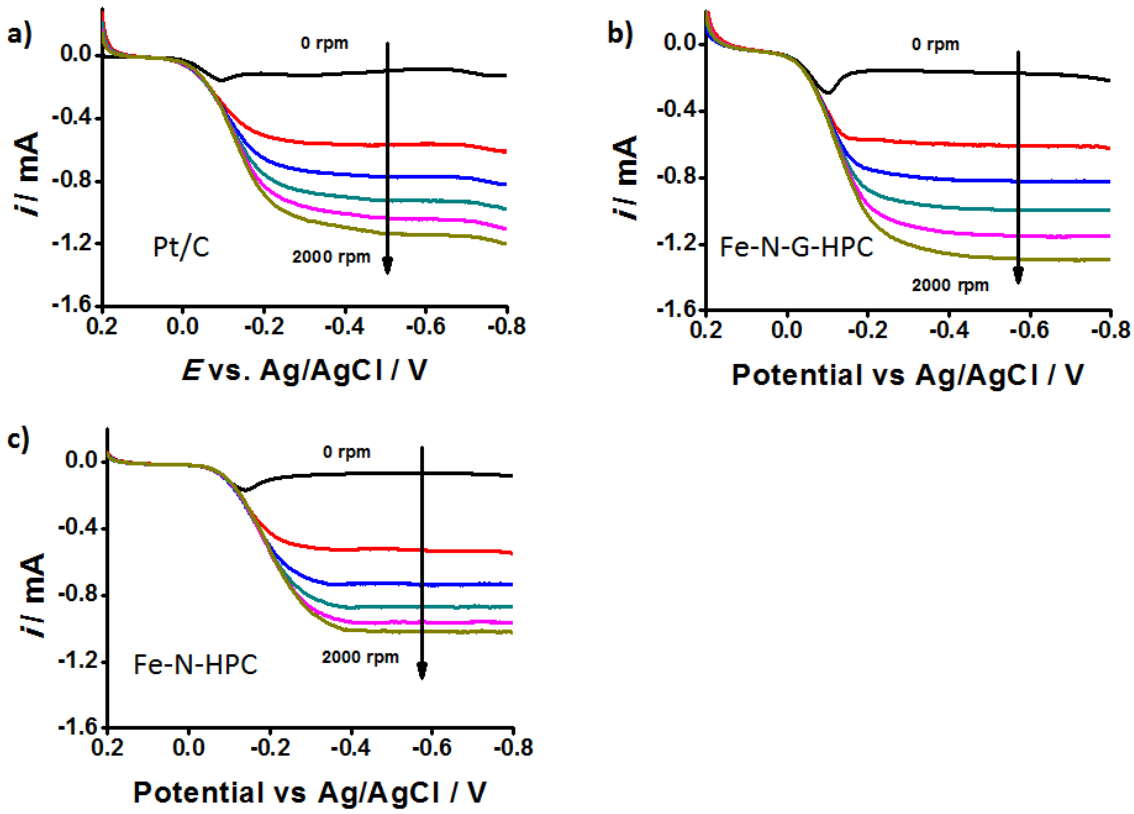

Figure S8. RDE voltammograms of (a) Pt/C, (b) Fe-N-G-HPC and (c) Fe-N-HPC samples obtained at different rotating speeds.

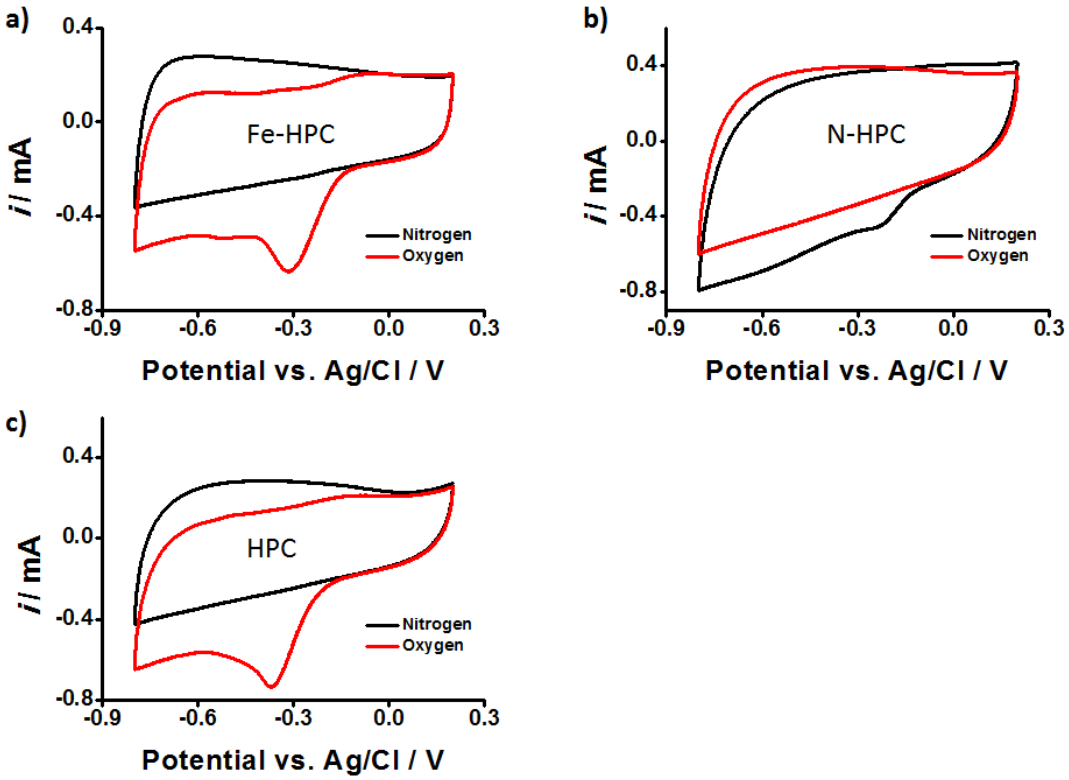

Figure S9. CV loops of (a) Fe-HPC, (b) N-HPC and (c) HPC samples.

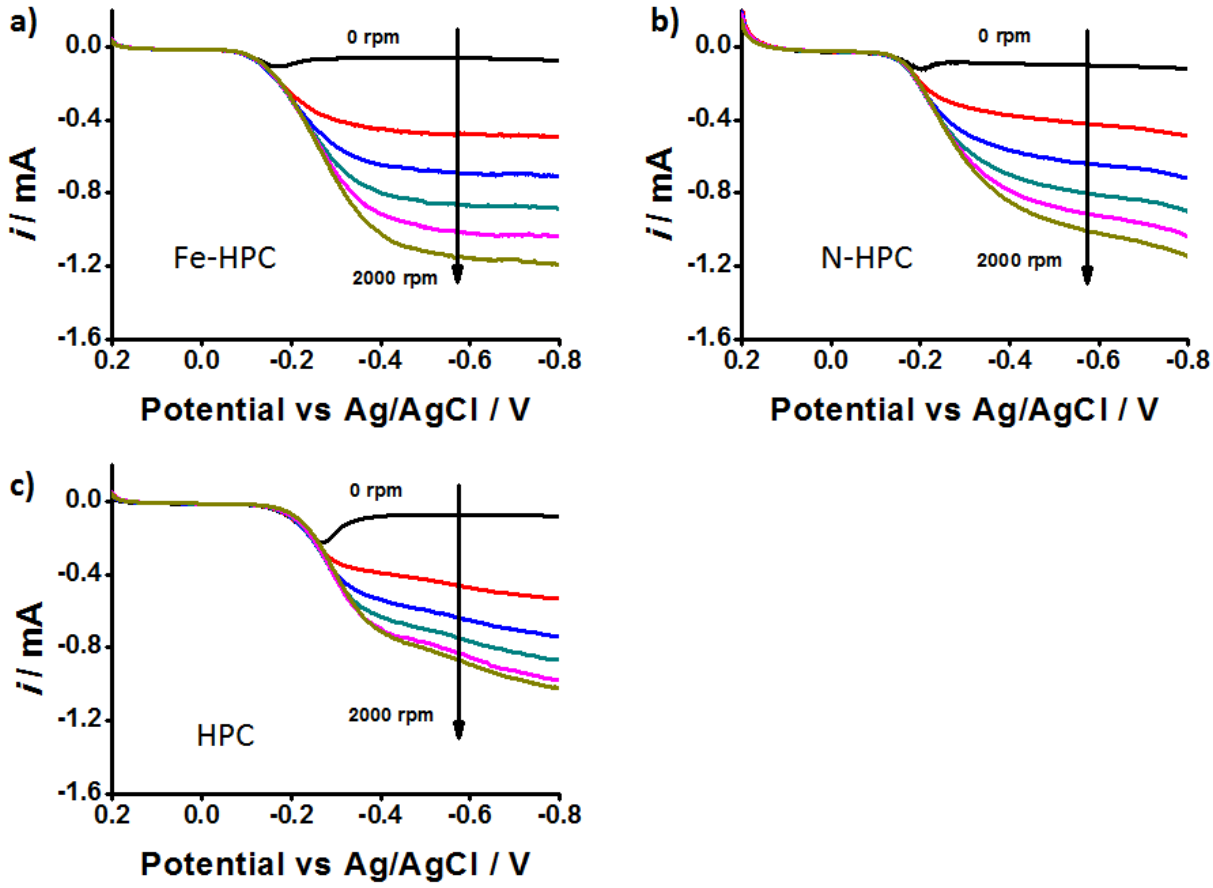

Figure S10. RDE voltammograms of (a) Fe-HPC, (b) N-HPC and (c) HPC samples.

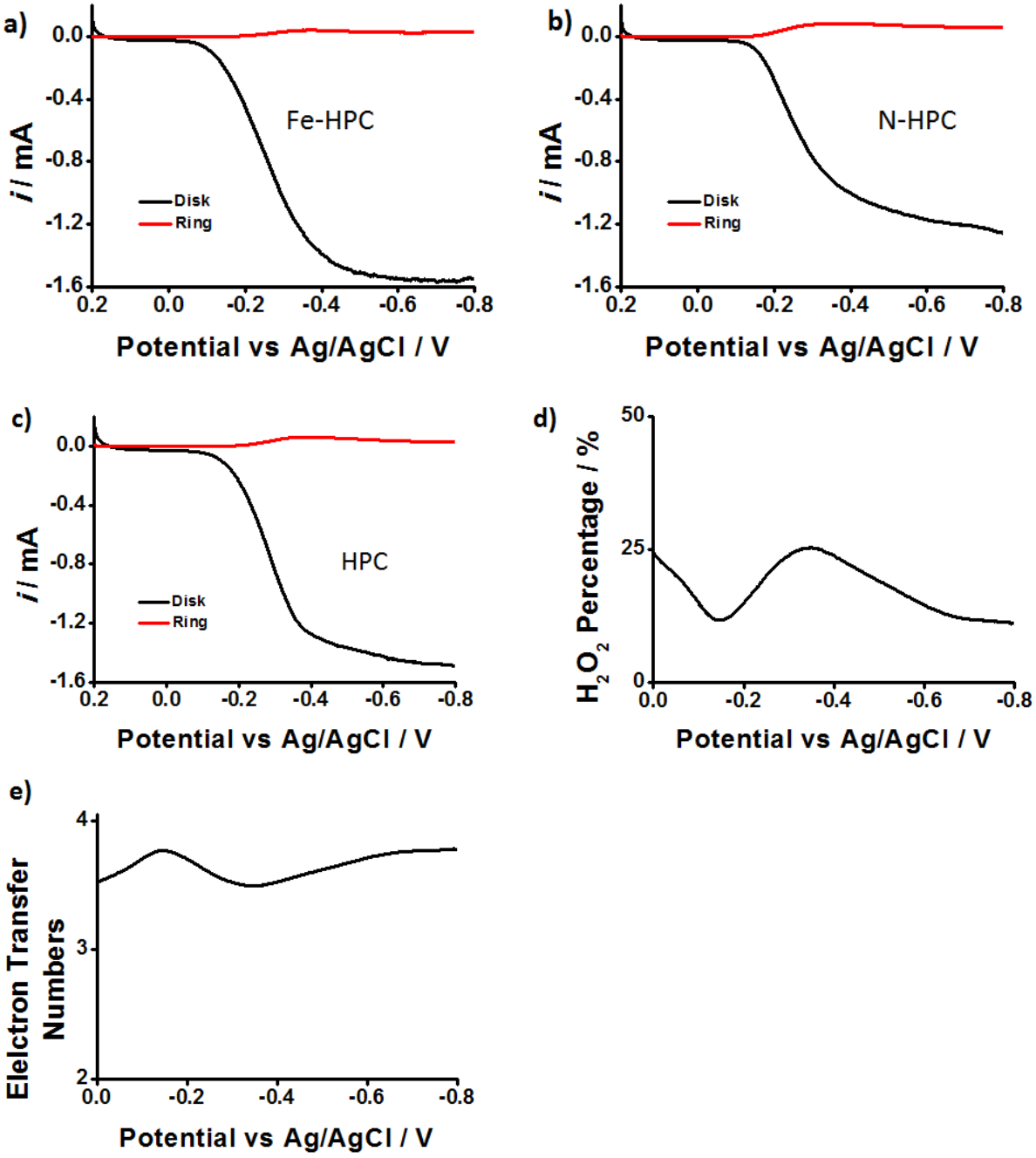

Figure S11. RRDE voltammograms at different rotating speeds of (a) Fe-HPC, (b) N-HPC samples and (c) HPC; and (d) the peroxide product and (e) electron transfer numbers of HPC.

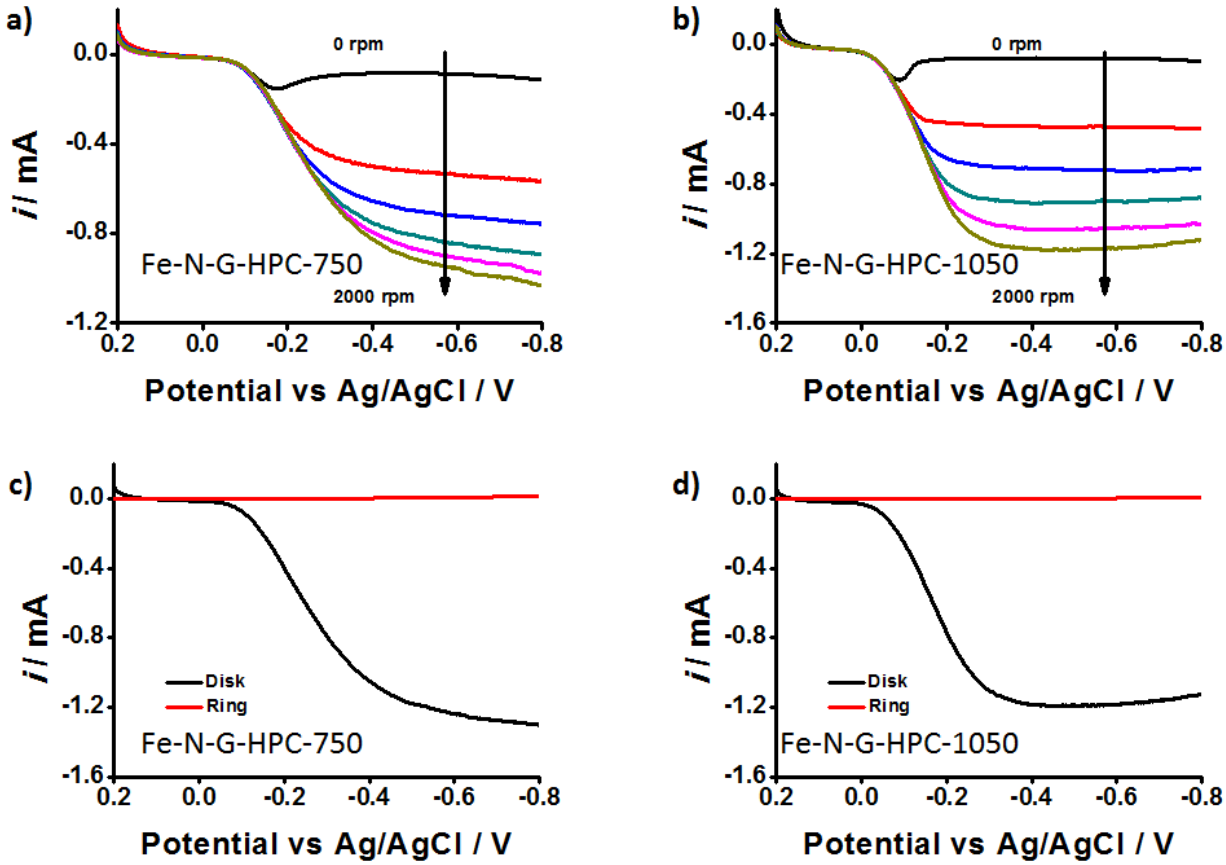

Figure S12. RDE voltammograms of different rotation speeds of (a) Fe-N-G-HPC-750 and (b) Fe-N-G-HPC-1050; and the RRDE voltammograms of (c) Fe-N-G-HPC-750 and (d) Fe-N-G-HPC-1050.

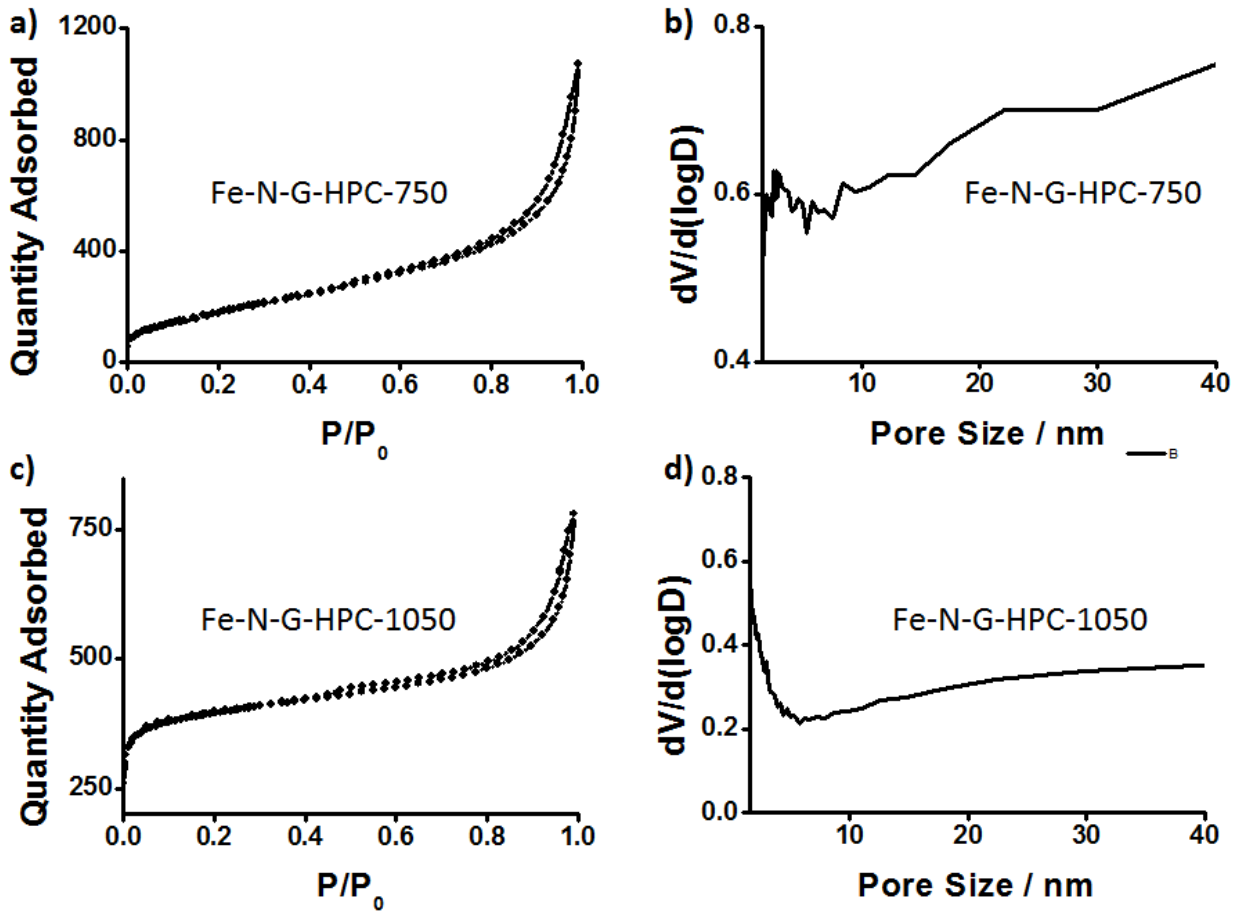

Figure S13. Nitrogen adsorption-desorption isotherms and the corresponding pore size distribution of (a, b) Fe-N-G-HPC-750 and (c, d) Fe-N-G-HPC-1050.

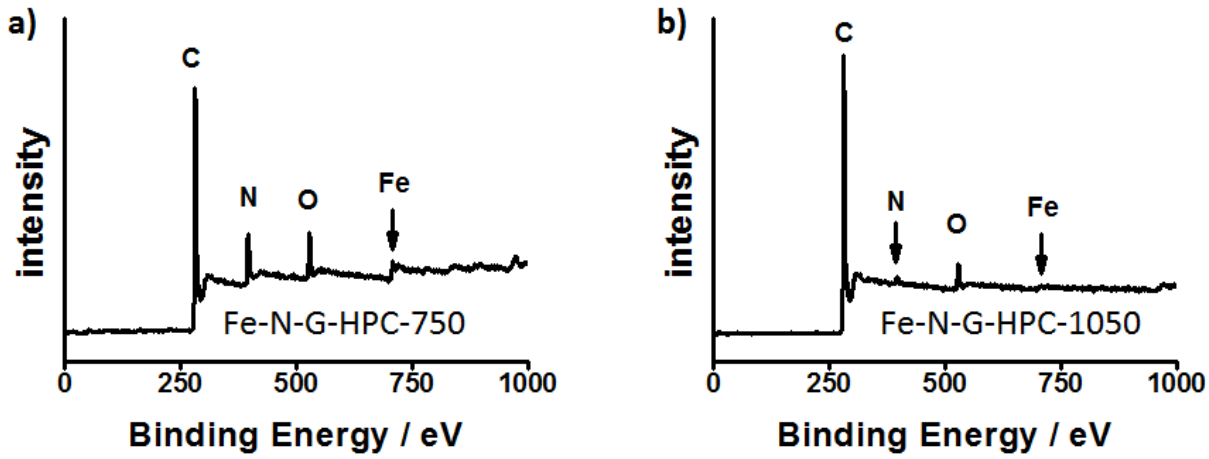

Figure S14. XPS survey scans of (a) Fe-N-G-HPC-750 and (b) Fe-N-G-HPC-1050.

Table S2

Content (at. %)	Fe	N	O	C
Fe-N-G-HPC-750	0.38	11.92	5.94	81.76
Fe-N-G-HPC	0.15	2.40	5.43	92.01
Fe-N-G-HPC-1050	0.09	1.68	3.31	94.92

Table S2. The content of different elements in the samples obtained from the XPS results in Figure S14.

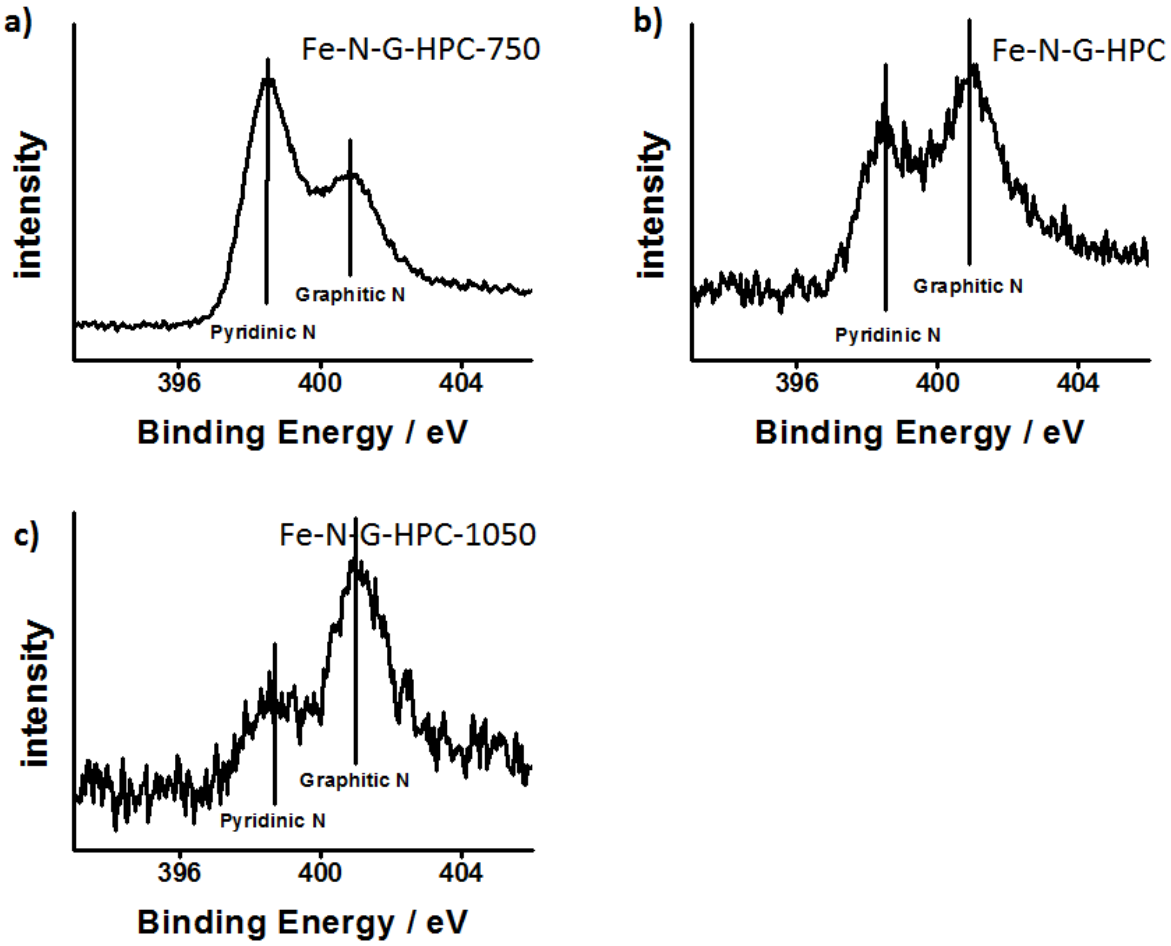

Figure S15. High resolution N1s spectra of (a) Fe-N-G-HPC-750, (b) Fe-N-G-HPC and (c) Fe-N-G-HPC-1050.

Chapter 6 Origin of the Synergistic Effect of Dual Dopants on Carbon for Metal-free ORR Catalysis

6.1 Introduction, Significance and Commentary

Graphene doped by heteroelement can electrochemically reduce oxygen and thus can be considered as a potential substitute for the expensive Pt/C to be used in a fuel cell or lithium-air battery. In this work, we have prepared S and N dual-doped mesoporous graphene and studied its oxygen reduction catalytic activity. It is found that the new metal-free catalyst has excellent catalytic performance. Further mechanism studies through experiment and density functional theory (DFT) calculation indicate that the synergistic effect of multiple heteroelements plays a key role on the performance enhancement. The highlights in work include:

1 We have for the first time achieved S and N dual-doping on graphene (S-N-graphene) by one-step method using simple and solid precursors. The new method can prevent the formation of any inactive side-product (e.g. BN in B-N-graphene) which does not have any catalytic activity to oxygen reduction reaction (ORR).

2 We also have for the first time introduced large mesopores into graphene to boost the mass transfer by using very cheap commercial colloidal silica nanoparticle as a hard template. The process is time efficient, low-cost and non-hazardous.

3 The oxygen reduction catalytic activity of S-N-graphene is significantly higher than the graphene solely doped by S or N, and is closely comparable with the commercial Pt/C. The new catalyst has also shown a completely methanol tolerance and excellent long-term stability, which is much superior to the commercial Pt/C.

4 We have then revealed and identified the synergistic nature of the two dopants in the graphene framework through density functional theory (DFT). Our study indicates that it is the large spin and charge densities redistribution brought by dual-doping of S and N atoms that leads to the significant performance enhancement.

6.2 Sulfur and Nitrogen Dual-doped Mesoporous Graphene Electrocatalyst for Oxygen Reduction with Synergistically Enhanced Performances

This section is included in the thesis as it appears as a back cover paper published by J. Liang, Y. Jiao, M. Jaroniec and S. Z. Qiao. Sulfur and Nitrogen Dual-doped Mesoporous Graphene Electrocatalyst for Oxygen Reduction with Synergistically Enhanced Performances, Angew. Chem. Int. Ed., 2012, 51, 11496

Statement of Authorship

Statement of Authorship

Title of Paper	Sulfur and Nitrogen Dual-Doped Mesoporous Graphene Electrocatalyst for Oxygen Reduction with Synergistically Enhanced Performance
Publication Status	◉ Published, ○ Accepted for Publication, ○ Submitted for Publication, ○ Publication style
Publication Details	Published on Angewandte Chemie International Edition (Back cover, hot paper, impact factor 13.734) Issue published online: 7 NOV 2012 Article first published online: 10 OCT 2012 Manuscript Received: 20 AUG 2012 DOI: 10.1002/anie.201206720

Author Contributions

By signing the Statement of Authorship, each author certifies that their stated contribution to the publication is accurate and that permission is granted for the publication to be included in the candidate's thesis.

Name of Principal Author (Candidate)	Ji Liang (First Author)		
Contribution to the Paper	Research plan, material synthesis, most of the characterizations, material performance assessment, manuscript drafting.		
Signature		Date	23/5/2014

Name of Co-Author	Dr. Yan Jiao		
Contribution to the Paper	Assistance with essential calculation section in the research, paper drafting and revising.		
Signature		Date	28/04/2014

Name of Co-Author	Prof. Mietek Jaroniec		
Contribution to the Paper	Assistance with manuscript revising and drafting		
Signature		Date	4/28/2014

Name of Co-Author	Prof. Shizhang Qiao		
Contribution to the Paper	Design of the project, organisation of the research and supervision Corresponding author, assistance with manuscript revise and drafting		
Signature		Date	23/5/2014

A Journal of the Gesellschaft Deutscher Chemiker

Angewandte Chemie

International Edition

GDCh

www.angewandte.org

2012–51/46

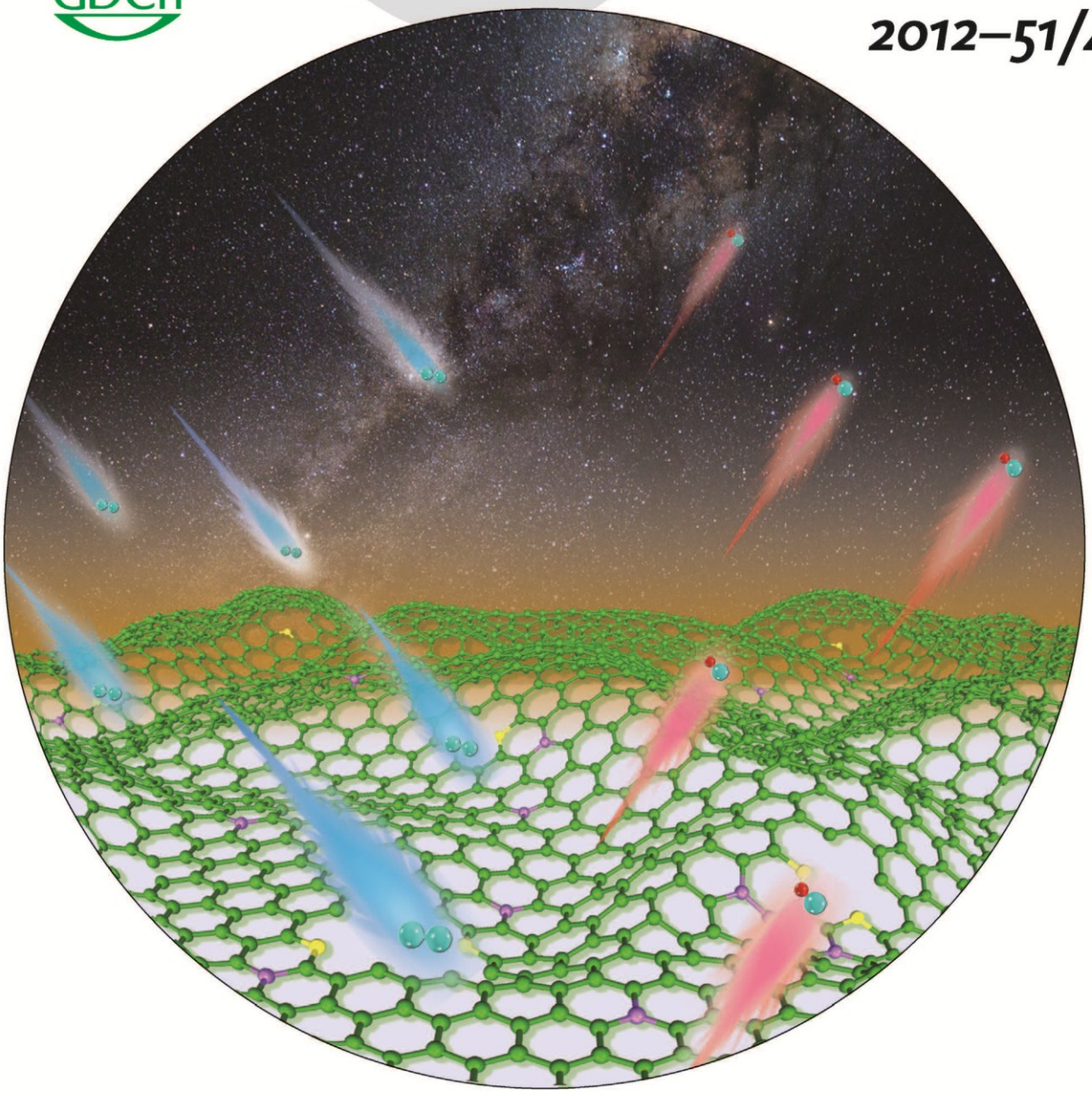

Developing highly active and cheap catalysts ...

... for the oxygen reduction reaction (ORR) is crucial to the commercialization of fuel cells and lithium–air batteries. In their Communication on page 11496 ff., S. Z. Qiao et al. describe an inexpensive mesoporous graphene catalyst dual-doped with sulfur and nitrogen that has high ORR activity. The superior performance can be attributed to synergistic effects between the dopants, resulting in increased spin and charge densities.

WILEY-VCH

Heterogeneous Catalysis

DOI: 10.1002/anie.201206720

Sulfur and Nitrogen Dual-Doped Mesoporous Graphene Electrocatalyst for Oxygen Reduction with Synergistically Enhanced Performance**

*Ji Liang, Yan Jiao, Mietek Jaroniec, and Shi Zhang Qiao**

The oxygen reduction reaction (ORR) is a key process in energy conversion and storage in, for example, fuel cells[1] and metal–air batteries[2] as well as in other applications including water purification, oxygen detection, and corrosion protection.[3] In lithium–air batteries and low-temperature fuel cells ORR takes place almost exclusively on Pt/C catalysts at the cathode. However, the high price, sluggish ORR process, intolerance to fuel crossover, and instability of the Pt/C catalyst in the fuel-cell environment have greatly impeded the commercialization of fuel cells and limited their performance.[1] Therefore, extensive studies have been conducted to find alternative metal-based catalysts with or without Pt, which could be viable from an economical viewpoint; however, current results are far from satisfactory.[4,5] Thus, there has been great interest in the development of metal-free catalysts for ORR. For this purpose, N-doped carbons have been extensively studied. Their potential for ORR originates from the heteroatoms present in the graphitic framework, which make these catalysts non-electron-neutral and consequently favors the molecular adsorption of oxygen and its reduction. Although moderate ORR performance has been obtained on these materials, their ORR activity is still inferior to that of conventional Pt/C catalysts.[6,7]

Among carbon materials, graphene, the ultrathin two-dimensional network composed of sp^2-hybridized carbon atoms, has become a very popular candidate for ORR catalysis because of its high conductivity and excellent mechanical properties,[8] which are greatly favorable for the harsh ORR process. Recently, other elements besides N (e.g. B, S, and I) have been introduced into graphene.[9–11] Although these newly developed doped-graphene materials have shown better performance than the N-doped materials, the improvement in the ORR catalytic activity has been very limited owing to the low content of the doped elements. To address this issue, some researchers have proposed to dope graphene with both B and N to further improve the ORR catalytic activity, since this is controlled not only by the increased number of dopant heteroatoms but also by the synergistic effects between the dopants.[3,12] However, in the high-temperature doping process that uses boric acid and ammonia as the B and N precursors, boron nitride (BN) is inevitably formed; as BN is catalytically inactive for ORR and is electrically insulating, the overall performance of the resulting catalyst is compromised. Besides, if one considers the relatively poor ORR activity of graphene doped solely with B,[11] further improvement in performance could be expected if additional "active" elements were selected. Based on our recent work on the effect of the nanostructures of metal-free g-C_3N_4/C catalysts on ORR performance, relatively large and regular pores are more favorable than randomly formed inaccessible narrow pores;[9–11,13] these features have been rarely considered in studies on graphene-based materials for ORR.

Herein, we report for the first time the design and one-step synthesis of N and S dual-doped graphene (N-S-G) without the formation of any side products. The main focus of this research is to develop a high-performance metal-free ORR electrocatalyst to replace Pt/C as well as to gain insight into the synergistic effects originating from multiple-element doping. By selecting highly active S and N atoms as dopants, we achieved dual-doped N-S-G catalysts with excellent ORR performance comparable to that of commercial Pt/C and significantly better than that of graphene catalysts doped solely with S atoms (S-G) or with N atoms (N-G). Also, both dopant elements in N-S-G are efficiently utilized for ORR catalysis and do not form inactive compositions. The outstanding performance of N-S-G is explained by its dual activation of C atoms, as evidenced by both experimental data and quantum chemistry calculations. Moreover, we also used commercially available colloidal silica nanoparticles to create large mesopores for the first time in the graphene catalyst which are favorable for ORR since they facilitate mass transfer.[12] Besides, compared to the fuel-sensitive and vulnerable Pt/C, the proposed N-S-G material is much more tolerant to fuel crossover and displays long-term durability in alkaline environment. This N-S-G material not only presents a very promising substitute for expensive Pt/C as a low-cost fuel-cell catalyst, but it also has potential in other applications such as lithium–air batteries, photocatalysis, and heterocatalysis.

Mesoporous N-S-G was prepared through a one-step doping process as illustrated in Scheme 1. Graphene oxide (GO) was first prepared by Hummer's method and dispersed

[*] J. Liang, Y. Jiao, Prof. S. Z. Qiao
School of Chemical Engineering
The University of Adelaide, SA 5005 (Australia)
E-mail: s.qiao@adelaide.edu.au
M. Jaroniec
Department of Chemistry and Biochemistry
Kent State University, Kent, 44242 OH (USA)

[**] This work was financially supported by the Australian Research Council (ARC) through the Discovery Project program (DP1095861, DP0987969).

Supporting information for this article is available on the WWW under http://dx.doi.org/10.1002/anie.201206720.

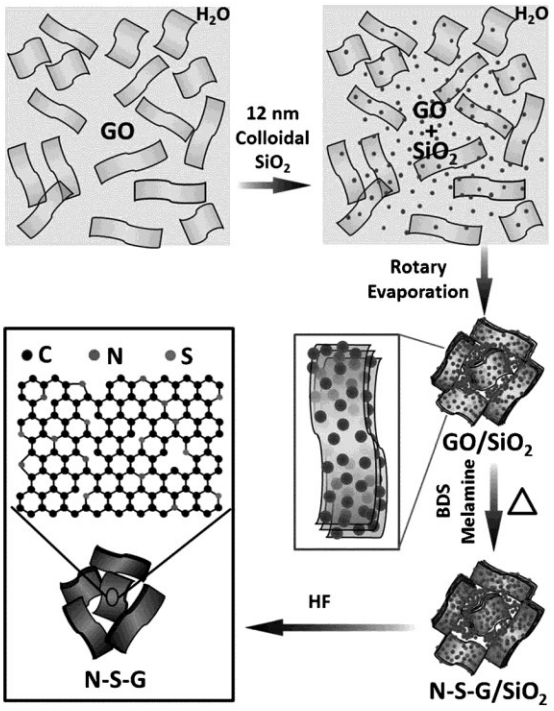

Scheme 1. Fabrication of N and S dual-doped mesoporous graphene (N-S-G) nanosheets from graphene oxide. See test for details.

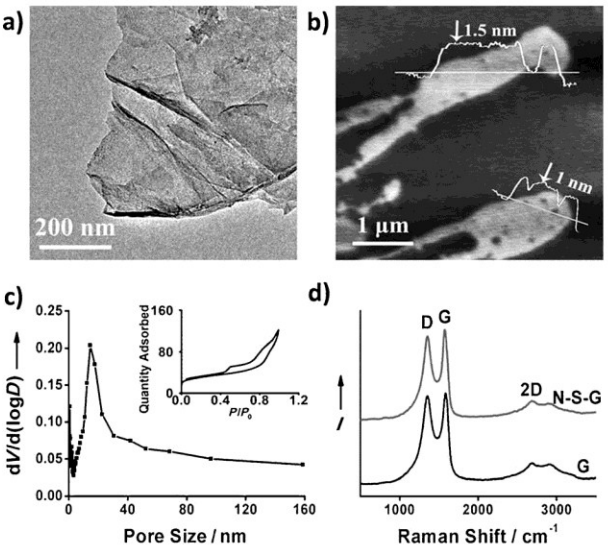

Figure 1. Characterization of typical N-S-G nanosheets. a,b) TEM and AFM images, respectively, c) pore size distribution and the corresponding nitrogen adsorption-desorption isotherms (inset), d) Raman spectra of N-S-G and pristine graphene (G).

in water.[14] Then commercial colloidal silica (12 nm), as the structural template, was added into the GO/water dispersion to achieve a SiO_2/GO weight ratio of 5:1. Water was removed by rotary evaporation, resulting in a brown crispy GO/SiO_2 composite. Melamine and benzyl disulfide (BDS) were selected as N and S precursors, respectively, and the doping process was carried out by heating the mixture of melamine/BDS/GO/SiO_2 (weight ratio of 5:5:1:5) at 900 °C in Ar to form N-S-G/SiO_2. The porous structure was formed in the N-S-G afterward by removing SiO_2 nanoparticles with hydrofluoric acid (HF). Mesoporous N-G and S-G, as well as pristine mesoporous graphene (G), were also prepared under similar conditions for comparison purposes.

The as-prepared mesoporous N-S-G was first investigated by transmission electron microscopy (TEM) and scanning electron microscopy (SEM) (images in Figure 1a and Figures S1 and S2 in the Supporting Information). Large amounts of transparent graphene nanosheets can be readily observed. Remarkably, the mesoporous N-S-G shows a very loose structure (Figures S1 and S2) similar to that of freeze-dried graphene aerogels but different from that of the typical densely packed graphene papers prepared without SiO_2.[15,16] Further structural details are also evident in the atomic force microscopy images (AFM) shown in Figure 1b and Figure S3. The AFM linear scan confirms that the thickness of a single graphene sheet is 1–1.5 nm, indicating 3–6 carbon atomic layers. Randomly located surface dents are also evident in the AFM image, which could result from defects in the doped graphene and might provide more high-energy edges that can act as active sites for ORR.

The porosity of N-S-G was investigated by nitrogen-adsorption technique. The nitrogen-adsorption isotherm of N-S-G (inset in Figure 1c) is of type IV with a distinct hysteresis loop in the medium- and high-pressure regions ($P/P_0 = 0.4$–1). The size of mesopores in the material range from 10 to 40 nm (Figure 1c, pore-size distribution calculated by the Barrett–Joyner–Halenda method); these are much larger than the mesopores in the previously reported graphene materials as a result of the silica template. These mesopores are expected to facilitate the diffusion of reactants in the ORR process.[13,17,18]

Further structural information about the doped graphene was obtained from Raman spectra (Figure 1d). A typical D band resulting from the disordered carbon atoms and a G band from sp^2-hybridized graphitic carbon atoms can be observed at roughly 1350 cm^{-1} and 1580 cm^{-1}, respectively.[12] Interestingly, the I_D/I_G ratio of N-S-G is similar to that of pristine graphene (G), which is lower than that of both N-G and S-G (Figure S4a), indicating larger crystalline graphitic domains in N-S-G.[19] The origin of these larger graphitic domains in the dual-doped graphene needs further study.

The doping of heteroelements into graphene was first probed by energy-dispersive spectrometry (EDS). The EDS spectrum indicates the presence of N, S, and O elements in graphene (Figure S4b), while the EDS elemental mapping of N and S, which is integrated onto the TEM image of the same region, illustrates a homogeneous distribution of S and N species in N-S-G (Figure 2a). Considering that both the N and S precursors were completely removed at temperatures below 750 °C in Ar, as shown by thermal gravimetric analysis (TGA) (Figure S5), it is reasonable to believe the N and S atoms belong to the doped graphene, rather than to any residual precursors. The chemical status of these elements was further investigated by X-ray photoelectron spectroscopy (XPS). The

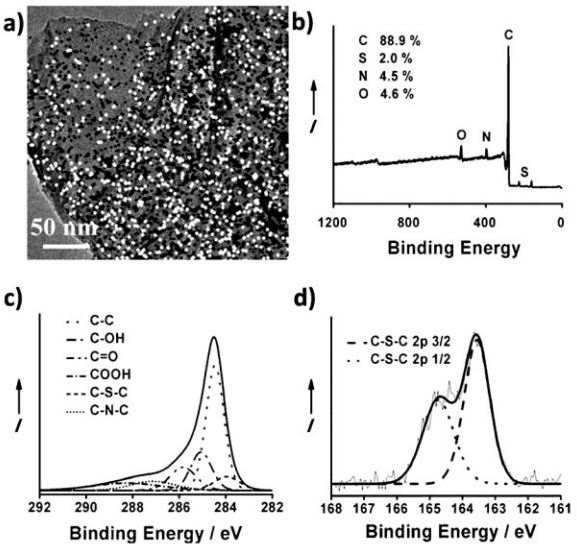

Figure 2. Compositional analysis of N-S-G. a) EDS elemental mapping indicating the distribution of N (black dots) and S atoms (white dots), b) XPS sweep scan, and the corresponding high-resolution spectra of c) C1s and d) S2p. The two peaks in (d) originate from the 2p 3/2 and 2p 1/2 splitting of the S2p spin orbital.

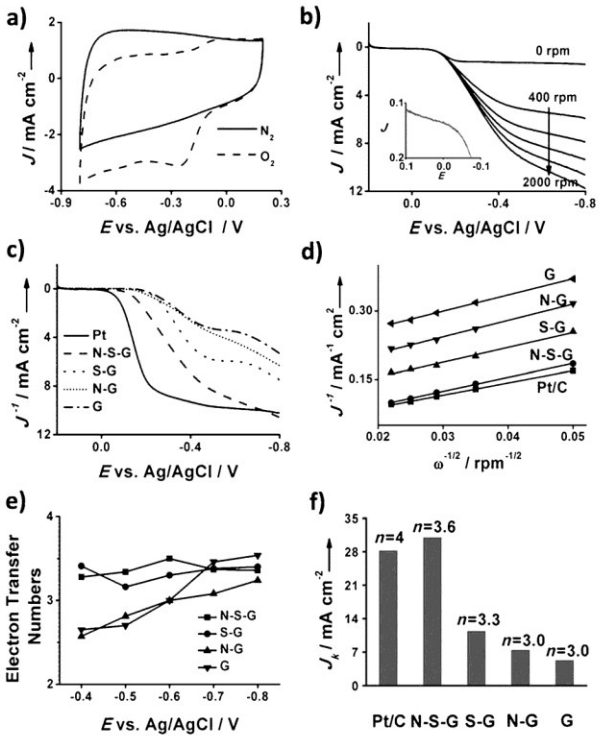

Figure 3. Electrochemical ORR catalytic performance of samples. a) CV curves of N-S-G in O_2- or N_2-saturated electrolyte. b) LSVs of N-S-G at different rotating speeds; the inset shows an enlargement of the initial region. c) LSVs of different samples at 1600 rpm. d) K-L plots of different samples at −0.6 V. e) Electron-transfer numbers as a function of the overpotential of different samples. f) Kinetic limiting current of different samples as well as the corresponding electron-transfer numbers at −0.6 V.

survey scan of N-S-G (Figure 2b) shows the identical elemental composition as that obtained from EDS. The N and S elemental content (4.5 atom% and 2.0 atom%, respectively) of the dual-doped N-S-G is comparable to that of the single-element-doped graphene materials (5.1 atom% of N in N-G and 1.3 atom% of S in S-G as shown in Figures S6a and S7a). The high-resolution spectrum of C1s in N-S-G (Figure 2c) can be deconvoluted into several single peaks, corresponding to C-S-C (283.9 eV)[20] and C-N-C (287.2 eV),[13,21] further confirming that N and S heteroatoms have been doped into the graphene framework. Different oxygen-containing groups (COOH, C=O, and C-OH) were also observed on N-S-G, similar to N-G, S-G, and pristine thermally reduced graphene (Figures S6b, S7b, and S9). Remarkably, N-S-G and S-G contain sulfur atoms that form thiophene-like structures with neighboring carbon atoms, as shown in the high-resolution S2p spectrum (Figure 2d and Figure S7c); SO_x groups, which are chemically inactive for ORR, are not evident.[9] On the other hand, the high-resolution N1s spectra of N-S-G and N-G (Figures S8 and S6c) show three nitrogen species, which are typically observed in the case of N-doped carbons.

The ORR catalytic performance of N-S-G was first investigated by cyclic voltammetry (CV) (Figure 3a); comparative studies were performed for N-G, S-G, and G (Figure S10). A quasi-rectangular voltammogram without obvious redox peak was obtained when the electrolyte was saturated with N_2, as a result of the the typical supercapacitance effect on porous carbon materials.[22,23] In contrast, when O_2 was introduced, a well-defined characteristic ORR peak, centered at −0.24 V with a reaction current of $-3.3\ mA\,cm^{-2}$, was observed with N-S-G. The ORR reaction current on N-S-G is apparently higher than on the solely doped N-G or S-G (Figure S10) or the pristine G. Moreover, the peak potential for N-S-G is also more positive than that of other recently reported metal-free ORR catalysts such as N-graphene,[17] S-graphene,[9] g-C_3N_4/C,[21] and co-doped graphenes,[12] indicating a more facile ORR process on this dual-heteroatom-doped N-S-G.

To gain additional insight about the ORR process on this dual-doped graphene, linear sweep voltammograms (LSVs) on a rotating disc electrode (RDE) were recorded at different rotating speeds from 0 rpm to 2000 rpm in 0.1 M KOH electrolyte saturated with O_2; for the purpose of comparison, analogous LSV curves were obtained for N-G, S-G, and G as well as for commercial 20 wt% Vulcan Pt/C (Figure 3b and Figure S11). Typically, the current simultaneously increased as the potential became more negative, which is commonly observed on metal-free ORR catalysts with mesopores.[21] Remarkably, N-S-G displayed a very high ORR onset potential of −0.06 V (inset in Figure 3b), which is close to that of commercial Pt/C (−0.03 V) and much more positive than that of N-G, S-G, or G (ca. −0.18 V) (Figure 3c) at 1600 rpm. On the other hand, the ORR reaction current of N-S-G is also explicitly higher than that of other samples over the whole potential range, agreeing with the CV results. The more positive onset potential as well as the higher reaction current on N-S-G indicate that this material would have

clearly better catalytic performance and also supports the proposed synergistic effect caused by dual N and S doping.

To qualify the ORR process on this novel catalyst, the Koutecky–Levich (K-L) plots (J^{-1} vs. $\omega^{-1/2}$) were obtained for each sample from the reaction currents at −0.6 V on the LSVs at various rotating speeds (Figure 3d); the K-L plots were also obtained at other potentials as illustrated in Figure S12. The plots of all samples show good linearity, and noticeably, the N-S-G sample shows a high ORR current, which is very close to that of the commercial Pt/C catalyst and significantly higher than those of S-G, N-G, and pristine G at all rotation speeds; this is further indication of the outstanding ORR catalytic performance on the dually doped graphene as compared with the solely doped or nondoped materials. The electron-transfer numbers (n) of all the samples at different potentials were calculated according to the slopes of the linear fitted K-L plots on the basis of the K-L equation (Figure 3e; for details see the Supporting Information). Generally increasing n values were obtained for N-G, S-G, and G as the potential became more negative, while n for N-S-G was more stable and higher at 3.3–3.6 over most of the potential range. The higher and steadier electron-transfer numbers indicate a smoother and more electrochemically stable ORR process over N-S-G.

To more clearly determine the potential suitability of N-S-G as an ORR catalyst, we acquired the kinetic limiting current (J_k) from the intercept of the linearly fitted K-L plots at −0.6 V (Figure 3f) and at other potentials (Figure S12). Significantly, the J_k value of N-S-G exceeded that of commercial Pt/C at −0.6 V and was much superior to that of N-G, S-G, and G over the whole potential range. Taking into account that the J_k value of N-S-G is substantially higher than the summed value of N-G and S-G (corrected for heteroelement content), we believe that the excellent ORR performance is not simply the result of the superposition of the reaction currents due to N and S doping. Moreover, the J_k value of N-S-G sharply increased from 15 mA cm^{-2} to 52 mA cm^{-2} as the potential varied from −0.4 V to −0.8 V (Figure S12) and its value became nearly twice as high as that of Pt/C (52 mA cm^{-2} vs. 28 mA cm^{-2} at −0.8 V), which is a good indication that the potential current can be improved even further through structural modification.[13]

High selectivity towards ORR is important for potential fuel-cell catalysts to prevent possible fuel-crossover effects. In this study, the tolerance of N-S-G to methanol crossover was assessed in comparison with that of the commercial Pt/C catalyst (Figure S13a). When methanol was introduced into the testing cell, the current response of N-S-G remained unchanged, showing its high catalytic selectivity for ORR against methanol oxidation. In contrast, Pt/C showed an instantaneous current jump upon addition of methanol, reflecting its sensitivity to fuel crossover. The durability of N-S-G and Pt/C was also evaluated (Figure S13b). A 60 h test of N-S-G showed only a very slight performance attenuation of 19%. In contrast, the Pt/C catalyst suffered an activity loss of nearly 40%. The higher stability of the metal-free catalyst can be attributed to the strongly bonded heteroatoms in N-S-G and the improved chemical and mechanical stability of the mesoporous graphene relative to that of the carbon-black-based Pt/C, which could effectively prevent the loss of active sites.

The synergistic effect of the two dopants in enhancing ORR performance could be better studied and understood by employing density functional theory (DFT) calculations. Graphene networks doped by N and/or S atoms with different relative positions have been constructed for computational simulation as illustrated in Figure S14. Whether an atom can serve as an active site for ORR depends on both its charge density and spin density, with the latter playing a more important role than the former.[24] For N-G, which is doped solely by more electronegative N atoms (electronegativity of 3.04),[25] the ORR activity mainly originates from the surrounding C atoms with high charge density (0.27 in Figure S15a).[24,26] For S-G, the electronegativity of the S (2.58) and C atoms (2.55) are quite close, and the charge transfer between S and C is negligible.[27] Thus, the catalytic behavior is mainly affected by the mismatch of the outermost orbitals of sulfur and carbon (Figure S15b); then the S atom is positively charged and hence can be viewed as the catalytic center for ORR.[9] Remarkably, when S and N are simultaneously incorporated into graphene to form dual-doped N-S-G, the maximum spin density is substantially uplifted to 0.43 (C1 in Figure 4) indicating significantly elevated ORR activity. A larger number of active C atoms is also observed (S and C1–C5 as shown in Figure 4),[24] because the dual-doping of S and N introduces asymmetrical spin and charge density. Simulations performed for other N-S-G models with different relative positions of the S and N atoms (Figure S16–19) also show that the charge/spin densities are increased to a certain extent, indicating higher ORR catalytic performance. All these features, including both higher activity and more active sites, can well explain the significant enhancement of ORR catalytic activity such as the more positive onset potential and higher reaction current on N-S-G relative to that on N-G or S-G.

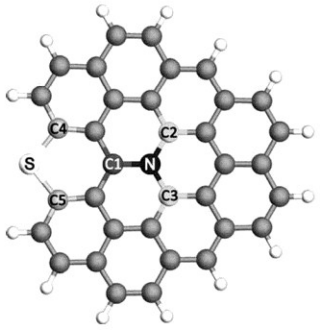

Atom Number	Spin Density	Charge Density
C1	0.43	0.23
C2	-0.03	0.28
C3	-0.03	0.28
C4	0.16	-0.22
C5	0.16	-0.22
N	0.06	-0.88
S	0.09	0.21

Figure 4. Spin and charge density of graphene network (gray) dual-doped by N (black) and S (white). C1 has very high spin density, C2 and C3 have high positive charge density, and C4 and C5 have moderately high positive spin densities.

In summary, we have described the first design and preparation of N and S dual-doped mesoporous graphene as a metal-free catalyst for ORR. This novel material shows

excellent catalytic activity including a highly positive onset potential and very high kinetic limiting current, which makes it closely comparable to the commercial Pt/C catalyst. The DFT calculations have revealed that the synergistic performance enhancement results from the redistribution of spin and charge densities brought about by the dual doping of S and N atoms, which leads to a large number of carbon atom active sites. This catalyst also shows a full fuel tolerance and much better long-term stability than Pt/C in alkaline environment. Moreover, this material can be prepared by a very simple one-step doping process using solid and low-cost precursors, and its porosity is introduced by employing commercially available colloidal silica; thus, it is easily adaptable for large-scale synthesis. Because of all these outstanding features, it is expected that the N-S-G material will be a very suitable catalyst for the next generation of fuel cells, and should find other applications as well such as in lithium–air batteries, photocatalysis, oxygen sensors, and water treatment.

Received: August 20, 2012
Published online: October 10, 2012

Keywords: graphene · heterogeneous catalysis · nanostructures · oxygen reduction reaction · synergistic effects

[1] B. C. H. Steele, A. Heinzel, *Nature* **2001**, *414*, 345.
[2] E. M. Erickson, M. S. Thorum, R. Vasic, N. S. Marinkovic, A. I. Frenkel, A. A. Gewirth, R. G. Nuzzo, *J. Am. Chem. Soc.* **2012**, *134*, 197.
[3] S. Wang, E. Iyyamperumal, A. Roy, Y. Xue, D. Yu, L. Dai, *Angew. Chem.* **2011**, *123*, 11960; *Angew. Chem. Int. Ed.* **2011**, *50*, 11756.
[4] R. Bashyam, P. Zelenay, *Nature* **2006**, *443*, 63.
[5] H. Gasteiger, N. Markovi, *Science* **2009**, *324*, 48.
[6] S. Maldonado, K. J. Stevenson, *J. Phys. Chem. B* **2005**, *109*, 4707.
[7] H. Wang, T. Maiyalagan, X. Wang, *ACS Catal.* **2012**, *2*, 781.
[8] A. Fasolino, J. H. Los, M. I. Katsnelson, *Nat. Mater.* **2007**, *6*, 858.
[9] Z. Yang, Z. Yao, G. Li, G. Fang, H. Nie, Z. Liu, X. Zhou, X. a. Chen, S. Huang, *ACS Nano* **2012**, *6*, 205.
[10] Z. Yao, H. Nie, Z. Yang, X. Zhou, Z. Liu, S. Huang, *Chem. Commun.* **2012**, *48*, 1027.
[11] L. Yang, S. Jiang, Y. Zhao, L. Zhu, S. Chen, X. Wang, Q. Wu, J. Ma, Y. Ma, Z. Hu, *Angew. Chem.* **2011**, *123*, 7270; *Angew. Chem. Int. Ed.* **2011**, *50*, 7132.
[12] S. Wang, L. Zhang, Z. Xia, A. Roy, D. W. Chang, J. B. Baek, L. Dai, *Angew. Chem.* **2012**, *124*, 4285; *Angew. Chem. Int. Ed.* **2012**, *51*, 4209.
[13] J. Liang, Y. Zheng, J. Chen, J. Liu, D. Hulicova-Jurcakova, M. Jaroniec, S. Z. Qiao, *Angew. Chem.* **2012**, *124*, 3958; *Angew. Chem. Int. Ed.* **2012**, *51*, 3892.
[14] W. S. Hummers, R. E. Offeman, *J. Am. Chem. Soc.* **1958**, *80*, 1339.
[15] S. Stankovich, D. A. Dikin, R. D. Piner, K. A. Kohlhaas, A. Kleinhammes, Y. Jia, Y. Wu, S. T. Nguyen, R. S. Ruoff, *Carbon* **2007**, *45*, 1558.
[16] F. Liu, S. Song, D. Xue, H. Zhang, *Adv. Mater.* **2012**, *24*, 1089.
[17] S. Yang, L. Zhi, K. Tang, X. Feng, J. Maier, K. Müllen, *Adv. Funct. Mater.* **2012**, DOI: 10.1002/adfm.201200186.
[18] S. Yang, X. L. Feng, X. C. Wang, K. Mullen, *Angew. Chem.* **2011**, *123*, 5451; *Angew. Chem. Int. Ed.* **2011**, *50*, 5339.
[19] M. Jin, T. H. Kim, S. C. Lim, D. L. Duong, H. J. Shin, Y. W. Jo, H. K. Jeong, J. Chang, S. Xie, Y. H. Lee, *Adv. Funct. Mater.* **2011**, *21*, 3496.
[20] S. Wan, L. Wang, Q. Xue, *Electrochem. Commun.* **2010**, *12*, 61.
[21] Y. Zheng, Y. Jiao, J. Chen, J. Liu, J. Liang, A. Du, W. Zhang, Z. Zhu, S. C. Smith, M. Jaroniec, G. Q. Lu, S. Z. Qiao, *J. Am. Chem. Soc.* **2011**, *133*, 20116.
[22] R. Liu, D. Wu, X. Feng, K. Müllen, *Angew. Chem.* **2010**, *122*, 2619; *Angew. Chem. Int. Ed.* **2010**, *49*, 2565.
[23] W. Yang, T.-P. Fellinger, M. Antonietti, *J. Am. Chem. Soc.* **2011**, *133*, 206.
[24] L. Zhang, Z. Xia, *J. Phys. Chem. C* **2011**, *115*, 11170.
[25] A. L. Allred, *J. Inorg. Nucl. Chem.* **1961**, *17*, 215.
[26] K. Gong, F. Du, Z. Xia, M. Durstock, L. Dai, *Science* **2009**, *323*, 760.
[27] S. Glenis, A. J. Nelson, M. M. Labes, *J. Appl. Phys.* **1999**, *86*, 4464.

6.3 Supplimentary Information

This section is included in the thesis as as a supplimentary information to setion 6.2. It includes additional information which is not put in the main text of the published papr, but as an electronic sullimentrary information freely accessable online.

Supporting Information

69451 Weinheim, Germany

Sulfur and Nitrogen Co-doped Mesoporous Graphene Electrocatalyst for Oxygen Reduction with Synergistically Enhanced Performance

*Ji Liang, Yan Jiao, Mietek Jaroniec, Shi Zhang Qiao**

Correspondence and requests for materials should be addressed to:

s.qiao@adelaide.edu.au (S.Z. Qiao)

I. Experimental Section

1. Chemical

Graphite flakes, sulfuric acid (H_2SO_4, 95-98 %), potassium permanganate ($KMnO_4$, 99 %), phosphorus pentoxide (P_2O_5, 98 %), potassium persulfate ($K_2S_2O_8$, 99 %), colloidal silica (Ludox HS-40, 40 % water suspension), benzyl disulfide (BDS, $C_6H_5CH_2SSCH_2C_6H_5$, 98 %), melamine (99 %), hydrofluoric acid (HF, 48 %) were purchased from Sigma-Aldrich and directly used without further treatment or purification.

2. Preparation of nitrogen and sulfur dual-doped mesoporous graphene

Graphene oxide (GO) was prepared through the modified Hammer's method.[1] GO was dispersed into deionized water to obtain a 0.05 wt.% suspension. 1.25 g of colloidal silica containing 40 wt.% 12 nm silica nanospheres was added to 200 ml of the aforementioend GO suspension. Then, the resulting aqueous mixture was rotary evaporated at 60 °C, and a crisp brown solid was obtained (*ca.* 0.6 g). Afterwards, the solid was slightly crashed in a motar with 0.5 g melamin and 0.5 g BDS into fine power. The mixture was then heated at 900 °C for 1 h under the protection of Ar to obtain N-S-G/SiO_2. The as-prepared sample was finally washed with HF acid to remove the silica, followed by water washing and drying at 100 °C. For the purpose of comparsion, N-G, S-G and G were also prepared similarly by using single nitrogen or sulfur presursor or in the abscence of any precursor, respectively.

3. Characterization

Nitrogen adsorption-desorption isotherm was recorded on Tristar II (Micrometrics) at -196 °C. Pore size distribution was obtained by Barrett-Joyner-Halenda (BJH) method using adsorption branch of the nitrogen isotherm. The specific surface area of as prepared mesoporous graphene was calculated using Brunauer-Emmett-Teller method to be 157-220 $m^2\ g^{-1}$ at a relative pressure range of $P/P_0 = 0.05\text{-}0.25$.

XPS analysis was carried out on Kratos Axis Ultra XPS instrument with a hemispherical 165 mm electron energy analyzer. Microstructures of the samples were observed on TEM (JEM-1010, JEM-2010, JEOL) and SEM (Quanta FEG 450, FEI). The morphology of the graphene nanosheets was also observed on AFM (Ntegra Solaris AFM, NT-MDT). Elemental mapping was conducted using EDAX detector attached on JEM-2010.

Thermogravimetric Analysis (TGA) was conducted on TGA/DTA system (STAR^e, Mettler Toledo) at 25-900 ºC in a 15 ml min^{-1} Ar flow with a ramp rate of 5 °C min^{-1}.

4. Electrode preparation and electrochemical test

2 mg of the doped graphene samples were dispersed in a solution containing 1 ml of deionized water (18.2 MΩ) and 0.5 ml of 1 wt.% Nafion aqueous solution. The mixture was ultrasonicated to obtain a homogenous catalyst ink.

To prepare the working electrode for electrochemical measurements, 10 µl of the ink was dipped on a mirror polished glass carbon electrode and dried at 50 ºC in air; this was repeated 3 times. Then, the working electrode was inserted into the cell setup, which is composed of a platinum counter electrode, an Ag/AgCl/KCl (3 M) reference electrode and a 125 ml glass cell containing 80 ml of 0.1 M KOH aqueous electrolyte.

Cyclic voltammetry (CV) experiments were performed on an electrochemical analysis station (CHI 650 D, CH Instruments, USA). Before test, an O_2/N_2 flow was used through the electrolyte in the cell for 20 min to saturate it with O_2/N_2. The cell was kept in a 25 ºC water bath for all the electrochemical tests. CV was performed from 0.2 V to -0.8 V versus Ag/AgCl/KCl (3 M), with a sweep rate of 100 mV s^{-1}. The sample was tested 3 times to avoid any incidental error. Long term durability test of N-S-G and Pt/C (Vulcan, 20 wt. %) was also conducted using the same setup. The test was performed for 60 h with continuous O_2 flow bubbling in.

For the rotating disk electrode (RDE) test, the same amount of catalyst was loaded on a rotating glass carbon electrode (Princeton Applied Research). Electrochemical measurements were carried out on a CHI 760 C electrochemical biopotentiostat (CH Instruments, USA). A Pt wire and an Ag/AgCl/KCl (3 M) were used as the counter and reference electrodes, respectively. The linear sweep voltammograms of the modified glass carbon electrode were recorded in O_2 saturated 0.1 M KOH with a scan rate of 5 mV s^{-1} at various rotating speeds from 400 to 2000 rpm. After each scan, the electrolyte was saturated with O_2 again for 20 minutes. The sample was tested 2 times to avoid any incidental error.

The Koutecky-Levich plots were obtained by linear fitting of the reciprocal rotating speed versus reciprocal current density collected at different potentials form -0.4 V to -0.8 V. The overall electron transfer numbers per oxygen molecule involved in a typical ORR process weere calculated from the slopes of Koutecky-Levich plots using the following equation:

$$1/j_D = 1/j_k + 1/ B\omega^{1/2}$$

where j_k is the kinetic current in amperes at a constant potential, ω is the electrode rotating speed in rpm, and B, the reciprocal of the slope, which was determined from the slope of Koutecky-Levich plots based on Levich equation as followed:

$$B = 0.2\, nFA\nu^{-1/6}C_{O2}D_{O2}^{2/3}$$

where n is the number of electrons transferred per oxygen molecule, F is the Faraday constant （96485 C mol^{-1}）, D_{O2} is the diffusion coefficient of O_2 in 0.1 M KOH (1.9×10^{-5} cm s^{-1}), *v* is the kinetic viscosity, and C_{O2} is the concentration of O_2 (1.2×10^{-3} mol L^{-1}). The constant 0.2 is adopted when the rotating speed is in rpm.

II. Supplementary Results

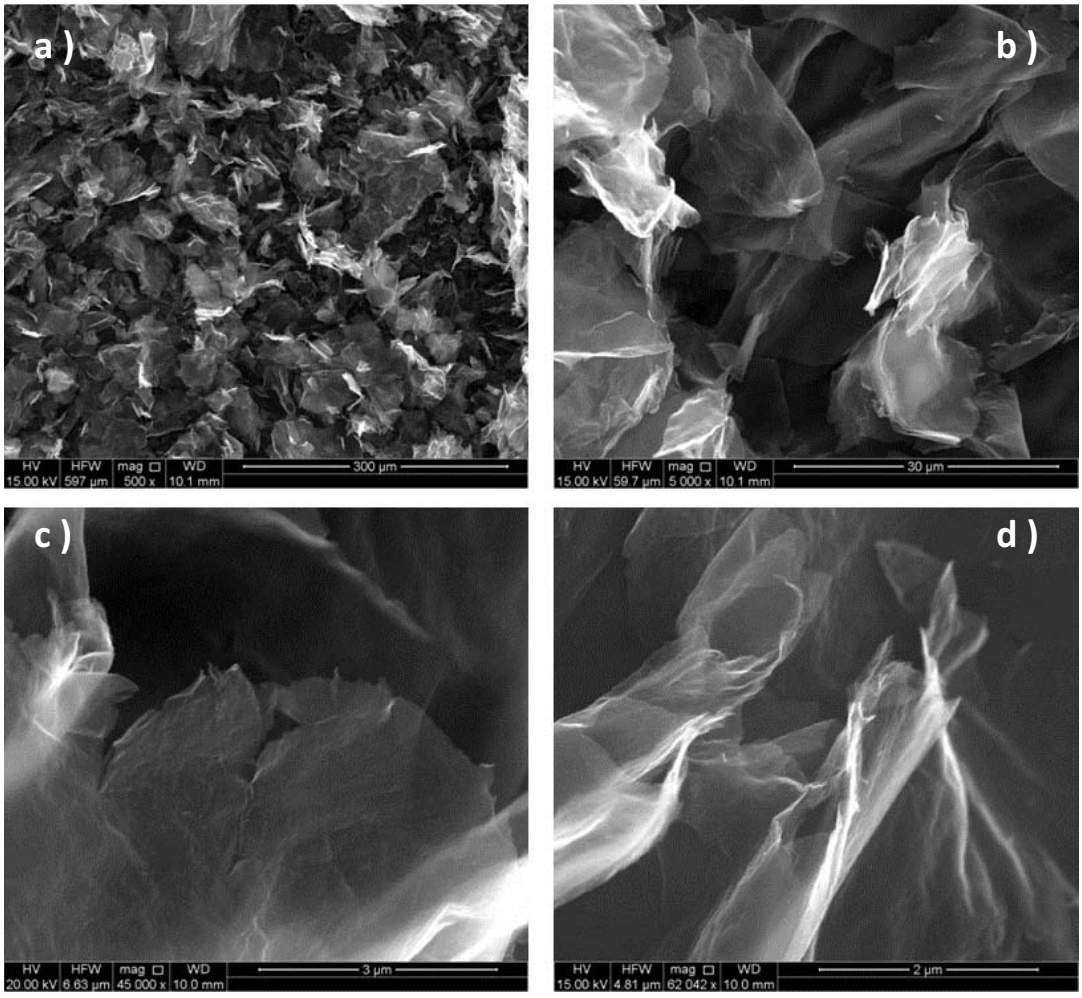

Figure S1. SEM images of mesoporous N-S-G at different magnifications. The sample shows a loose structure, rather than the close packed non-porous graphene layers present in a graphene paper formed without silica templates.

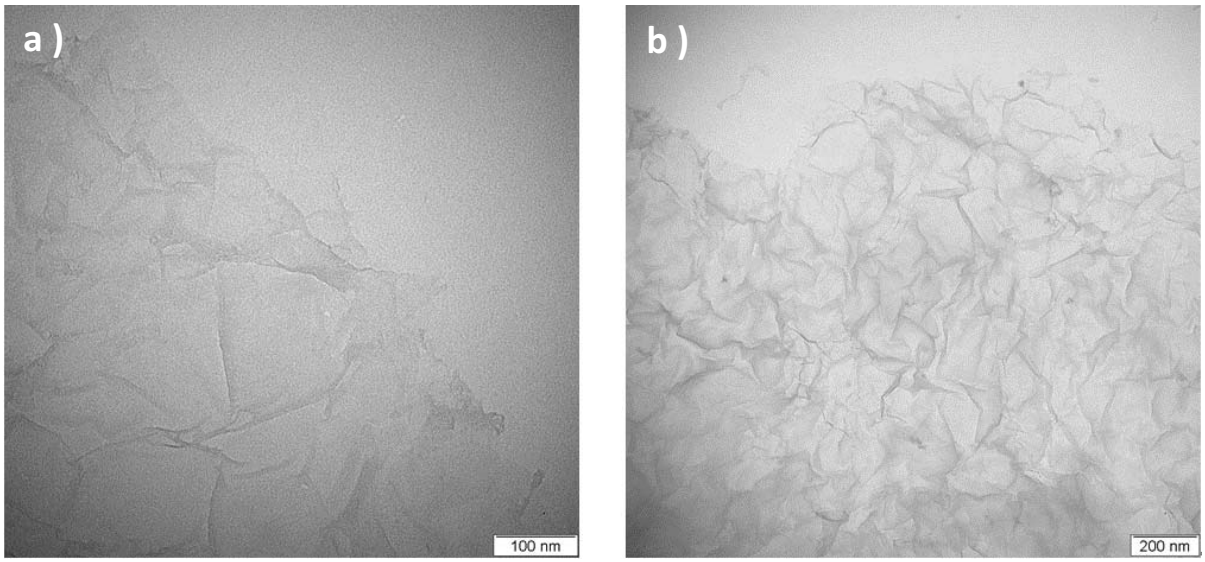

Figure S2. Additional TEM images of mesoporous N-S-G. All images show typical thin graphene nanolayers.

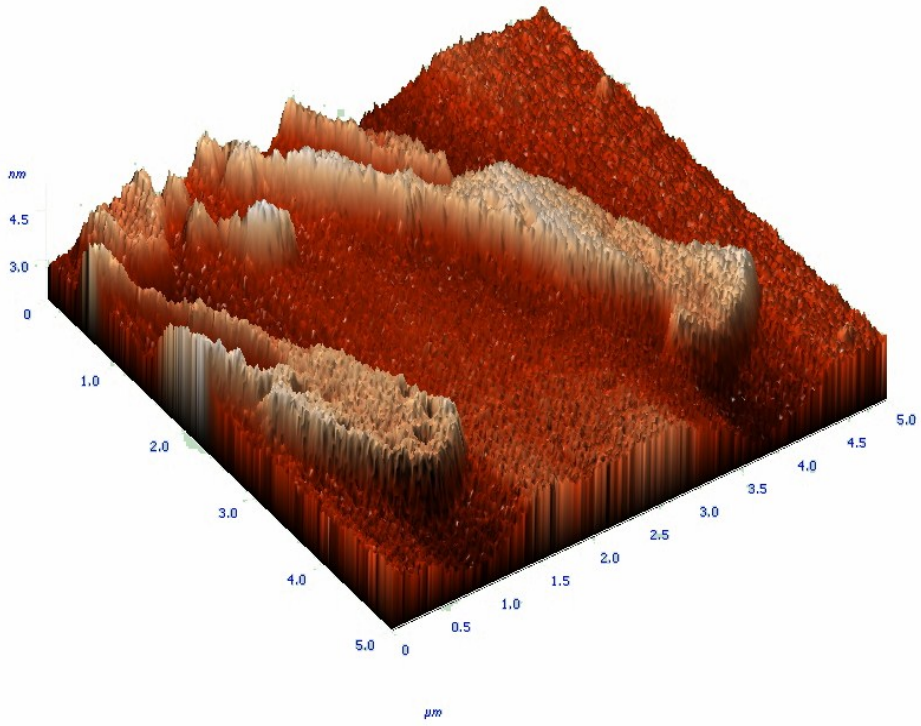

Figure S3. AFM image of N-S-G supported on a silicon wafer observed from a 3-dimensional view.

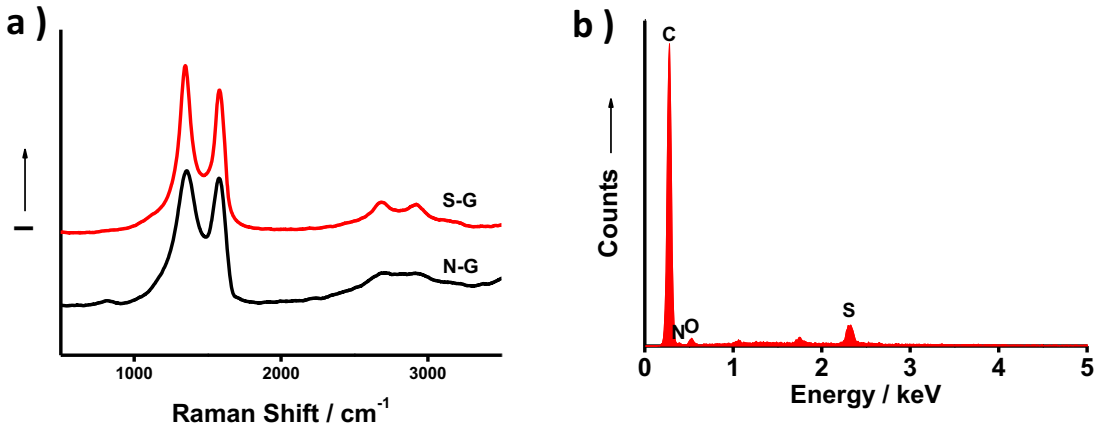

Figure S4. a) Raman spectra of N-G and S-G; b) X-Ray energy disperse spectrum of N-S-G showing the existence of S and N heteroelements on the graphene sheets.

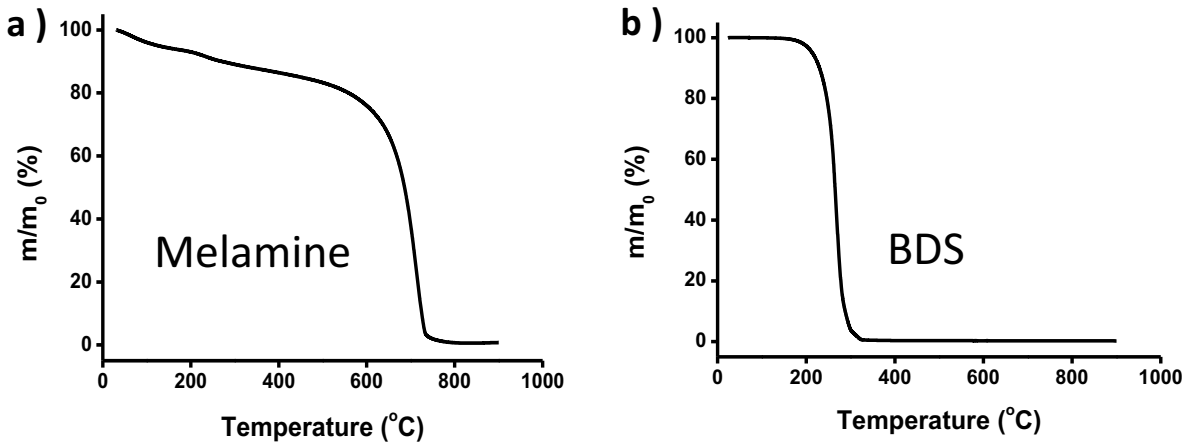

Figure S5. Thermal gravimetric analysis curves of a) melamine and b) BDS obtained by heating the samples from room temperature to 900 °C under the protection of Ar. The results show clearly a complete weight loss of both precursors below 800 °C, which excludes the possibility that the heteroelements on the N-S-G originate from any residuals of the precursors. This confirms the successful doping of the heteroelements into the graphene framework.

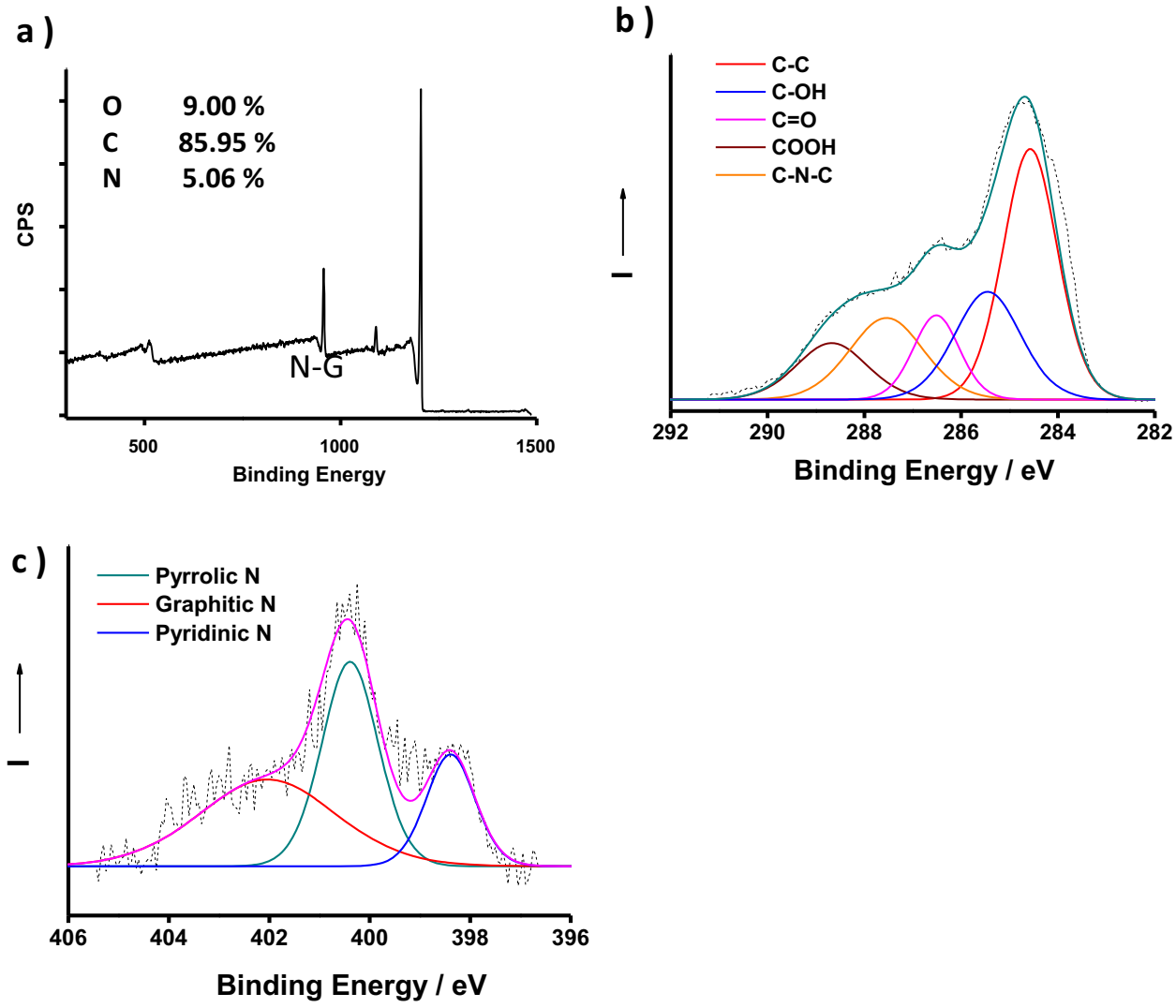

Figure S6. a) XPS sweep scan of nitrogen doped graphenee (N-G) as well as the high resolution spectrum of b) C1s and c) N1s species.

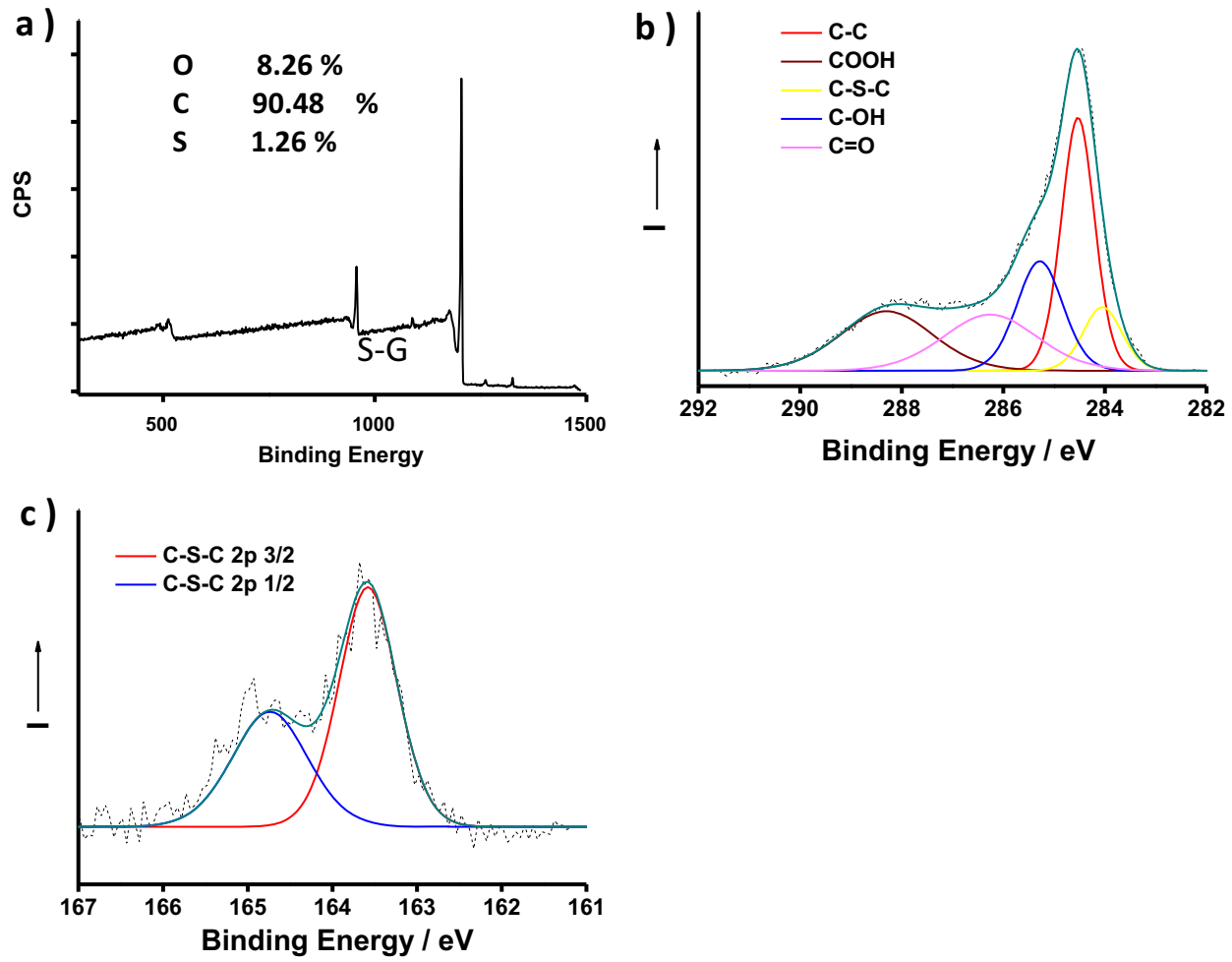

Figure S7. a) XPS sweep scan of sulfur doped graphene (S-G) as well as the high resolution spectrum of b) C1s and c) S2p species. Noticeably, both S-G and N-S-G show thiophene-type sulfur species only.

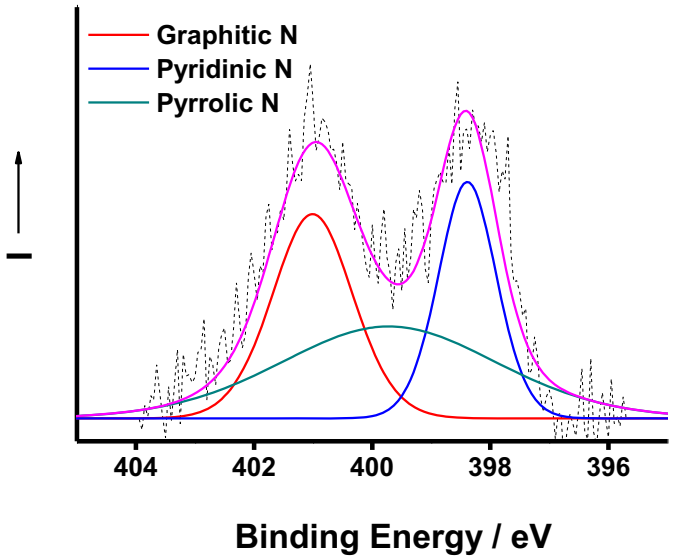

Figure S8. High resolution XPS spectrum of N1s in N-S-G, showing typical three types of nitrogen species in the doped graphene.

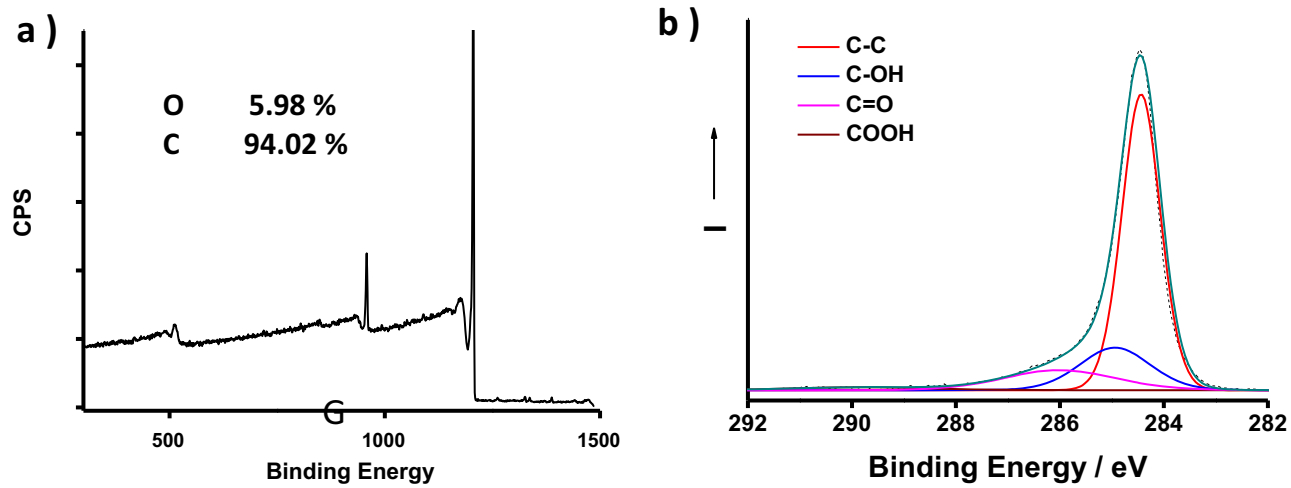

Figure S9. a) XPS sweep scan of graphene (G) as well as the high resolution spectrum of b) C1s species of G.

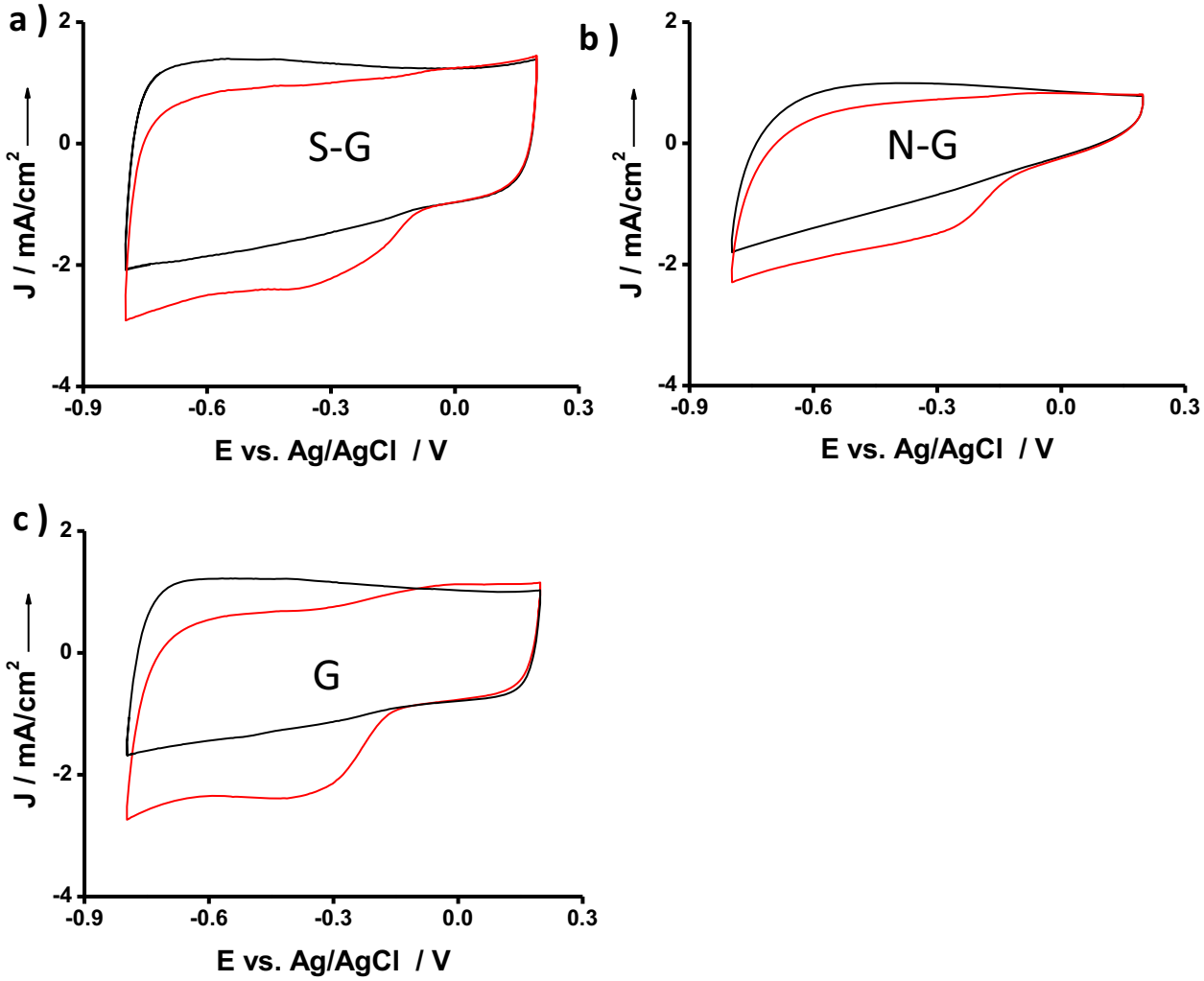

Figure S10. CV curves of a) S-G, b) N-G and c) pristine G from 0.2 V to -0.8 V vs Ag/AgCl in N_2 or O_2 saturated 0.1 M KOH aqueous electrolyte. Scan rate is 100 mV s^{-1}.

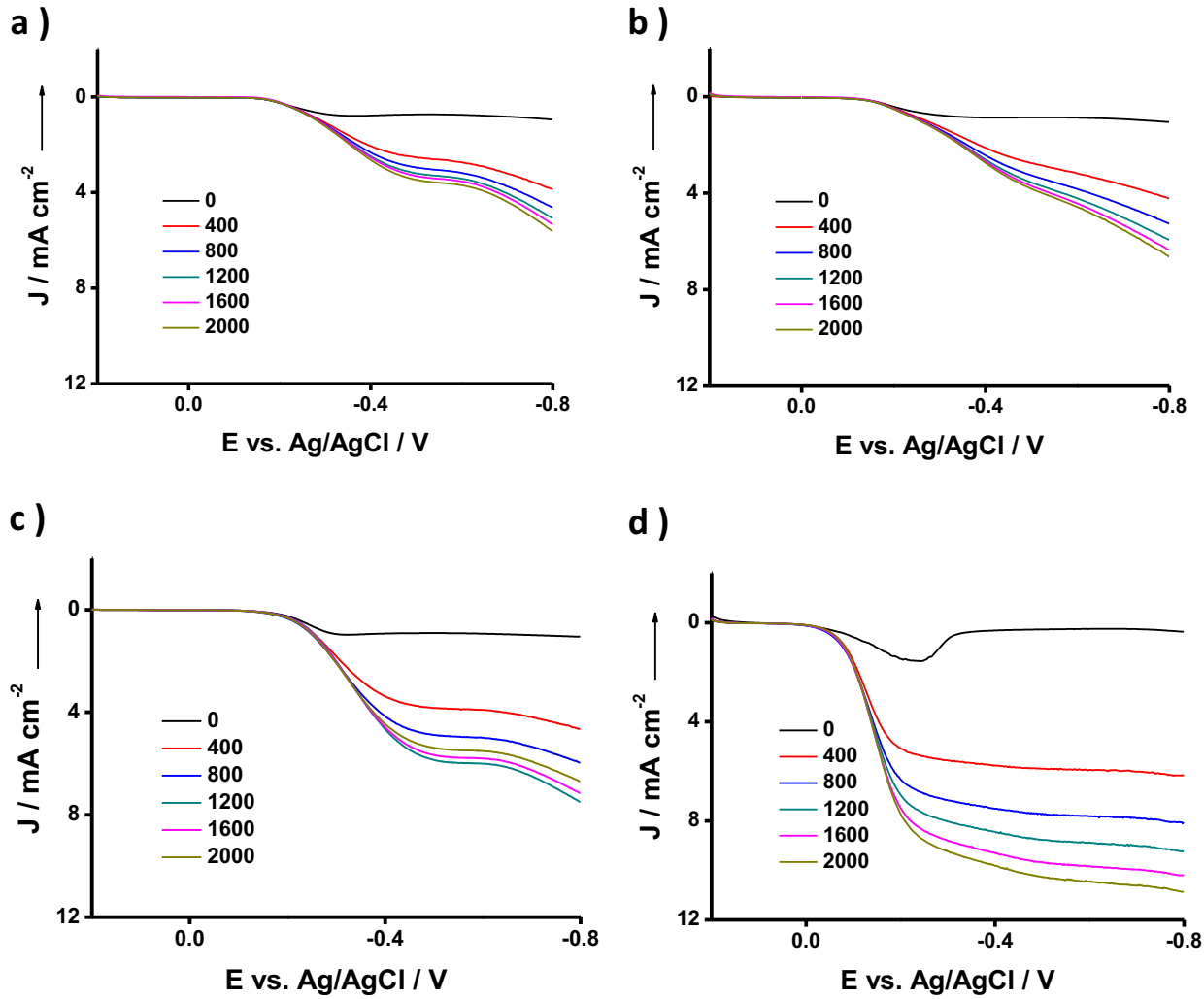

Figure S11. LSVs of a) pristine G, b) N-G, c) S-G and d) Vulcan Pt/C on a RDE at different rotating speeds from 0 rpm to 2000 rpm. All the tests were conducted from 0.2 V to -0.8 V with scan rate of 5 mV s^{-1} in an O_2 saturated 0.1 M KOH aqueous electrolyte.

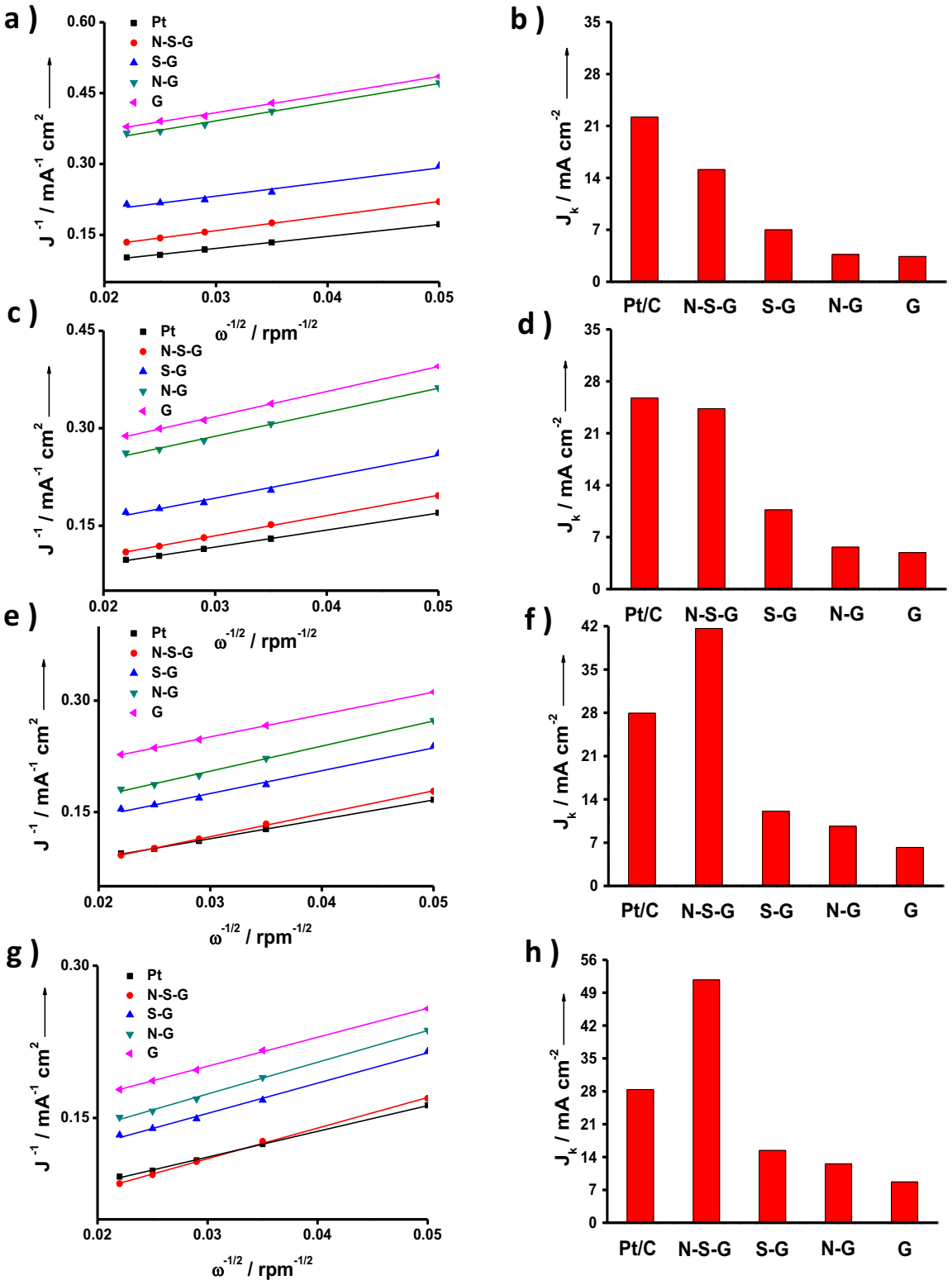

Figure S12. K-L plots and the corresponding kinetic limiting currents of N-S-G, N-G, S-G, G as well as Vulcan Pt/C obtained at different potentials: a, b) -0.4 V; c, d) -0.5 V; e, f) -0.7 V and g, h) -0.8 V.

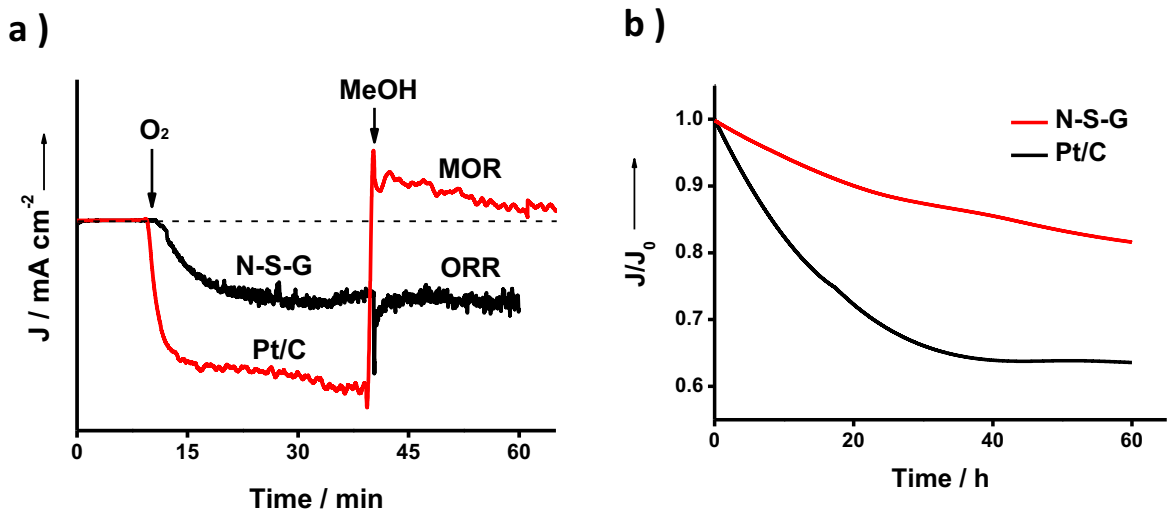

Figure S13. a) methanol crossover tolerance test of N-S-G and Vulcan Pt/C conducted by chronoamperometic response at -0.25 V vs Ag/AgCl in 0.1 M KOH aqueous electrolyte; the arrow indicates the introduction of O_2 and methanol. b) long-term durability test of N-S-G and Vulcan Pt/C by current-time chronoamperometric measurements at -0.25 V vs Ag/AgCl in O_2 saturated 0.1 M KOH solution.

III. Computational Calculation Section

1. Method

The explored model is based on a $C_{37}H_{15}$ model with all the edge carbon atoms saturated by hydrogen. Since S can only form double bond with C (XPS examination), the doping site for S is on the edge of such graphene cluster model. For S and N dual-doped model, nitrogen atom is then inserted into the S-G with varying distances to the sulfur (Figure S14). The obtained models are named as S-N-G-1 to S-N-G-5, correspondingly.

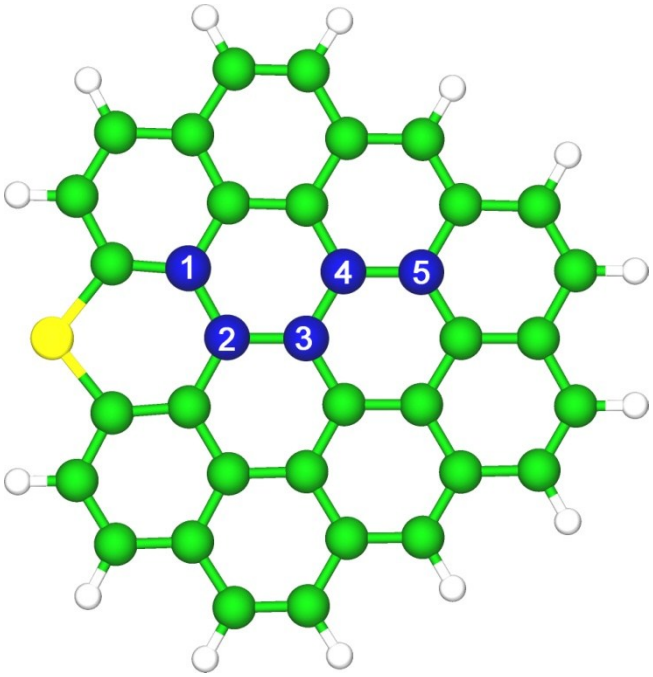

Figure S14. Models for S and N dual-doped graphene. Green is carbon, yellow is sulphur, blue atoms are reserved for nitrogen doping sites labeled from 1 to 5. The corresponding model names are S-N-G-1, S-N-G-2, S-N-G-3, S-N-G-4, and S-N-G-5.

The electronic structures were calculated using density functional theory (DFT) in the Gaussian 09 program.[2] All the calculations were carried out using UB3LYP/6-31G(d,p) level of theory with all atoms being fully relaxed. Charge and spin density on each atoms were calculated by Mulliken population analysis.[3] The bond orders and orbital analysis were calculated by Natural Bond Analysis.[4]

2. Spin and Charges

According to Zhang *et al.*,[5, 6] the atomic spin and charge densities determine the catalytic capability of the materials for ORR. Previous works show that the carbon atoms with positive spin or charge density larger than 0.15 are most likely to serve as catalytic active sites. Thus, the number of atoms with large positive spin or charge density could serve as a barometer to evaluate the activity of a specific molecular structure.

For the models assuming sulfur or nitrogen single doping, the largest charge identified by our calculations is 0.22 (the sulfur atom on S-G) and 0.27 (three carbon atoms next to nitrogen on N-G), respectively, as presented in Figure S15. However, these two models do not possess spin density at all, even when we deliberately break the orbital symmetry by the keyword guess=mix. The charge transfer on N-G could be explained by different electronegativities possessed by nitrogen and carbon. For S-G, in which the electronegativities of sulfur and carbon are similar, the charge transfer could originate from the mis-match of the two elements' orbitals. By Natural Bond Orbital (NBO) analysis, the most significant change in the sulfur's electron distribution is the loss of electron on 3s orbit due to its embedding into the carbon framework with sp^2 hybridization.

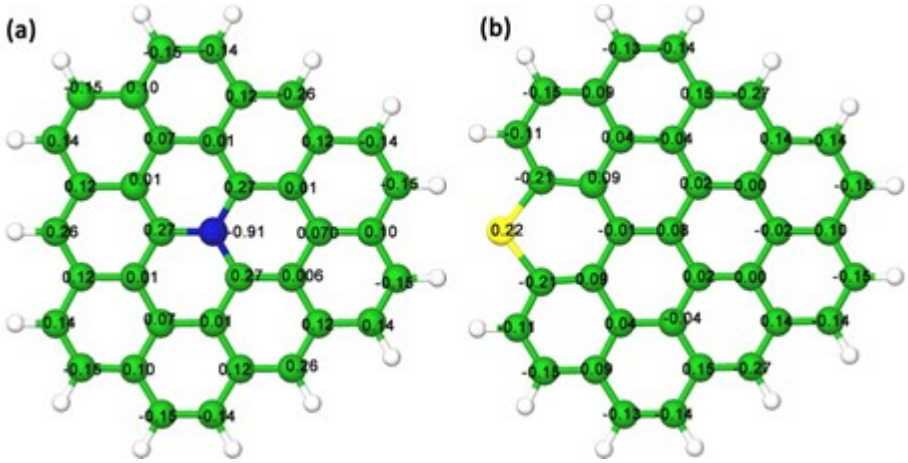

Figure S15. Charge distribution on a) N-G and b) S-G, respectively. Green is carbon, yellow is sulfur, and navy is nitrogen.

When the graphene cluster is dual-doped by sulfur and nitrogen, non-paired electrons are subsequently introduced and the atomic charge/spin density is greatly modified (Figures S16-19). The model with the largest number of active carbon atoms (N-S-G-3 in Figure 4) is presented in the main text.

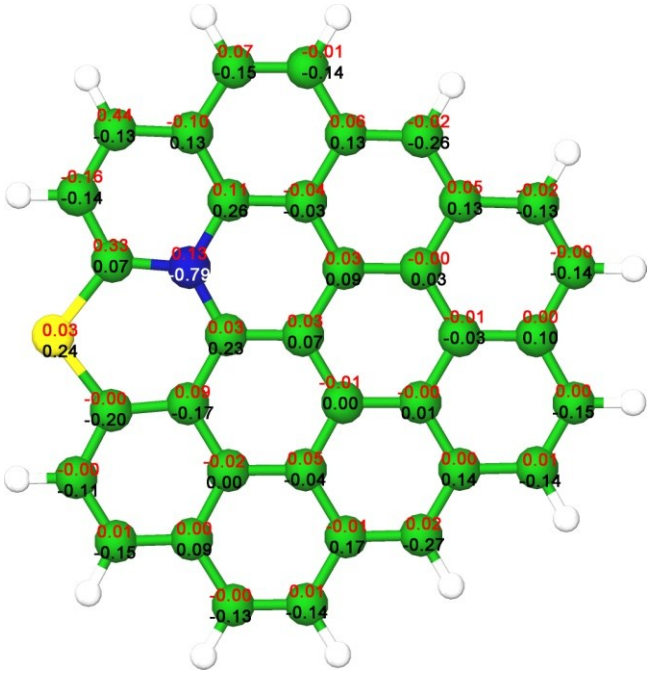

Figure S16. Charge and spin distribution on S-N-G-1. The numbers highlighted in red are the spin density values, and the numbers in black (white in the case of nitrogen) are the charge values populated to each atom. Green is carbon, yellow is sulfur, and navy is nitrogen.

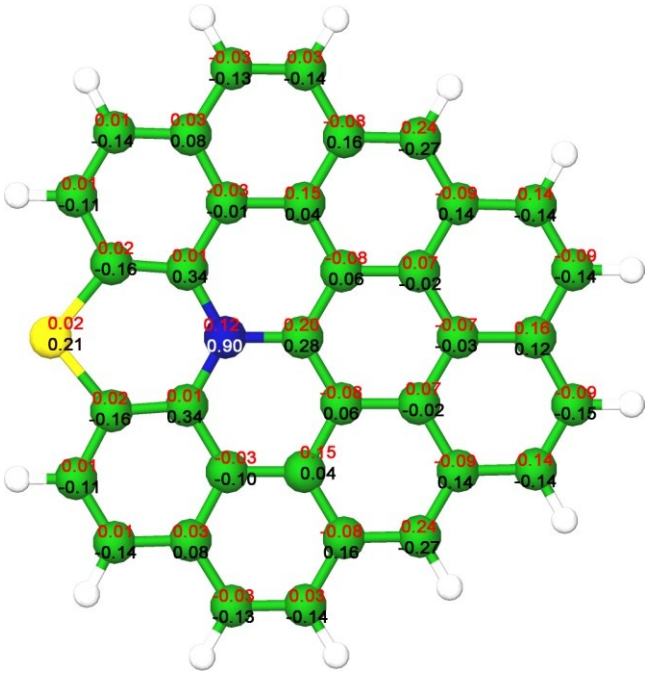

Figure S17. Charge and spin distribution on S-N-G-2. The numbers highlighted in red are the spin density values, and the numbers in black (white in the case of nitrogen) are the charge values populated to each atom. Green is carbon, yellow is sulfur, and navy is nitrogen.

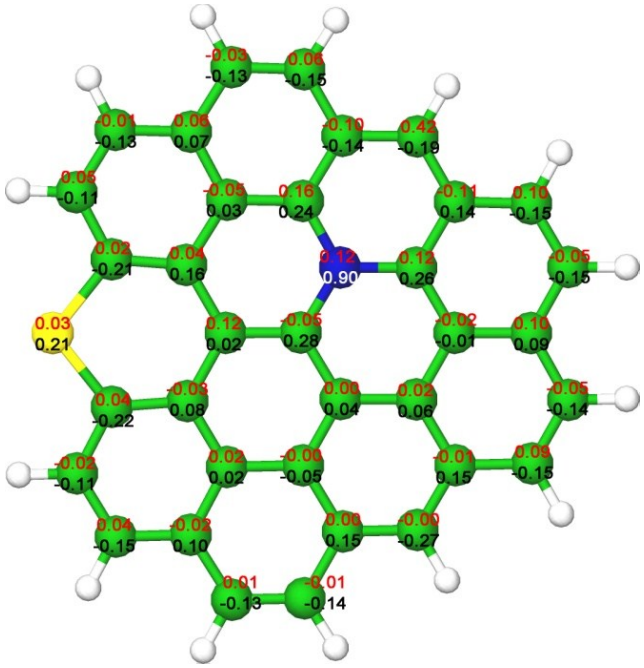

Figure S18. Charge and spin distribution on S-N-G-4. The numbers highlighted in red are the spin density values, and the numbers in black (white in the case of nitrogen) are the charge values populated to each atom. Green is carbon, yellow is sulfur, and navy is nitrogen.

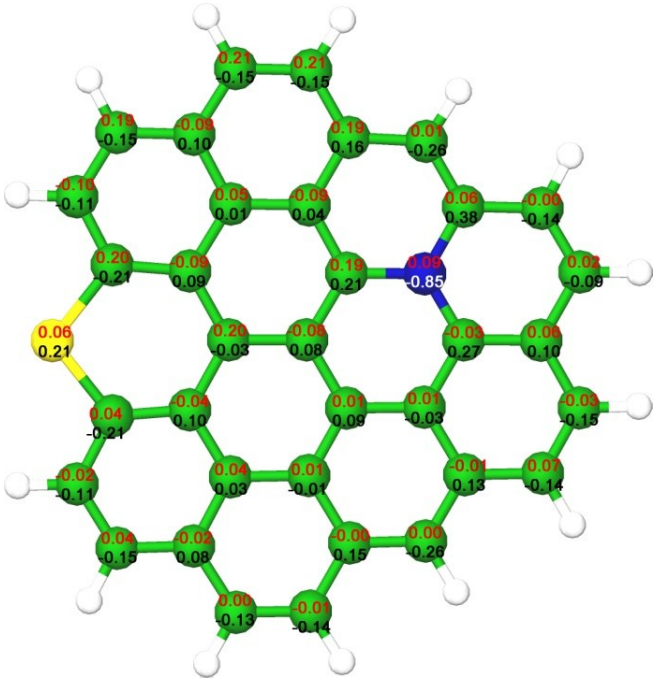

Figure S19. Charge and spin distribution on S-N-G-5. The numbers highlighted in red are the spin density values, and the numbers in black (white in the case of nitrogen) are the charge values populated to each atom. Green is carbon, yellow is sulfur, and navy is nitrogen.

In the above mentioned N-S-G model with different N and S relative positions, the elevation of charge and spin densities could be observed as compared with solely doped N-G or S-G or pristine

G, which is resulted from the interaction of two dopants; this finding is in a good agreement with the synergistically enhanced ORR performance.

References

[1] W. S. Hummers, R. E. Offeman, *Journal of the American Chemical Society* **1958**, *80*, 1339.

[2] M. J. Frisch, G. W. Trucks, H. B. Schlegel et al., *GAUSSIAN 09, Revision A.02* **2009**, Gaussian, Inc., Wallingford, CT.

[3] Mulliken, R. S. *J. Chem. Phys.* **1955**, *23*, 1833.

[4] E. D. Glendening, J. Badenhoop, A. E. Reed, J. E. Carpenter, J. A. Bohman, C. Morales, and F. Weinhold, *NBO version 3.1* **2001**, Theoretical Chemistry Institute, University of Wisconsin, Madison, Madison.

[5] L. Zhang, Z. Xia, *The Journal of Physical Chemistry C* **2011**, *115*, 11170.

[6] S. Wang, L. Zhang, Z. Xia, A. Roy, D. W. Chang, J.B. Baek, L. Dai, *Angewandte Chemie International Edition* **2012**, *51*, 4209.

Chapter 7 Conclusion and Perspective

7.1 Conclusions

The researches in this thesis are aimed at developing high performance but low-priced oxygen reduction electrocatalysts free of noble metals; as well as gaining insights into the kinetics and mechanism of the catalytic ORR process on these materials by design and construction of materials with controllable composition and structure. Based on these studies, the followed conclusions have been obtained:

(1) We have firstly designed and constructed a 3-dimensionally ordered macroporous g-C_3N_4/C catalyst with different pore sized as a metal-free catalyst for ORR. This novel catalyst possesses prominent ORR catalytic activity such as high reaction current density and moderate onset potential. As a metal-free catalyst, the macroporous g-C_3N_4/C showed much better fuel crossover resistance and long-term durability in alkaline medium. This material was synthesized through a simple procedure using inexpensive cyanamide as a precursor and easily fabricated silica microspheres as a template, which gives a great promise for large scale production. The pore size of g-C_3N_4/C can be easily tailored by using different size silica spheres as templates. By looking into the ORR catalytic behavior on the material with different pore sizes, we found that a large pore size (*ca.* 150 nm) is the most favorable for ORR in this material system, as it can provide a moderate surface area for active site exposure and good mass diffusion for reactant transference. These features make this macroporous g-C_3N_4/C material potentially promising for the expensive noble metal catalysts in the next generation alkaline and direct methanol fuel cells.

(2) Based on the above study, we found that it is hard to obtain both very large surface area and high mass transportation from pores with uniformed pore size distribution. So, we subsequently developed an elaborate bottom-up design of a nitrogen-doped carbon material with hierarchical porous; and interlinked the carbons with *in-situ* grown graphene to increase its electron conductivity. Remarkably, these excellent structural properties, such as large surface area, high accessibility and good conductivity, have made this metal-free material a very suitable candidate for electrochemical applications, which is approved by its inherent ORR catalytic actives with synergistically enhanced performance.

(3) To further enhance the materials' ORR catalytic activity, we then introduced Fe species into the system of hierarchical porous carbon interlinked by highly conductive carbon naomaterials. These Fe-N decorated hybrids have successfully combined the desired merits such as highly active Fe-N species, good conductivity, large pore size and sufficient surface area to catalyze the electrochemical reduction of oxygen. These excellent characters have endowed this material with outstanding catalytic performances closely comparable to or even better than Pt/C, considering their

very positive ORR onset potential, quite high ORR current, excellent durability and complete resistance to methanol crossover, which makes this catalyst promising as a potential substitute for Pt/C. Moreover, this material is made from very cheap chemicals via simple synthesis, which makes it convenient for large-scale fabrication. And most importantly, this research has shed light on a new avenue of enhancing materials' performance of electrochemical applications by simple structural optimization and in-situ architecting.

(4) Apart from designing materials' microstructure, we have also presented an N and S dual-doped mesoporous graphene as a metal-free catalyst for ORR. This material shows an excellent catalytic activity including positive onset potential and high limiting current. The DFT calculations have revealed that the synergistic performance enhancement results from the spin and charge densities redistribution brought by dual-doping of S and N atoms, which leads to a large number of carbon atom active sites. Moreover, this material is prepared through a very simple one-step doping process using solid and low-cost precursors, and its porosity has been introduced by employing commercially available colloidal silica; thus, it is easy adaptable for large scale synthesis.

In summary, we have developed a serial of materials with well-designed structures and components as catalysts for the electrochemical reduction of oxygen. These studies have not only provided a group of high-performance ORR catalysts; but also paved an avenue of the design, construction and optimization of novel carbon materials for the applications concerning the storage and conversion of clean energy.

7.2 Perspective

As catalysts for ORR as well as other electrochemical reactions, it is necessary to integrate several merits into the materials:

(1) Ideal hierarchical structure to maximize the actives exposure on/inside the catalyst and to facilitate the reactants access into the catalysts, which is especially important to ORR.

(2) Good conductivity also plays a crucial role controlling the kinetics of the electrochemical reactions. As a result, it is important to make these carbon based materials graphitized. However, robust porosity and high graphitization seem to be conflicting with each other. Thus, to design and build a hybrid material can be a solution to obtain high conductivity on the highly porous carbons.

(3) From the aspect of materials' composition, it has been found that Fe-N complex on the graphite frameworks in the carbon material can be highly active towards ORR. However, at the current stage, the content of these species is still too low in the carbon materials; so, it is still necessary for the studies on how to increase the amount of these active species as well as on the

discovery of new active species for ORR based on transitional metal complexes.

(4) Such materials, besides ORR, have also shown potentials to catalyze other reactions, such as the electochemcial/photochemical water splattering to produce hydrogen or oxygen and electrochemical reduction of carbon dioxide to produce fuels. Thus, these types of low-priced materials can be potentially promising as multi-functional substitutes of different noble metals in a variety of applications.

(5) Besides catalysis, these serial of materials can also be used in other applications concerning the storage of energy, such as a supercapacitor which requires large surface area and abundant porosity, a lithium-ion battery which requires sufficient mesopores or a lithium-sulfur battery which requires large pore volume and suitable hierarchical structures.

Appendix: Publications during Ph.D

Book Chapters

[1] **J. Liang**, S. Z. Qiao, G. Q. Lu, D. Hulicova-Jurcakova, Carbon-based Catalyst Support in Fuel Cell Applications, in: J.M.D. Tascon, *Novel Carbon Adsorbents,* Elsevier Ltd, **2012**, 549.

[2] **J. Liang**, R. F. Zhou, D. Hulicova-Jurcakova, S. Z. Qiao, Carbon Materials and Their Energy Conversion and Storage Applications, in: *Producing Fuels and Fine Chemicals from Biomass Using Nanomaterials*, Taylor & Francis Group, **2014**, 59.

Journal Papers

[3] **J. Liang**, X. Du, C. Gibson, X. W. Du, S. Z. Qiao. A Hybrid of Nitrogen-Doped Graphene and Hierarchical Porous Carbon for Enhanced Oxygen Reduction, *Adv. Mater.*, **2013**, *25*, 6226. **[Front Inside Cover]**.

[4] **J. Liang**, Y. Jiao, M. Jaroniec, S.Z. Qiao. Sulfur and Nitrogen Dual-doped Mesoporous Graphene Electrocatalyst for Oxygen Reduction with Synergistically Enhanced Performances, *Angew. Chem. Int. Ed.*, **2012**, *51*, 11496. **[Back Cover]**.

[5] **J. Liang**, Y. Zheng, J. Chen, J. Liu, D. Hulicova-Jurcakova, M. Jaroniec, S. Z. Qiao, Facile Oxygen Reduction on a Three-Dimensionally Ordered Macroporous Graphitic C_3N_4/Carbon Composite Electrocatalyst. *Angew. Chem. Int. Ed.,* **2012**. *51*, 3892.

[6] **J. Liang**, R. F. Zhou, X. M. Chen, Y. H. Tang, S. Z. Qiao, Fe-N decorated hybrid porous carbon catalyst for high performance oxygen reduction. *Adv. Mater.*, **2014**. *Accepted,* DOI: 10.1002/adma.201401848.

[7] **J. Liang**, R. F. Zhou, X. M. Chen, T. Y. Yang, S. Z. Qiao, Designable Fe-N-C Complex: an Avenue towards Best Oxygen Reduction Catalytic Activity. In Preparation.

[8] X. Du, B. Y. Shi. **J. Liang**, J. X. Bi, S. Dai, S. Z. Qiao, Developing Functionalized Dendrimer-like Silica Nanoparticles with Hierarchical Pores as Advanced Delivery Nanocarriers, *Adv. Mater.,* **2013**, *25*, 5981.

[9] Y. Zheng, Y. Jiao, J. Chen, J. Liu, **J. Liang**, A. J. Du, W. M. Zhang, Z. H. Zhang, S.C. Smith, M. Jaroniec, G. Q. Lu, S. Z. Qiao, Nanoporous Graphitic-C_3N_4@Carbon Metal-free Electrocatalysts for Highly Efficient Oxygen Reduction, *J. Am. Chem. Soc.*, **2011**, *133*, 20116.

[10] Y. Zheng, J. Liu, **J. Liang**, M. Jaroniec, S. Z. Qiao, Graphitic Carbon Nitride Materials: Controllable Synthesis and Applications in Fuel Cells and Photocatalysis*, Energy Environ. Sci.,* **2012**, *5*, 6717.

Conference Papers

[11] **J. Liang**, Y. Zheng, S. Z. Qiao, Porous Carbon and Graphene Based Materials for Enhanced Eclectrochemical Conversion, **2012**, American Chemical Society Annual Meeting, Vol 245.

[12] **J. Liang**, S. Z. Qiao, Carbon Based Completely Metal-free Catalysts for High Performance

Oxygen Reduction, International Conference on Nanoscience and Nanotechnology, **2014**, Abstract Collection.

[13] Y. Zheng, **J. Liang**, S.Z. Qiao, Metal-free electrochemical catalysts for oxygen reduction reaction, American Chemical Society Annual Meeting, **2012**, Vol 243.